2002135410

605693

Title: Fundamental Study of Material Flow in Friction Stir Welds 253P.

Type of Report: Summary of Research

Principal Investigator: Anthony P. Reynolds

Period Covered: 08/01/1998 through 07/31/1999

University of South Carolina
Office of Sponsored Programs and Research
901 Sumter Street, Fifth Floor
Columbia, SC 29308-0001

Grant #: NAG-1-2108

CC: R. Hafley/NASA Langley TO
CASI Document Processing
ONR Admin Grants Officer

GRANT
TR/IN/37
03 135 410

Abstract

The presented research project consists of two major parts. First, the material flow in solid-state, friction stir, butt-welds as been investigated using a marker insert technique. Changes in material flow due to welding parameter as well tool as geometry variations have been examined for different materials. The method provides a semi-quantitative, three-dimensional view of the material transport in the welded zone.

Second, a FSW process model has been developed. The fully coupled model is based on fluid mechanics; the solid-state material transport during welding is treated as a laminar, viscous flow of a non-Newtonian fluid past a rotating circular cylinder. The heat necessary for the material softening is generated by deformation of the material. As a first step, a two-dimensional model, which contains only the pin of the FSW tool, has been created to test the suitability of the modeling approach and to perform parametric studies of the boundary conditions. The material flow visualization experiments agree very well with the predicted flow field. Accordingly, material within the pin diameter is transported only in the rotation direction around the pin. Due to the simplifying assumptions inherent in the 2-D model, other experimental data such as forces on the pin, torque, and weld energy cannot be directly used for validation. However, the 2-D model predicts the same trends as shown in the experiments. The model also predicts a deviation from the "normal" material flow at certain combinations of welding parameters, suggesting a possible mechanism for the occurrence of some typical FSW defects.

The next step has been the development of a three-dimensional process model. The simplified FSW tool has been designed as a flat shoulder rotating on the top of the workpiece and a rotating, cylindrical pin, which extends throughout the total height of the flow domain. The thermal boundary conditions at the tool and at the contact area to the backing plate have been varied to fit experimental data such as temperature profiles, torque and tool forces. General aspects of the experimentally visualized material flow pattern are confirmed by the 3-D model.

Table of Contents

List of Figures

List of Tables

1 Introduction

1.1 Problem Definition

Metals can be joined by a variety of methods. In general, heat, force, or the combination thereof is necessary for the joining process. The most common processes are fusion welding techniques with intense localized heat inputs. Friction stir welding (FSW) is a solid-state joining technique especially well suited for high strength aluminum alloys. The heat necessary for the plastic flow of the material is generated due to viscous dissipation during the extreme plastic deformation. The advantages of the FSW process include good strength and ductility along with minimization of residual stress and distortion. These qualities of FSW are generally attributed to the solid-state nature of the process and a supposed low energy input to the weldment.

Although significant effort has been expended in putting FSW to use in full-scale production of such products as ferry boats, rocket fuel and oxidizer tanks, the operating mechanisms and in particular, only little was known about the process mechanisms when this research project started in 1998. The welding process was developed empirically with initially pure guesses of the welding parameters and tool dimensions. The knowledge of the proper welding parameters was based on trial and error experiments. However, systematic experimental and/or numerical studies of the parameters influencing the process are necessary for the optimization of the process.

The goal of the present work is to provide a comprehensive understanding of the material flow in FSW and to characterize the influences of the welding parameters. This study focuses on the development of a fluid mechanics based, numerical process simulation, which is supported and verified by experimental data.

The problem definition of this research project is as follows: Develop a process model to simulate the material flow and the heat transfer in FSW. Show the validity of the simplifications and assumptions of the model. Verify the model with experimental data.

1.2 Scope of the Research

The scope of this project consists of experimental and numerical investigations. Experimentally, the scope of this project includes the development of a marker insertion technique to describe semi-quantitatively the material deformation in friction stir welds performed at various welding parameters, with different tools, and different base materials; moreover, the acquisition of welding data, which is used for verification of the numerical analysis.

The scope of the numerical part of this project includes among others the determination of the "fluid" properties of the aluminum alloys at elevated temperatures; the development of a 2-D model based on the fluid mechanics; and the justification of the assumptions. The model is verified by comparison with the available welding data and the experimental flow analysis. Comprehensive parametric studies are conducted to investigate the influences of the welding parameters, different materials, and single material properties. Based on the results in 2-D, a three-dimensional model is developed also using the Eulerian flow formulation. Experimental data is used to determine the boundary conditions of the 3-D model and to verify the modeling results.

2 The Friction Stir Welding Process

Friction Stir Welding (FSW), developed at The Welding Institute in 1991, [1], [2], is especially well suited for joining high strength aluminum alloys. FSW is a solid state joining process combining deformation heating and mechanical work to obtain high quality, defect-free joints. The deformation heating is produced during the material transport of the two plates to be joined around a non-consumable, rotating tool. In general, the cylindrical FSW tool consists of a broad shoulder and a pin with a smaller diameter. Several different tool designs are seen in Figure 2-1.

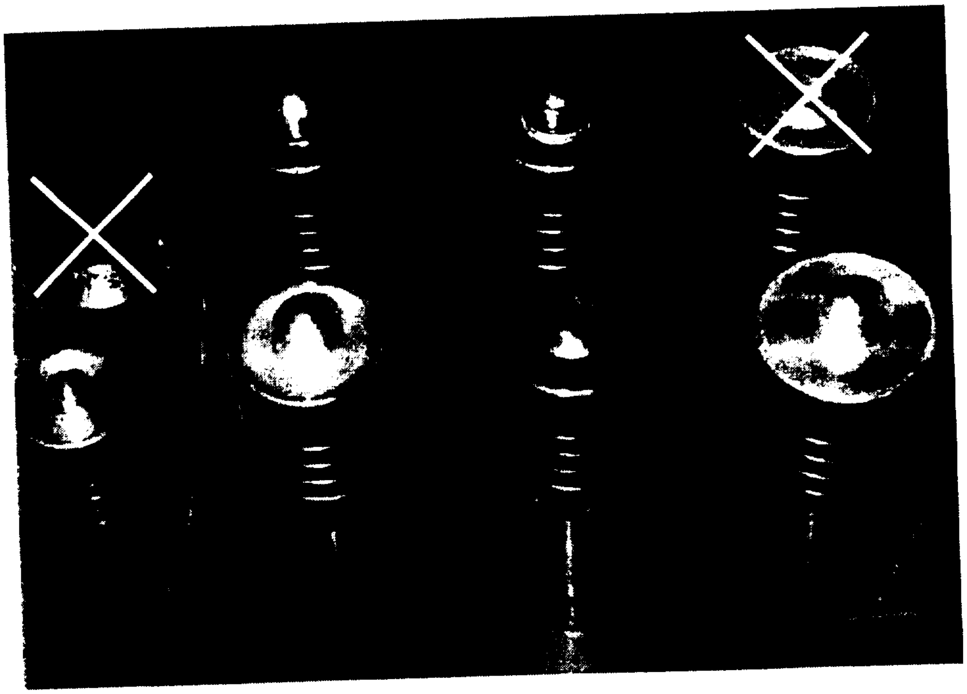

Figure 2-1 Friction stir welding tool designs.

The full penetration, single pass, welds were performed on either a vertical milling machine or the MTS FSW Process Development System. The steps required to make a friction stir weld are the following. First, the two pieces to be joined are clamped on a backing plate to hold the plates in place during welding. Second, the rotating tool, which consists of a broad shoulder and a narrower, threaded pin, is plunged into the faying surface of the two plates until the shoulder contacts the upper workpiece surface. The end of the plunging step corresponds to a certain pin clearance in displacement controlled welding and to constant vertical force in load controlled welding. The plunge depth or the vertical force is such that the tool shoulder provides enough forging pressure at the top surface of the plates. Third, the rotating tool traverses along the centerline, which describes the original interface of the two plates, forming a joint. Figure 2-2 is a schematic showing the welding set-up.

In the present research program most welds were performed with a 2.5° tool-to-workpiece-normal angle. Most recent tool developments allow the so-called zero-degree welding where the tool-to-workpiece-normal angle is zero. An advantage is the more practically oriented application of such tools since welding in other than the longitudinal direction is possible.

In general, the shape of the tool promotes high hydrostatic pressure along the joint line, causing consolidation of the material plasticized due to heat generation. Welding parameters are the rotational (or spindle) velocity, the welding (or translational) speed, as well as the vertical force on the tool or the plunge depth depending on the control mechanism. The welding parameters depend on the base material, the plate thickness, as well as the tool geometry and are to be determined for each new setup.

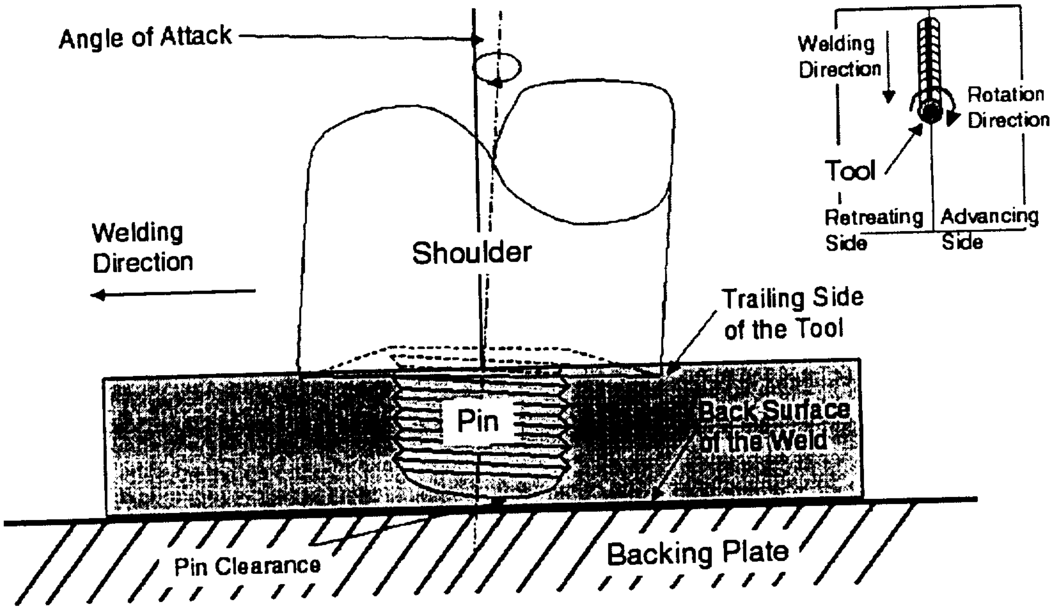

Figure 2-2 Schematic drawing of the FSW process.

Friction stir welding process is not symmetric about the centerline: the advancing side of the weld is defined as the side on which the rotational velocity vector of the welding tool has the same sense as the translational velocity vector of the tool relative to the workpiece. The retreating side is where the two vectors are of opposite sense. The leading side is the front of the tool and the trailing side indicates the back of the tool. The crown is the top surface of the weld and the root is the bottom surface.

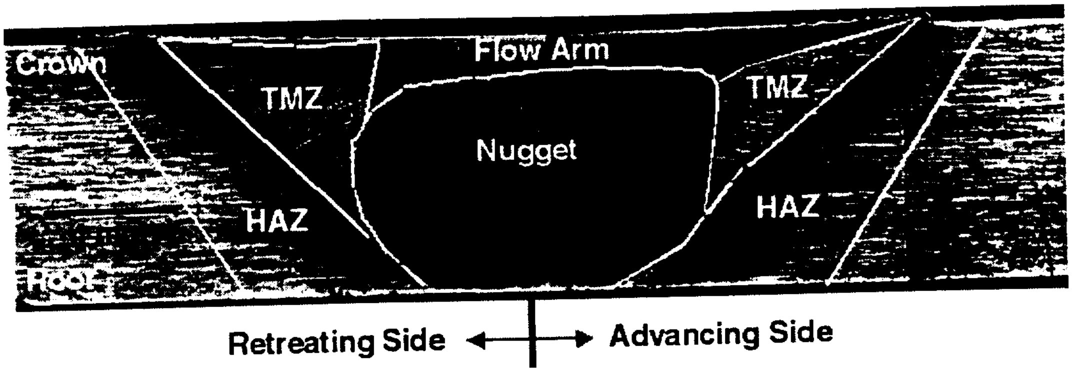

Figure 2-3 Typical microstructure of an AA2195-T8 friction stir weld

The microstructure of a typical friction stir weld has been described in numerous previous publications [3-6] but will be briefly reviewed here. Figure 2-3 shows the microstructure resulting from friction stir welding of AA2195-T8. The weld microstructure features can be separated into two broad categories: the thermo-mechanically affected zone, or TMZ, and the heat affected zone, or HAZ. The HAZ is similar to heat affected zones resulting from conventional, fusion welding processes. Depending on the alloy, its initial heat treatment, and the proximity to the weld centerline, processes occurring in the FSW HAZ might include precipitate coarsening, precipitate dissolution, recovery, recrystallization, and grain growth. The TMZ of a friction stir weld might be considered analogous to the fusion zone of a conventional weld except that, instead of being melted, the material in the TMZ has been mechanically worked.

Within the TMZ, there are three somewhat distinct regions. The most obvious is the "weld nugget". The weld nugget is the region, which has undergone the most severe plastic deformation and is characterized by a fine, relatively equiaxed, recrystallized grain structure. The width of the nugget is normally similar to, but slightly greater than, the diameter of the pin. Outside of the nugget on either side, is a region which has been deformed to a lesser extent and which, depending on the alloy, may or may not show signs of recrystallization. In Figure 2-3, the delineation between the nugget and the rest of the TMZ is quite sharp because of the recrystallization resistance of the AA2195-T8 base metal. The deformation of the base metal grains manifests itself as bending in the plane of the metallographic section (they are also bent in the horizontal plane perpendicular to the section). The third region of the TMZ is the "flow arm". This is the region of material above the nugget. The flow arm is formed when the rotating tool shoulder passes over the weld.

3 Literature Survey

3.1 Modeling Metal Forming Processes

Process models have been a great help in understanding plastic deformation in metal forming throughout the development of processes like extrusion, forging, and metal cutting. The simulation of metal forming processes is a challenging area for engineers because it involves non-linear material behavior, large deformation, coupled material flow and heat transfer as well as complex geometries and boundary conditions.

Zienkiewicz and Godbole [7] as well as Zienkiewicz et al. [8] were among the first who solved the flow of plastic and visco-plastic solids numerically by considering only the plastic deformation using a "flow approach". Neglecting the elastic deformation the large deformation metal forming process is equivalent to the flow of a viscous non-Newtonian fluid. In this case the constitutive law defines the strain rate as a function of stresses.

$$\bar{\dot{\varepsilon}} = f(\sigma_{ij})$$

Zienkiewicz et al. [9], and [10] presented a numerical solution algorithm for solving directly the coupled thermal plastic/visco-plastic flow such that the solution of the temperature distribution is obtained simultaneously with that for the velocity field;

even temperature and strain rate dependent constitutive equations were possible from now on. Since more than 90 % of the energy dissipated in the plastic deformation is converted into heat, the above mentioned papers were a significant step towards the real modeling of metal forming processes. Earlier solutions were dependent on the accuracy of pre-scribed temperature fields. Strenkowski and Moon [11] used the Eulerian flow formulation to model steady state flow in orthogonal metal cutting. They were able to predict the chip geometry, velocity, stress and strain rate fields as well as the temperature distribution in tool and workpiece.

In the application of finite element methods (FEM) to metal forming, there are two formulations, namely, the above-mentioned Eulerian flow formulation and the solid Lagrangian approach, which includes elasticity. The Lagrangian method takes a material mesh into account (instead of a spatially fixed mesh in the flow formulation) and allows natural surface shape changes. However, in large deformation processes the mesh distortion usually becomes unacceptably high so that remeshing and mesh refinement become necessary tools. Rebolo and Kobayashi ([12] and [13]) developed an algorithm for the coupled analysis of deformation and heat transfer of visco-plastic deformation in the Lagrangian FEM and applied their method successfully to solid cylinder compression tests. The coupled material flow and heat transfer analysis has been extensively used in the simulation of numerous metal forming processes like extrusion, forging, rolling, and metal cutting [14]. Kobayashi et al. [15] published a book, which covers a broad spectrum of finite element modeling in metal forming processes. Tang et al. [17] summarized the application of the commercial modeling software DEFORM^{TM} with examples on internal cracks, nut forming, shape rolling, and forging.

Throughout the years researchers developed metal forming processes such as extrusion, forging, and metal cutting by applying more and more sophisticated modeling techniques to the processes. Including more process relevant parameters in a simulation, allows the analysis of the metal forming processes in more detail. Reinikainen et al. [18] analyzed the 2-D, isothermal extrusion of copper with constant friction factors in the axisymmetric forward extrusion with two different die shapes and in the continuous extrusion process Conform^{TM}. They used a shear rate dependent flow stress at a constant temperature and found good agreement with experimental results of the material flow. Surdon and Chenot [19] presented a FE method to analyze the 3-D, isothermal hot forging process using a visco-plastic material and a nonlinear friction law based on the flow formulation. They simulated the isothermal compression of cubic blocks and proposed the expansion to more complicated geometries. Shiau and Kobayashi [20] studied the isothermal open-die forging and handled problems with the die-workpiece interface effectively using Bezier-curves at rounded tool edges. Their work focused on a computational scheme to solve general symmetric problems by reducing variables and rearranging them in the stiffness matrix.

Researches have constantly developed modeling techniques, while others applied the existing computer models to their research fields. Meidert et al. [21] compared two modeling techniques, a finite element and a physical model as design tools in cold forging. The physical model performed with plasticine was used to verify the material flow predictions of the FE model. The 2-D, FE model used a remeshing scheme for the isothermal deformation of the plasticity based strain hardening material. Shen et al. [22] analyzed the temperature history compensation in non-isothermal forging of Ti-6Al-4V. They proposed an isothermal modeling technique, which used a thermal correction of the flow stress and found better agreement with the experimentally determined forging load than with direct isothermal flow stress data. Cheng et al. [23] used a coupled deformation and thermal analysis to optimize process parameters in metal forging. It was possible for them to optimize the forging velocity with respect to strain rate and temperature gradients as well as the temperature range of the process.

Computer and software developments made it possible to include more processing relevant parameters than just the extruded component at a constant temperature. In the recent years, analysis in the field of the extrusion process includes not only the thermo-elastic-plastic behavior of the extrudate but also the thermal and elastic deformation of the extrusion die. Lu et al. [24] modeled thermo-mechanically the 2-D extrusion of temperature and rate dependent AA6061 in the continuous extrusion Conform^{TM} process including the elastic deformation of the extrusion die. The model enabled the authors to predict stress, strain, strain rate, and temperature distributions in both, the workpiece and the machine components. Udagawa et al. [25] simulated the flow and thermal fields in the extrusion of Ti-6Al-4V tubes including the development of an automated remeshing procedure. They observed that heat generation due to the large deformations is important to include in the model since localized temperature rises were over 100 °C. Influences of the ram speed on the temperature and stress distribution were investigated as well. Long and Balendra [26] studied the effect of the thermal and elastic behavior of both the component and the forming tool in cold-extruded aluminum and steel components. The accuracy of formed components is therefore significantly influenced by the thermal and elastic behavior of the process. The thermal expansion/contraction of aluminum had greater influence than the elastic behavior of the tool. Conversely, for steel, the elastic deformation of the die and the component were dominant factors influencing the component form errors. Chandra et al. [27] investigated the temperature rise in the initial stage of hot extruded AA6061 using a strain rate and temperature dependent rigid visco-plastic material law for the workpiece and temperature dependent elastic properties for the extrusion die. They discovered temperature rises of as much as 100 °C in the initial extrusion stage. The magnitude of the temperature rise was influenced by the area reduction ratio and the ram speed. The results, which were not verified in experiments, were proposed as useful guidelines in selecting process parameters to avoid extrusion defects and minimize temperature.

The finite element analysis of large deformation processes presents difficulties concerning the progressive distortion of the mesh. If the mesh distortion is severe, the computational errors are generally unacceptably high. These difficulties can be solved with proper remeshing techniques. In the past, finite element users were forced to perform remeshing manually, which is a very time consuming task. Petersen and

Martins [28] presented a paper on an automatic finite element remeshing system for quadrilateral elements with emphasis on local densification strategies. The algorithm computed the expected effective strains and effective strain rates allowing the new mesh generation to be based not only on the present but also on the expected plastic deformation. PavanaChand and KrishnaKumar [29] analyzed remeshing issues in the FEA of metal forming processes with focus on the data transfer during remeshing. Problems usually occur during the component-wise data transfer of tensor quantities such as stress and strain. The transfer of frictional contact boundary conditions may also lead to divergence if proper care is not taken while transferring data from the old to the new mesh.

A recent development in finite element modeling is the application of the Arbitrary Lagrangian-Eulerian (ALE) method. It combines the advantages of both the solid Lagrangian formulation and the Eulerian flow formulation. A major disadvantage of the updated Lagrangian method results from the fact that usually a considerably high amount of workpiece has to be processed before the desired steady state is achieved. However, the updated Lagrangian method is capable of predicting for example the transient chip formation in metal cutting and it obtains free surfaces in a direct way. However, the mesh is fixed to the material so that mesh distortion occurs; remeshing is required. In the Eulerian approach, the cutting action is modeled as the flow around the tool. No mesh refinement is required since the mesh is fixed spatially. The mesh density is only dictated by the gradients, thus, the Eulerian method is computationally more efficient and best suited for ductile materials by neglecting the elastic deformation of the material. The fixed mesh in space is on the other hand one of the disadvantages of the Eulerian flow approach since a priori assumptions about the shape of the flow domain are necessary. In the ALE analysis, the mesh is neither attached to the material nor fixed in space. The mesh has a motion that generally is independent of the material. In the Arbitrary Lagrangian-Eulerian formulation, models are Lagrangian until steady state conditions are reached and equivalent to the Eulerian one once these conditions are reached. Gouveia et al. [30] compared the updated Lagrangian and the combined Eulerian-Lagrangian formulations with respect to the cold forward rod extrusion. Both methods simulated the material flow and the extrusion forces with good agreement to experimental results. However, only the combined Lagrangian-Eulerian method predicted the friction accurately. Movahhedy et al. [31] demonstrated that ALE is an efficient approach in modeling orthogonal metal cutting because it combines the strength of the Eulerian and the Lagrangian analysis. The advantageous feature of the ALE in metal cutting is that no change in the mesh topology is needed and frequent remeshing including the data point interpolation is avoided, as the mesh motion becomes part of the solution procedure. Movahhedy et al. predicted the chip formation, its thickness and shape. However, no experimental data was used to verify the simulation results. Joyot et al. [32] simulated the orthogonal metal cutting process in two dimensions, including frictional heating, using an ALE method and found good agreement with experimental measurements of cutting forces and chip thickness.

Simplifying assumptions of the frictional contact are shortcomings of many simulations of metal forming processes. The simplest form is using a constant friction factor. Nakamura et al. [33] showed how the forward rod – backward can extrusion can be used as a friction test and carried out several tests with AA6061 and varying lubricants. Peric and Owen [34] published a comprehensive work on FE in nonlinear mechanics. They covered finite-strain elasto-plastic deformations material incompressibility, adaptive mesh refinement as well as modeling frictional contact conditions. The friction coefficient was developed as a function of the density of frictional work, which acts as an internal variable. The resultant constitutive model for frictional contact is analogous to classical work hardening plasticity. Oancea and Laursen [35] proposed a thermodynamically consistent frictional model, which included the coupling of mechanical response to the thermal field through frictional heating as well as the rate dependence. The frictional model was successfully applied to a number of examples including frictional contact between two bodies. Antunez and Kleiber [36] presented a steady state, 2-D Eulerian approach of metal cutting including a sensitivity analysis to the friction coefficient in a Coulomb friction law.

3.2 Modeling Friction Welding

The role of friction in material joining techniques first became important with the development of Friction Welding in the early 1960's. Dickson and Bahrani [37] gave an outline of the main types of the friction welding process describing the effect of the main process variables like the velocity of rubbing, the axial pressure, the welding time as well as the thermal and frictional material properties. Friction welding is a solid-state joining process that produces coalescence by the heat developed between two surfaces by a mechanically induced rubbing motion, mostly of rotational nature. The two surfaces are held together under pressure and due to the developed heating, a plasticized layer forms at the interface. After a predetermined time the rotation stops and the pressure is increased to facilitate forging of the heated metal. Process models have been a great support in understanding process details bringing friction welding to full-scale production in industry. Midling and Grong [38] were among the first who developed a process model including a heat flow model, the strain rate distribution a kinetic model and constitutive equations. Even though the heat flow model was just one dimensional they were able to predict adequately the peak-temperature and time-temperature profile over a wide range of operational conditions of welding AA6082-T6 and an Al-SiC metal matrix composites (MMC). Midling and Grong predicted strain rates that might exceed 1000 s-1 in positions close to the contact region. The strain rates were calculated based on an analytically assumed 2-D velocity distribution. Vairis and Frost [39] reported on the extrusion stage in the recently developed linear friction welding of Ti-6Al-4V, where two parts move relative to each other under pressure in a direct reciprocating mode produced by a linear mechanism. They obtained the heat flow and the strain distribution in a similar analytical model as Midling and Grong. Due to the oscillating nature of the linear friction welding process the reported strain rates were about two orders of magnitude lower than in conventional continuous drive or inertia friction welding. Fu and Duan [40] reported on a FEM model, which combined deformation and heat flow for a friction welded joint of a nickel-base superalloy. The calculated temperature stress and strain fields were in good agreement with experimental results. Francis and Craine [41] published their model on continuous drive friction welding of thin steel tubes. They approached the process using a flow formulation but used only a constant Newtonian viscosity, which does not account for the temperature and strain rates dependence of the material. Healy et al. [42] proposed an analytical dynamic analysis of the equilibrium phase in friction welding using a Bingham plastic model for the apparent viscosity and calculated the equilibrium torque in good agreement with experimental data. Bendzsak et al. [43] developed a two dimensional, steady state Eulerian flow model of friction welding. The non-Newtonian, laminar material flow was simplified by assuming isothermal conditions, hence, the viscosity was a function of the strain rate, only. This model was the first to give insight in the material flow pattern in friction welding. Zhai et al. [44] and North et al. [45] compared the numerically obtained material flow of friction welded AA6061/Al2O3 MMC with experimentally observed flow patterns and found an excellent agreement. Despite its simplifying assumptions, Bendzsak's Eulerian flow model has been successfully applied to the steady state stage in the friction welding process.

3.3 Experimental Material Flow Analysis in Friction Stir Welding

There have been some studies incorporating flow visualization in Friction Stir Welding. Midling [46] investigated the influence of the welding speed on the material flow in welds of dissimilar aluminum alloys. He was the first to report on interface shapes using images of the microstructure. The flow visualization, however, was limited because no other detail except for the interface of the different alloys was investigated. Li et al. [47] described patterns observed on metallographic cross-sections in friction stir welds made between dissimilar aluminum alloys and between aluminum alloys and copper. The material flow was described as a chaotic-dynamic mixing. Colligan [48] studied the material flow using embedded steel spheres placed along the weld centerline before welding. Colligan reported that material is stirred only in the upper portion of the weld and that in the rest of the weld, material is simply extruded around the pin. Colligan's approach to flow visualization, although elegant, was limited by following single points in the weld. However, it must be stated that details of the material flow are dependent on the exact tool geometry and the welding parameters used; therefore, the generality of any conclusions about the material flow has not been established.

Seidel and Reynolds [49], Reynolds et al. [50], Reynolds et al. [51], Reynolds [52], and Seidel and Reynolds [53] have analyzed the material flow of AA2195-T8 in several friction stir welds using a marker insert technique. This method is based on a post weld determination of the position of AA5454-H32 markers placed in the faying surface of the weld. The marker insert technique allows determination of the positions of material pre- and post-welding in the thermo-mechanically affected zone (TMZ) by a serial sectioning technique. As a result, full three-dimensional plots of the deformed markers are obtained. They provide a good qualitative characterization of the material flow in friction stir welds. An extended analysis of the material flow in friction stir welds performed in different materials with varying welding parameters and tool geometries is presented in 5.

Larsson et al. [54] investigated the material flow and mechanical properties of dissimilar friction stir welds containing AA6082 and AA5083. Although dissimilar alloys were welded, the flow pattern shows the same features as they were discovered in the USC friction stir welds using the marker insert technique ([49]-[53]).

London et al. [55] presented a very nice work on flow visualization in friction stir welded AA7050 at the Aeromat Conference in 2001. They used SiC powder as a flow tracer and determined the positions of the tracer by post-weld metallographic sectioning. By stopping the FSW tool abruptly while the tool did not pass the tracers completely, London et al. were able to follow the material's flow path on its way around the tool. The resulting final positions of the tracers were almost identical with the marker positions of the marker insert technique at USC.

3.4 Analytical and Numerical FSW Models

Since the invention of Friction Stir Welding (FSW) in 1991, analytical as well as numerical models were developed accompanied by extensive experimental work in order to gain more information about the mechanisms of the process. The first models were of analytical nature and dealt with the heat flow in FSW. Russell and Shercliff [56] presented a quasi-steady state analytical heat flow model, which combined a frictional shoulder heat generation and a distributed circular source solution. However, the authors ignored the effect of the tool pin, and bulk material heat generation. Frigaard et al. [57] developed a 2-D numerical heat flow model based on the finite difference approach including transient heating and cooling in FSW. As the aforementioned authors, Frigaard et al. neglected the heat generation due to the rotating pin as well. Frigaard and his co-authors expanded their model to a 3-D heat flow analysis based on the method of finite differences [58]. With the obtained temperature profile, which predicted the peak temperatures approximately 30 °C above the measured ones, they were able to make good predictions of the hardness in the weld nugget. Gould and Feng [59] published their work on a relatively simple heat flow model that used a point heat source and considered only frictional heating at the shoulder. The first thermal and thermo-mechanical FEM work on FSW was done by Chao and Qi [60]. The model was three-dimensional and included the backing plate as well as a reduced yield stress in the weld nugget. The heat generation in their model was due to frictional contact between tool shoulder and workpiece only. However, the total heat input was obtained by fitting the analytical model to experimental thermocouple data. Based on the 3-D temperature distribution post-weld residual stresses were calculated. Tang et al. [61] published detailed experimental temperature data of friction stir welded AA6061-T6. They measured almost constant peak temperatures between pin and shoulder in transverse direction with decreasing temperatures from the crown to the root of the weld. Tang at al. concluded from their data that the friction at the tool shoulder dominates the heat generation in FSW.

Steward et al. [62] were the first to present analytical models of the FSW process. With the development of the "Mixed Zone" model and the "Single Slip Surface", they were able to predict the shape of the weld plug, the energy input, the forces, and the maximum temperatures. Although the single slip model, which includes a restricted zone of deforming material, was the most successful model so far, it ignored the three dimensional effects in FSW. Nunes [63] created a plug model upon the work of Steward et al., in which material is transported around the pin as it translates through the workpiece by a "last in first out" wiping action. Accordingly, material movement occurs only around the retreating side of the pin. His "merry-go-around model" accompanied by copper wire experiments showed a secondary circulation driven by the threads of the pin, creating a vortex ring, which is mainly responsible for moving material in and out of the primary plug. The most recent developments in FSW process models focus on the numerical simulation of the material flow.

Smith et al. [64] determined the non-Newtonian properties of the plasticized region using an iterative process. They converted torque data measured during the plunging of the tool into viscosity and used it as an input for a 2-D flow model, in which viscous dissipation was used as the only heat source. A converged solution of the viscosity was found when measured and calculated temperature profiles matched. Smith et al. applied the obtained viscosity in a three dimensional model based on the flow formulation. However, only preliminary simulation results were published. North et al. ([65] and [66]) continued the work of Smith et al. and developed a 3-D FSW model based on the flow formulation. Computational limitations prevented them from performing a coupled analysis. Instead, they assumed constant temperatures in different regions in the flow domain. Consequently, North et al. used a constant viscosity equal to that at the eutectic temperature.

Colegrove et al. [67] showed a 3-D model including a threaded pin, where heat was generated at the shoulder only. The model consisted of a global thermal and a local thermo-mechanical model near the tool. It is believed that due to the coarse mesh that Colegrove at al. used, important information in the vicinity of the tool is lost.

FSW process models are valuable tools to determine the influence of the diverse FSW related parameters on the flow field and on the material consolidation behind the tool. As shown, efforts have been undertaken to create full three-dimensional process models. At USC two different types of FSW process models are pursued: A solid mechanics based model is developed by Xu, S. [68] and currently expanded to 3-D. The other approach is a fluid mechanics based model. A two-dimensional model has been developed to determine the correctness of the "flow formulation" approach. As the flow visualization has shown, the flow pattern changes throughout the thickness with increasing rotational to translational speed ratio. Hence, a 3-D process model, which includes also the tool shoulder, may simulate and rebuild the complicated flow pattern observed in many welds. In the present research the commercial available computational fluid dynamics (CFD) code FLUENT was used to develop a FSW process model. As a first step, the 2-D model simulates the steady state, laminar material flow past a rotating circular cylinder with a coupled heat generation due to viscous dissipation. The aluminum alloy is considered as a non-Newtonian, shear thinning fluid. The viscosity is based on the flow stress of aluminum using the Zener-Hollomon parameter. The model was used to perform parametric studies with respect to the welding parameters and material properties. Several 3-D geometries were created and tested for different welding parameters. In the simplest form, the tool consists only of a non-threaded, non-tilted pin. Most research was conducted with a non-tilted tool, which consists of a flat shoulder with a non-threaded pin. The physics of the model, the results of the 2-D model and of the 3-D model are presented in the chapters 6, 7, and 8, respectively.

4 Experimental Procedures

4.1 Friction Stir Welding

The friction stir welds presented in this research served two purposes. Different aluminum alloys were welded at varying welding parameters to visualize the material flow with maker inserts. Welds were also performed at different welding parameters to acquire weld specific data such as tool forces, torque, and power. The procedure to produce the welds has already been discussed briefly in Chapter 2.

All friction stir welds before the year 2000 were performed on a displacement controlled 15 Hp Supermill vertical milling machine at the University of South Carolina. For example, all the aluminum plates prepared for the flow visualization using the marker insert technique (Section 4.2) were welded on the milling machine.

In 2000, USC purchased the first custom built Friction Stir Welding Process Development System (FSW-PDS) from MTS Systems Corporation. During the fully automated welding process data such as spindle speed (RPM), welding speed (WS), tool forces, torque is acquired. Load and displacement controlled welding are possible with the PDS. In general, load controlled welding is preferred because it usually guarantees better (more uniform) weld quality. The vertical force on the FSW tool is used as a control parameter instead of a constant vertical tool displacement, i.e. the plunge depth. In displacement controlled welding, the tool is hold at the same vertical position regardless of shape changes of the plates to be welded.

In load controlled welding, a constant vertical force (z-force) is maintained during welding. Assuming that the z-force provides enough forging pressure for full weld consolidation at all times, small changes in the plate thickness for example do not cause a different weld quality. The tool is following the shape of the plate surface. Load controlled welding is more useful for industrial applications where different 3-D shaped panels may be welded. Hence, load controlled welding does not only provide a more consistent weld quality, it is also more application oriented than displacement controlled welding. The different weld setups on the two machines are described in sections 4.1.1 and 4.1.2.

The single-pass friction stir welds investigated in this research were butt-welded plates of 8.1 mm thick aluminum alloys except for partially penetrated welds in 25.4 mm thick AA6061 as described in Section 4.1.2. The aluminum alloys **2024**-T351, **2195**-T8, **2219**-T87, **5083**-O, **6061**-T6, **7050**-T76, and **7075**-T7351 were welded using different welding parameters and tools, respectively. Table 4-1 and Table 4-2 list the nominal compositions of the different aluminum alloys.

Common features for all tools used for the 8.1 mm thick plates include: pins threaded with a standard machine screw type thread and a thread pitch of 0.8 threads/mm, a shoulder dish angle of 7° (concavity), a pin length of 7.9 mm, and a pin tip radius of 8 mm. The standard tool, which was used in most of the welds, had a 9.9 mm pin diameter and a 25.4 mm shoulder diameter.

2024-T351		2195-T8		2219-T87		5083-O	
Comp.	Wt. %	Comp.	Wt. %	Comp.	Wt. %	Comp.	Wt. %
Al	93.5	Al	93.98	Al	93	Al	94.8
Cr	Max 0.1	Cu	4.0	Cu	5.8 - 6.8	Cr	0.05 - 0.25
Cu	3.8 - 4.9	Li	1.0	Fe	Max 0.3	Cu	Max 0.1
Fe	Max 0.5	Mg	0.5	Mg	Max 0.02	Fe	Max 0.4
Mg	1.2 - 1.8	Ag	0.4	Mn	0.2 - 0.4	Mg	4 - 4.9
Mn	0.3 - 0.9	Zr	0.12	Si	Max 0.2	Mn	0.4 - 1
Si	Max 0.5			Ti	0.02 - 0.1	Si	Max 0.4
Ti	Max 0.15			V	0.05 - 0.15	Ti	Max 0.15
Zn	Max 0.25			Zn	Max 0.1	Zn	Max 0.25
				Zr	0.1 - 0.25		

Table 4-1 Nominal compositions of the aluminum alloys 2024, 2195, 2219, and 5083.

5454-H32		6061-T6		7050-T76		7075-T351	
Comp.	Wt. %	Comp.	Wt. %	Comp.	Wt. %	Comp.	Wt. %
Al	96.4	Al	98	Al	89	Al	90
Cr	0.05 - 0.2	Cr	0.04 - 0.35	Cr	Max 0.04	Cr	0.18 - 0.28
Cu	Max 0.1	Cu	0.15 - 0.4	Cu	1.9 - 2.5	Cu	1.2 - 2
Fe	Max 0.4	Fe	Max 0.7	Fe	Max 0.15	Fe	Max 0.5
Mg	2.4 - 3	Mg	0.8 - 1.2	Mg	2 - 2.7	Mg	2.1 - 2.9
Mn	0.5 - 1	Mn	Max 0.15	Mn	Max 0.1	Mn	Max 0.3
Si	Max 0.25	Si	0.4 - 0.8	Si	Max 0.12	Si	Max 0.4
Ti	Max 0.2	Ti	Max 0.15	Ti	Max 0.06	Ti	Max 0.2
Zn	Max 0.25	Zn	Max 0.25	Zn	5.9 - 6.9	Zn	5.1 - 6.1
				Zr	0.08 - 0.15	Zr+Ti	Max 0.25

Table 4-2 Nominal composition of the aluminum alloys 5454, 6061, 7050, and 7075.

4.1.1 Welding on the Vertical Milling Machine

Single-pass butt welds on the displacement controlled vertical milling machine required generally four steps. First, two aluminum plates were clamped onto a steel backing plate on the movable table of the milling machine. The clamping prevents unintentional movement of the plates during welding. Second, the rotating FSW tool was slowly plunged into the faying surface of the two plates. The end of the plunging step corresponded to a constant initial backing plate-to-pin clearance of 0.08 mm with the milling machine unloaded. The third step was considered as the actual welding. The rotating FSW tool started moving at the welding speed relative to the two plates to be welded. For all welds, a constant tool-to-workpiece normal angle was maintained at approximately 2.5 degrees. The setup provided adequate forging pressure at the heel of the tool shoulder for full weld consolidation and maintained close enough clearance between the bottom of the pin and the backing plate to promote full penetration of the dynamically recrystallized zone. At the forth and last step of a friction stir weld, the rotating tool is retracted form the weld after stopping the translational table movement of the milling machine. A hole was left in the weld at the location of the tool at the end of welding.

4.1.2 FSW Process Development System PDS

The Process Development System (PDS) built by MTS Systems Corporation in 2000 is a customized machine for friction stir welding. Control (or welding) parameters are the spindle speed, the welding speed, and the vertical force on the tool. In contrast to displacement controlled welding with a fixed pin clearance, load controlled welding required the new welding parameter, the vertical force, which is also called z-force. The z-force was optimized for each weld dependent on the rotational velocity, the welding speed, the base material, and the plate thickness by judging the weld surface. An optimal z-force provided enough forging pressure for fully penetrated welds without excessive flash at the top surface.

RPM	WS (mm/s)	Z-Force (kN)	Weld Pitch (mm/rev)
240	1.279	22.24	0.32
240	2.36	26.69	0.59
240	3.3	28.02	0.825
390	1.23	21.35	0.189
390	2.36	22.24	0.363
390	3.3	28.91	0.508

Table 4-3 Welding parameters for friction stir welds in 8.128 mm thick AA6061-T6 plates using the FSW tool #1 (9.9 mm and 25.4 mm pin and shoulder diameter, respectively). The tool to workpiece angle was 2.5 degree in all welds.

Table 4-3 lists the welding parameters that were used in 8.128 mm thick, butt-welded AA6061-T6 aluminum plates. All welds were performed with the standard tool described in Section 4.1 (9.9 mm and 25.4 mm pin and shoulder diameter, respectively), which was tilted 2.5 degree from the vertical axis. The data of these welds presented in Section 7.4.3.1 is used for comparison with corresponding 2-D and 3-D FSW process models, respectively.

Friction stir welds were also performed in AA7050-T76 at three constant weld pitches but equally changing the rotational and the welding speed as listed in Table 4-4. The specific weld energy is compared in Section 7.4.4.1 with corresponding 2-D model results.

WP=282 mm/rev			WP=0.423 mm/rev			WP=0.564 mm/rev		
RPM	**WS [mm/s]**	**Z-Force [N]**	**RPM**	**WS [mm/s]**	**Z-Force [N]**	**RPM**	**WS [mm/s]**	**Z-Force [N]**
180	0.85	22240	180	1.27	24464	90	0.85	28912
270	1.27	23574	240	1.69	24464	135	1.27	28912
360	1.69	25800	360	2.54	31136	180	1.69	26688
540	2.54	35584	540	3.81	35584	270	2.54	37808
630	2.96	35584	720	5.08	37808	315	2.96	37808
810	3.81	35584				405	3.81	46704

Table 4-4 Welding parameters of the AA7050 friction stir welds at three constant weld pitches.

Three partially penetrated friction stir welds were performed in a 25.4 mm thick AA6061-T6 plate using a so-called zero-degree tool. The FSW typical tool to workpiece angle was avoided adding features to the tool shoulder that prevent the rotating tool from excessive out of the vertical line rotation. Scrolls were machined in the tool shoulder such that material is moved from the outer shoulder diameter towards the center of the tool. An advantage of the zero-degree tool is the better suitability for industrial welding where friction stir welds on three-dimensional panels are performed. The shoulder diameter in of the zero-degree tool was 33 mm. The pin was a non-threaded 10 mm long cylinder with a diameter of 12.7 mm. The welds performed with the zero-degree tool were especially thought for the validation of thee-dimensional, numerical process models. It is worth mentioning that the pin and shoulder diameter as well as the pin length were 25 % larger than in the standard tool described above.

Case	RPM	WS (mm/s)	Z-Force (kN)	Weld Pitch (mm/rev)
1	232	2.35	31.14	0.607
2	390	2.35	28.91	0.362
3	464	2.35	26.69	0.304
4	540	2.35	24.46	0.261

Table 4-5 Welding parameters for the zero-degree welds in 25.4 mm thick AA6061-T6.

During welding, the PDS recorded a number of friction stir welding relevant data. Measurements include the time, the distance, the longitudinal and vertical force, the spindle and welding speed, as well as plunge depth, and the hydraulic pressure difference at the spindle. The forces were measured using load cells. The hydraulic oil pressure difference at the spindle motor was converted to torque. The measured torque included the torque required for free spindle rotation, which was subtracted. The torque at the tool was then calculated from the product of the net spindle torque and the motor efficiency, which depended on the rotational spindle speed. The motor efficiency accounted among others for the mechanical losses in bearings and oil leaks in the pressure tubes. It was assumed that the mechanical work of the PDS corrected by the motor efficiency was put into a friction stir weld. Hence, the power of a weld was calculated from the product of spindle speed and torque.

The measured data such as forces and power was used for comparison and validation of the numerical FSW process model presented in the chapters 7 and 8.

4.2 The Marker Insert Technique

The material flow in friction stir welds was visualized using the marker insert technique. A total of six 2.7 mm high, 1.8 mm thick, markers were placed in the weld path in order to gain information about the overall material transport and detailed information about flow variations through the thickness of the plates. The marker inserts were made of an aluminum alloy with different etching characteristics than the base material. Inserts were placed on both the advancing and the retreating sides, at three different heights covering the top, middle and bottom thirds of the plate. Inserts were staggered along the weld line so that the possibility of mixing of the markers from different positions was eliminated. The length of the markers was such that some of the marker, remote from the weld line, extended beyond the TMZ and was not deformed by the welding process. Markers were placed by milling narrow slots into the faying surface and press-fitting the markers into the slots. For the markers that were placed in the middle third of the plate, a base metal shim of similar size to the marker was press fit into the upper third of the plate above the marker. Figure 4-1 shows schematically the configuration of the six inserts which, when put together, cover the total height and width of the welded zone.

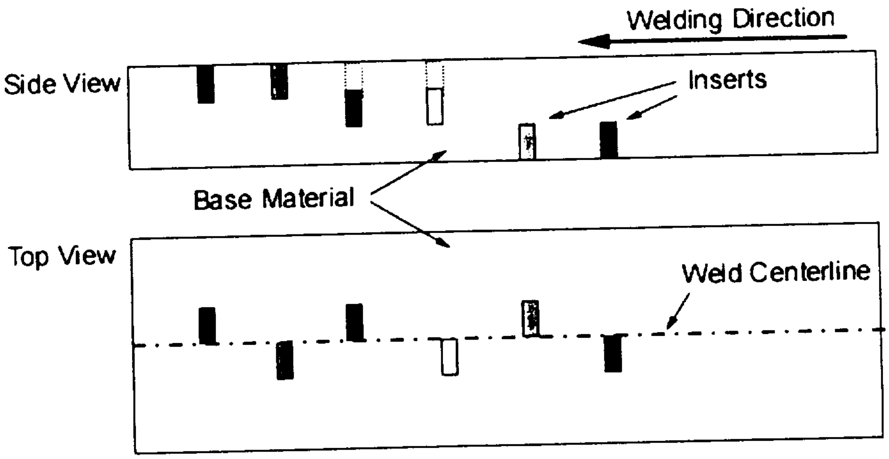

Figure 4-1 Schematic view of the placement of the six markers. Two markers were placed at the top, middle, and bottom of the plates, respectively, and were staggered on advancing and retreating side.

The marker flow was elucidated by milling off successive slices, 0.25 mm thick, from the top surface of the weld. After each cut the surface was etched with Keller's reagent and digital images of the region surrounding each marker were obtained. Due to the etching process, the alloy rich in copper turned dark whereas the other alloy was relatively unaffected by the etchant. The pixel positions of the markers were extracted from the digital images of each marker (a total of six) at each level (up to 32 per weld). Combining the data from all six markers, a three-dimensional visualization of the deformed markers, similar to a CT scan was obtained. The 3-D plot gives the final position of a thin layer (1.8 mm thick) that was originally perpendicular to the welding direction. The digital camera has an aspect ratio of vertical ratio of 0.8533 (ratio of the vertical to the horizontal axis). The spatial calibration was based on the marker thickness (1.8 mm). The extracted pixel positions in from the images were converted to real distances using spatial calibration and the aspect ration. Additionally, the position of the centerline was marked in each weld as a reference line.

Weld	Tool	Pin Diameter (mm)	Shoulder Diameter (mm)	RPM	WS (mm/s)	Weld Pitch (mm/rev)
38	1	9.9	25.4	232	2.35	0.61
45	5	12.0	25.4	232	2.35	0.61
46	6	7.8	25.4	232	2.35	0.61
47	4	9.9	20.3	232	2.35	0.61
48	3	9.9	30.5	232	2.35	0.61
74	1	9.9	25.4	397	3.3	0.5
75	1	9.9	25.4	397	2.35	0.35
76	1	9.9	25.4	397	1.279	0.19

Table 4-6 Tool and weld parameter details of the AA2195-T8 welds.

The marker insert technique was first applied to friction stir welds in AA2195-T8 using AA5454-H32 as marker inserts. Here, the base material is rich in copper whereas the marker contains almost no copper. For each weld made, the pin and shoulder diameter as well as the rotational and welding speed are listed in Table 4-6.

The weld pitch is defined as the tool advance per revolution (welding speed / rotational speed). However, although the weld pitch is an important factor, welds made with the same pitch may have differing energy inputs, in particular, for two welds with the same weld pitch, the weld with the higher welding speed and RPM will in general be "colder" than one with lower welding speed and RPM. It is important to note that all of the welds studied were essentially defect free and exhibited similar properties to each other when tested in transverse tension [51].

The marker insert technique was also used to visualize the material flow in the aluminum alloys 2024-T351, 2219-T87, 5083-O, 6061-T6, 7050-T73, 7075-T7351. AA5454-H32 markers were inserted in welds of aluminum alloys of the 2XXX and 7XXX series. In the AA5083 and AA6061 welds, AA2024 and AA7075 were used as the marker material, respectively. In addition to the 6 markers previously described, 2 markers covering the total height were placed at the same location on advancing and retreating side, respectively, such that one marker was covering the whole weld zone when the plates were clamped on the backing plate. For the purpose of data reduction, the welds were milled off in 0.5 mm thick slices. Consequently, digital images of the seven markers were taken at 16 layers throughout the weld height.

The welds were performed at three different sets of welding parameters listed in Table 4-7, which are categorized as "cold", "nominal", and "hot". Note that the welding condition "nominal" and "hot" are the same as for Weld 75 and 76 (Table

4-6), respectively. The "hot" welds in AA5083-O and AA6061-T6 were performed at 637 and 832 RPM, respectively. 232 RPM were used in the "nominal" AA2219 weld.

Condition	Alloys	RPM	WS (mm)	Weld Pitch (mm/rev)
Cold	2024, 2219 5083, 6061 7050, 7075	232	3.3	0.853
Nominal	2024 5083, 6061 7050, 7075	397	2.35	0.355
Hot	2024, 2219 7050, 7075	397	1.279	0.185

Table 4-7 Welding parameters of the "cold", "nominal", and "hot" welds for the flow visualization of the 2XXX, 5XXX, 6XXX, and 7XXX aluminum alloys.

5 Flow Visualization with the Marker Insert Technique

The detailed analysis of the material flow pattern in FSW for several welding conditions and different aluminum alloys is presented in this chapter. The structure of this chapter is the following. Some general aspects of the material transport are discussed with the example of Weld 38, a relatively "cold" weld (weld pitch 0.61 mm/rev) in AA2195-T8. The effects of varying welding parameter, different pin and shoulder diameters in AA2195-T8, respectively, are shown in the Sections 5.2, 5.3, and 5.4. Thereafter, in Section 5.5, the flow characteristics of the alloys AA2024, AA7050, AA5083, and AA6061 are presented usually for three sets of welding parameters to study the effect of different weld energy on the material flow.

In the following the x-, y-, and z-axis refer to the welding direction, the transverse direction, and the weld height, respectively. All welds had some general material flow patterns in common. The flow is not symmetric about the weld centerline. The flow patterns on advancing and retreating side are different because the relative velocities between the tool and workpiece are different on both sides. The marker insert technique does not directly provide information on the actual flow path of the material because it shows only the final position of the markers in the weld.

5.1 The General Flow Pattern

Figure 5-1, 5-2, and 5-3 illustrate the process by which the images from separate markers are combined to provide a full 3-D view of material flow. Figure 5-1 is an image of the etched marker from the advancing side of Weld 38 at a height of 4 mm in the weld (near the mid-plane). Figure 5-2 is from the same height in Weld 38, but is an image of the corresponding retreating side marker. The vertical line in both Figures 5-1 and 5-2 indicates the weld centerline. In Figure 5-3, the marker position data, extracted from Figure 5-1 and Figure 5-2, have been combined into a single, binarized, image. The images were combined so that the undeformed markers on the advancing and retreating sides were aligned (vertical alignment as seen in the images) and so that the weld centerline from both images is coincident (horizontal alignment). No overlap between the advancing and retreating side markers was observed, but when combined, the two markers form a continuous path from the advancing to retreating sides in Weld 38.

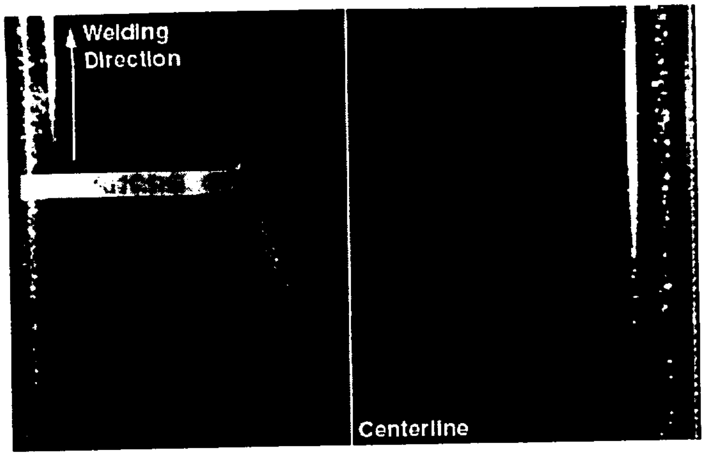

Figure 5-1 Picture of the advancing side marker at the middle height (z=4mm) of Weld 38. Rotation direction was clockwise. The bulk of the marker was transported against the welding direction. However, a small amount was moved forward at the edge of the pin.

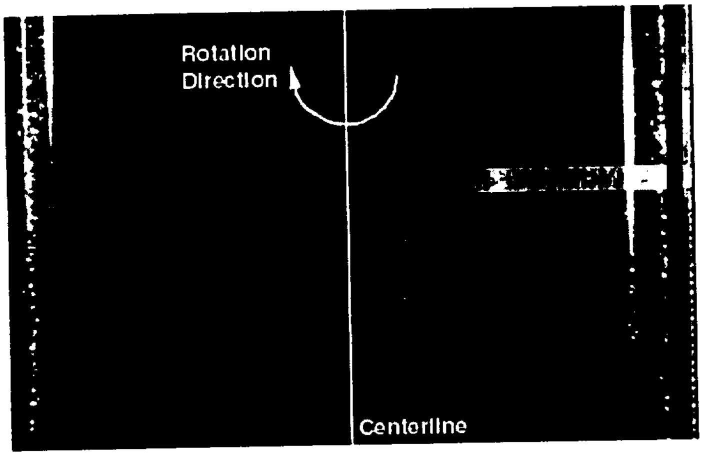

Figure 5-2 Picture of the retreating side marker at the middle height (z=4mm) of Weld 38. This marker was transported against the welding direction, only.

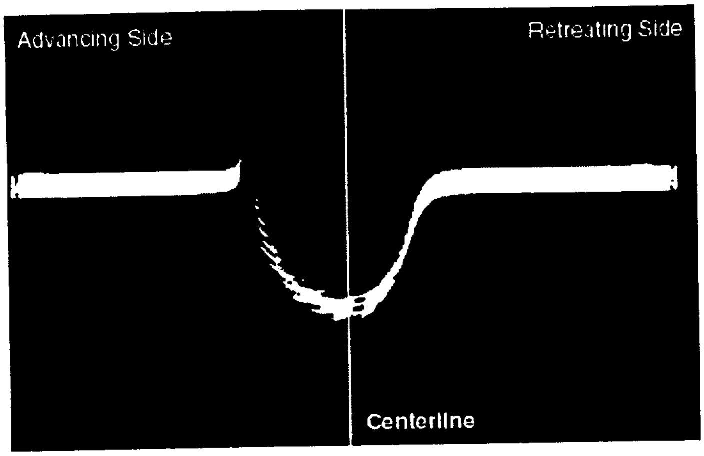

Figure 5-3 The images of the advancing (Figure 5-1) and retreating side (Figure 2-1) markers are combined and binarized in one image (c) at the middle of Weld 38 (0.61 mm/rev). The tool rotation was clockwise.

The bulk of the marker material was moved to a final position behind its original position and only a small amount of the material on the advancing side was moved to a final position in front of its original position. No material was transported further backwards than one pin diameter behind its original position. It is important to mention that in a "cold" weld as Weld 38, the material flow as presented in Figure 5-3 is characteristic for the material flow throughout the weld height, except for the region close to the tool shoulder. However, the width of the deformed zone decreases towards the bottom of the weld because of the curved lower end of the pin. FSW can be roughly described as an in-situ extrusion process where the tool shoulder, the pin, the backing plate, and the cold base material form an extrusion die. It is nowadays well accepted that all the material, originally within the pin diameter, is passing the tool on the retreating side [55], [63], [68]. Experiments and numerical models have successfully shown that material is moved in rotation direction (here clockwise) around the tool to its final position.

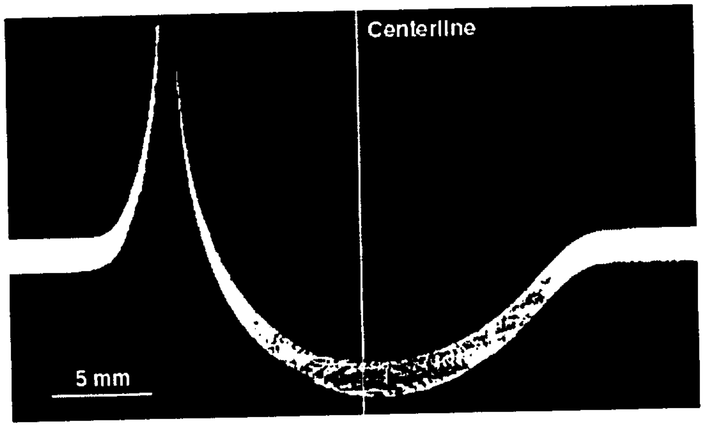

Figure 5-4 The deformed markers just below the tool shoulder at z=8mm in Weld 38.

The flow pattern close to the broad shoulder is different than observed in lower heights of the weld. Figure 5-4 shows the assembled markers from advancing and retreating side close to the top surface of Weld 38 at a height of 8 mm. Near the top of the weld, because of the shape of the tool, a substantial amount of material is moved from the retreating side of the weld to the advancing. The advancing side marker is transported only in welding direction at z=8 mm. The movement of material from the retreating to the advancing side causes vertical mixing in the weld and a complex circulation of material around the longitudinal axis of the weld. The amount of vertical material flow in the weld is strongly correlated with the weld energy of the weld and is discussed in detail in Section 5.2.

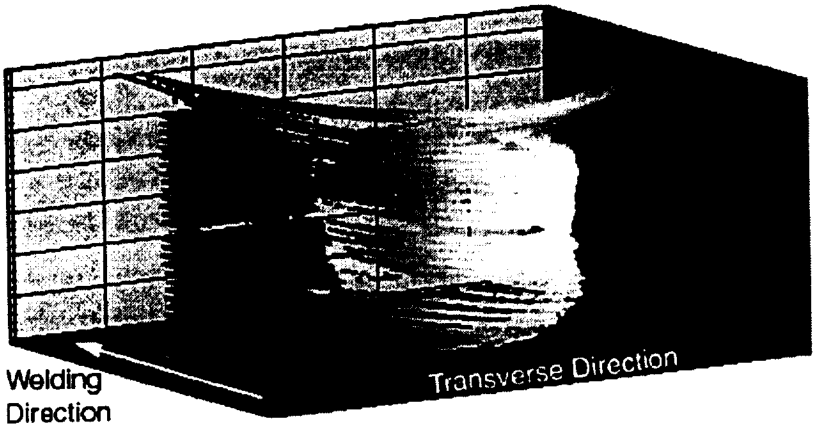

Figure 5-5 Three-dimensional plot of the markers in Weld 38 (0.61mm/rev). The weld height (vertical axis) is magnified by a factor of 2.5. The markers are continuous after welding. The bulk of the material was transported against the welding direction behind its original position. Material transport in welding direction occurred only at the advancing side of the tool.

The assembly procedure was performed for each of the 30 to 32 levels in each weld. Combining the data of all detected marker positions at all 30 - 32 levels, one obtains three-dimensional plots: one of these 3-D plots for Weld 38 is shown in Figure 5-5. In Figure 5-5, the welding direction is into the plane of the paper and the contour variable (represented by the shade of gray applied to a data point) is the y-coordinate or position along the weld line. The z-axis of the plot is the height in the weld and is magnified by a factor of 2.5. One can see that the markers, assembled as described above, are continuous after welding. The bulk of the material is transported to a position behind its original position, but none by more than one pin diameter. In the top third of the weld, a substantial amount of material is transported forward of its original position (in the direction of welding), presumably by the action of the shoulder. This forward transport occurs for material originally on both the advancing and retreating sides, however, all of the material transported forward ends up on the advancing side of the weld. At lower levels in the weld, where the influence of the shoulder is diminished, only a small amount of marker material on the advancing side, slightly more than a pin radius from the weld centerline, was detected in front of its original position.

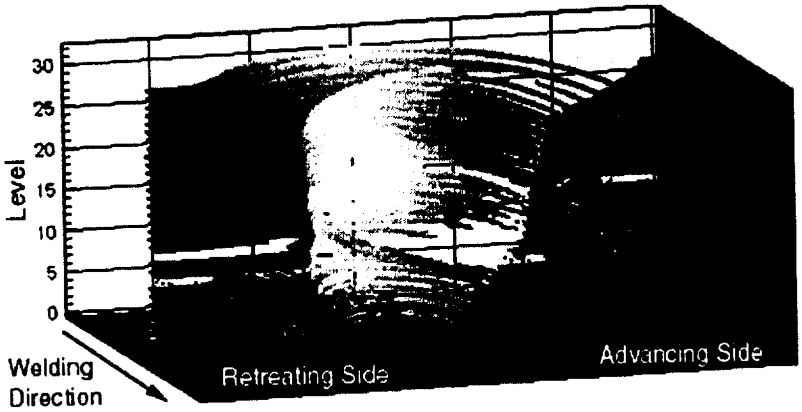

Figure 5-6 Front view of the 3-D plot of the deformed markers in Weld 38.

The 3-D plot of the markers is seen in a view against the welding direction in Figure 5-6. Note the apparent gap in the lower third of the advancing side. Here, material in this area is distributed over a wide range in the horizontal plane.

The material flow in the lower third of the weld height is different from the backward transported material, which is predominant elsewhere. Several flow features can be seen in Figure 5-7, which shows the bottom marker on the advancing side at z=2 mm. First, material extruded around the pin was deposited over a wide range in the welding direction. The marker was detected at positions even in front of its original indicating forward transport within the weld nugget region. Second, the insert was deposited in a serrated form where base material is "mixed" in the marker. The distance between two jagged peaks corresponds exactly to one weld pitch (0.61 mm). The serrated form of markers, deposited in the lower two-thirds of the advancing side, occurs in most (if not all) welds. However, the mechanisms of formation of the serrations are not known. Third, material at the edge of the weld nugget is transported in a thin layer in welding direction to positions in front of its original.

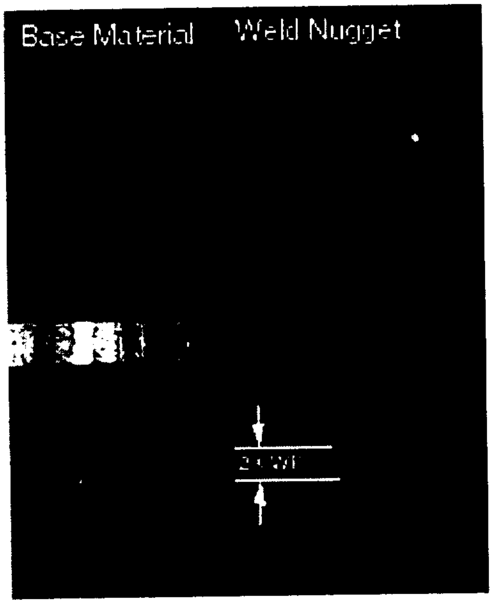

Figure 5-7 Marker from the advancing side of Weld 38 at z=2 mm.

A reason for the marker distribution over a wide range in the horizontal plane might be the contact time of the marker with the tool. It will be shown in the following sections that in welds with higher weld energies the marker from the top (mostly of the advancing side) is pushed down to the lower third of the weld height. Material originally from the top being deposited close to the bottom of the weld will most likely "travel" the longest distance during welding. Hence, the highest degree of mixing is expected in this region. The widespread deposited marker at lower weld heights (mainly on the advancing side) as shown in Figure 5-7 occurred in all welds presented in this chapter. Therefore, Figure 5-7 shall be taken as a representative picture for the flow phenomenon in this region even though the pattern of deposited material may vary from one weld to the other.

a) Markers before welding

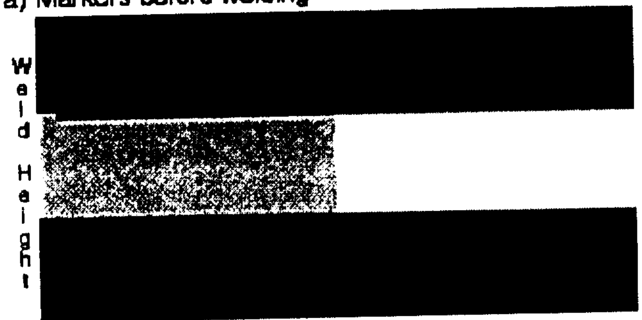

b) Markers after welding

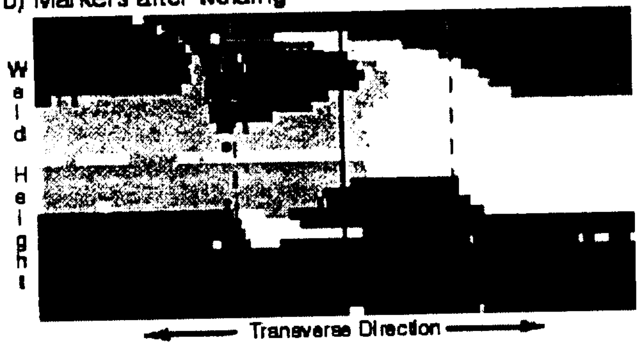

Figure 5-8 Vertical mixing in Weld 38 (0.61 mm/rev). The markers are projected in the vertical plane viewing in welding direction. (a) shows the undeformed markers before welding and (b) shows the vertically mixed six markers after welding. The solid and the dashed lines denote the centerline and the pin diameter, respectively.

A 3-D plot, as shown in Figure 5-5 gives no information about the vertical mixing of the 31 layers. A projection of the marker positions onto a vertical plane in the welding direction is best suited to give detailed information about the vertical material flow. Figure 5-8 shows the six markers before (Figure 5-8a) and after (Figure 5-8b) welding. A different gray scale level has been assigned to each marker so that the post-welding position of each marker may be determined in the plot. Note that the bulk of the material, e.g. inside the pin diameter (dashed lines), was transported towards the observer, which is equivalent to the material transport backwards relative to the welding direction. Material is pushed downwards on the advancing side and moved upwards towards the top at the retreating side within the pin diameter. It is believed that the counterclockwise material movement around the longitudinal axis is initiated by the material transport due to the rotation of the tool shoulder at the crown of the weld. At the crown, material from the retreating side was transported to the advancing side occupying space on the advancing side. Since FSW is a nominally constant volume process and the shoulder, the pin, and the undeformed base material restrict the flow path, the transport of material from the retreating to advancing sides by the shoulder causes material from the top of the advancing side to move downward within the pin diameter. Closer to the root of the weld, the material transport is restricted by the backing plate; therefore, an upward motion is detected on the retreating side within and near the pin radius. The net result of the upward and downward material flows is a circulation about the longitudinal axis of the weld.

It is important to realize that the vertical circulation is a secondary motion, overlaid over the primary material transport in rotation direction around the rotating tool in the horizontal plane of the weld. Considering only markers on the retreating side, it seems obvious that material is moved (extruded) in the rotation direction around the pin. However, using the marker insert technique, no statement can be made about the flow path of material on the advancing side. Both, flow around the advancing and the retreating side is conceivable but nothing indicates the true flow path. However, the process models presented in the chapters 6, 7, and in 8 as well as other published literature (e.g. [55] and [63]) agree that material, originally within the pin diameter, is transported around the retreating side only. Additionally, the marker insert technique does not provide any information about how often material rotates with the tool before it ends at its final position. After all, the tool completes 3 rotations within 1.8 mm (the thickness of the inserted markers) and about 19 rotations before the tool has traveled 11.7 mm (pin diameter + marker thickness) at a weld pitch of 0.61 mm/rev and a pin diameter of 9.9 mm. For example in Figure 5-7 (in the lower part on the advancing side) 25 jagged peaks are visible. The distance between each corresponds to the tool advance per one revolution (0.61mm). Hence, material was deposited during 25 revolutions at this particular level (z=2mm).

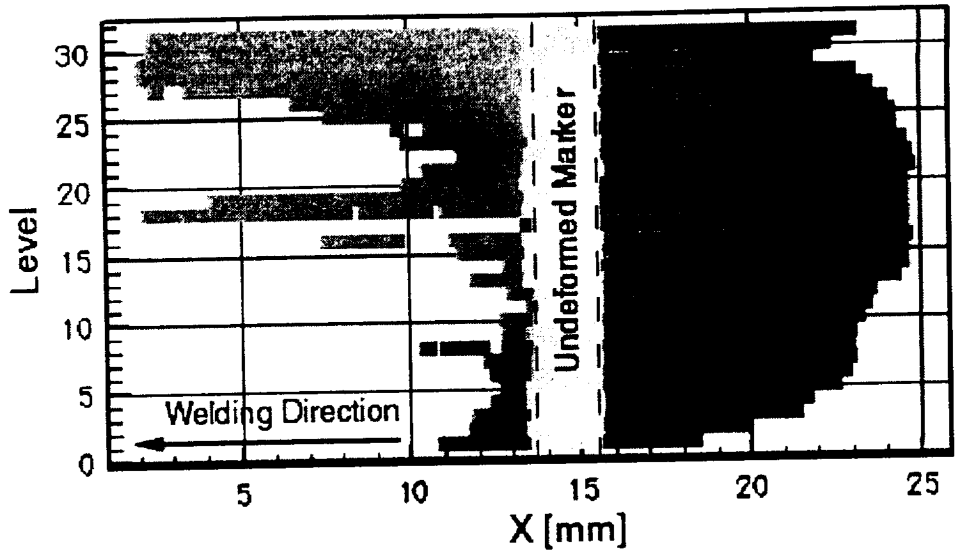

Figure 5-9 Side view of the 3-D plot (Figure 5-5) from the advancing side.

The side view from the advancing side on the 3-D plot of Figure 5-5, as shown in Figure 5-9 for Weld 38, provides more detailed information about the material flow in and against welding direction. The dashed lines (at x=13.8 mm and x=15.6 mm) denote the original position of the marker inserts. Most material transport in welding direction occurs at the top of the weld (on the advancing side only). Material dragged along with the pin in welding direction at low levels (Figure 5-7) can almost not be seen in Figure 5-9 (at level 8) but is more obvious in a weld shown in the next section. The bulk of the material is transported against the welding direction. The maximum deformation against the welding direction occurs just above the middle of the weld height. The transport against the welding direction at the top is smaller than at middle heights. Presumably high pressure on the trailing side of the tool shoulder prevents material at the top from a larger backward flow. The minimum backward transport at the top of the weld occurs where the vertical circular material transport interacts with the retreating side material flow caused by the rotating shoulder. The two perpendicular circular motions cause the observed flow pattern.

5.2 Weld Pitch Effects

In this section, the material flow patterns in the Welds 38, 74, 75, and 76 are compared. The weld pitches listed in Table 4-6 for Welds 74, 75, and 76 indicate that each of these welds is hotter than Weld 38 and that the hottest of these welds is Weld 76 followed by Weld 75 and then by Weld 74. The increased heat inputs in these welds result in increased volumes of material involved in the material transport as well in intensified vertical material transport.

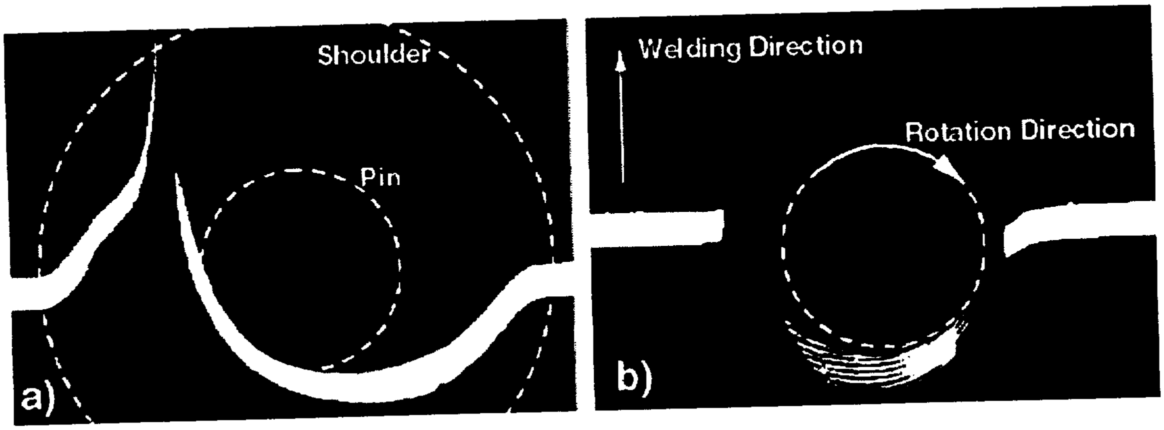

Figure 5-10 Combined markers of Weld 75 (WP=0.355 mm/rev) at the top (a) and the middle (b) of the weld.

Figure 5-10 shows the deformed markers of Weld 75 at a height of 4 mm (a) and 8 mm (b), respectively. The dashed lines indicate the pin and shoulder diameter, respectively. The material flow in Weld 75 is different from that shown in Weld 38. Weld 75 and 38 were welded with the same tool and the same welding speed but different rotational velocities. The flow pattern at the top surface is similar to the one shown in Figure 5-10, except for the kink in the forward transported marker on the advancing side (on the left side of Figure 5-8 a). The markers on the advancing and the retreating side, placed at the middle height, of the weld do not cover the whole width of the welded zone as shown in Figure 5-10 b). The images of the middle markers do not reveal the whole story. Vertically transported material from other levels (material which is pushed upwards and downwards) fills the gaps. Therefore, all 6 markers detected at z=4 mm need to be included in the analysis. Using the data extracted from the digital images, all markers, present at one level, can be plotted at once. Figure 5-11 shows that the markers are continuous after welding as shown for Weld 38 in Figure 5-3 with the exception that all six markers are mixed in the mid plane of Weld 75.

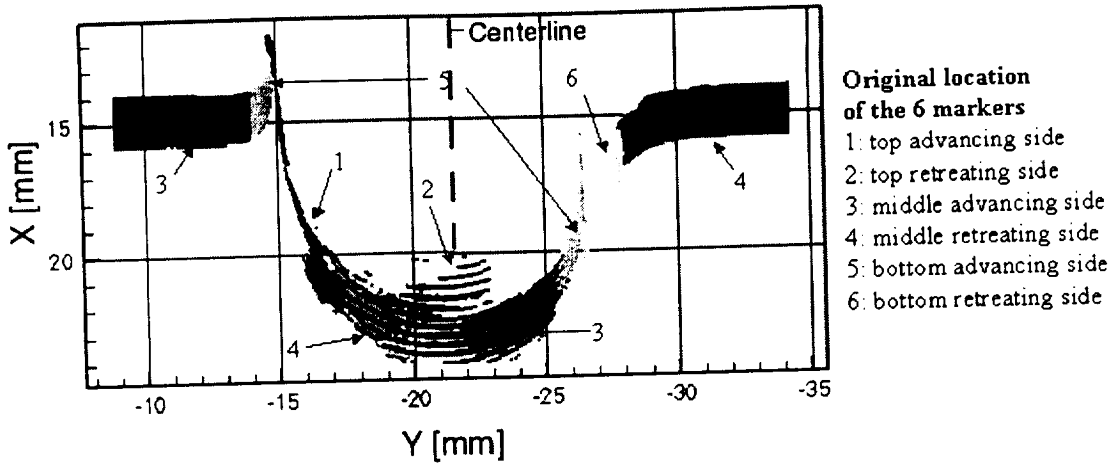

Figure 5-11 All the 6 markers were detected at the mid-plane (z=4mm) in Weld 75. The plot is created from the extracted pixel positions of the 6 markers at z=4mm.

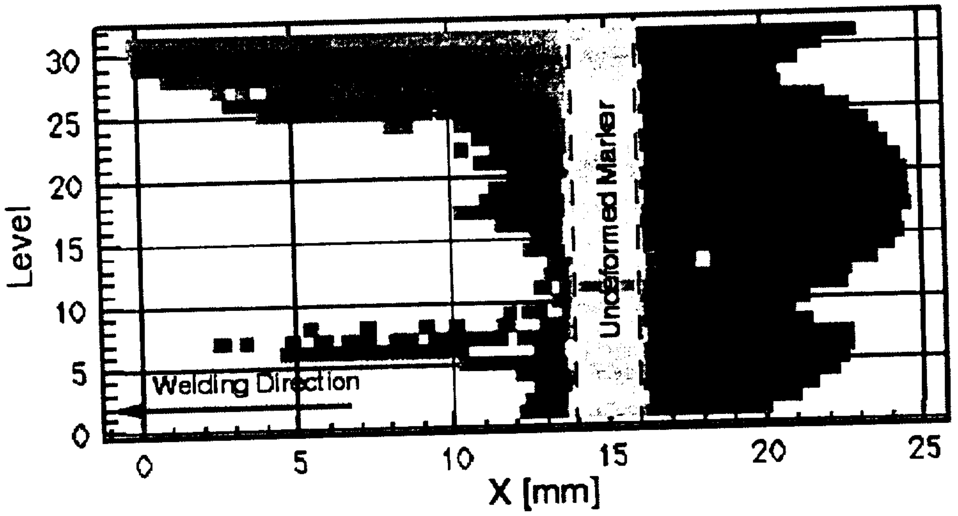

Figure 5-12 Side view from the advancing side of the 3-D plot of Weld 75.

Figure 5-12 illustrates the forward and backward transport of material in Weld 75. The picture shows the view from the advancing side on the 3-D plot of Weld 75.

Material movement in welding direction to positions in front of its original occurs on the advancing side (note that Figure 5-12 does not reveal the difference between advancing and retreating side) in two regions namely in the upper part and in the lower third of the weld. Material movement at the top of the weld is caused by the broad shoulder and is already discussed in detail for Weld 38. Material movement in the lower third of the weld is also already described for Weld 38 in Figure 5-7 and Figure 5-9. In Weld 75 (performed at the same welding speed but a higher RPM as Weld 38) the shape of the 3-D plot has changed in the lower third of the weld (level 6, 7, 8 in Figure 5-12 correspond to approximately 2 mm from the bottom surface). The material transport against welding direction is minimal in this part. Markers from the bottom and from the top of the advancing side are deposited in the horizontal plane at $z = 2$ mm in a similar serrated form as shown for Weld 38 in Figure 5-7. The marker insert technique does not reveal the actual flow path of the material to its final position. However, the flow pattern seen in the lower third of the weld is a result of the extrusion in FSW accompanied by the complicated vertical flow.

Since the projection of the markers onto the vertical plane in the welding direction offers the most valuable characterization of the welds, in this and the following sections other views of the deformed markers will be shown only where necessary. Figure 5-13 shows the differences in the mixing for Welds 74, 75, and 76. The general pattern of material flow in each of Welds 74, 75, and 76 is consistent with the flow pattern described in the previous section for Weld 38 (Figure 5-8). Material within the pin diameter experiences a counterclockwise rotation around the longitudinal axis during the transport backwards to its final position in the weld. Outside the pin diameter, material is transported towards the top of the weld with flow in and opposite the welding direction on advancing and retreating sides, respectively.

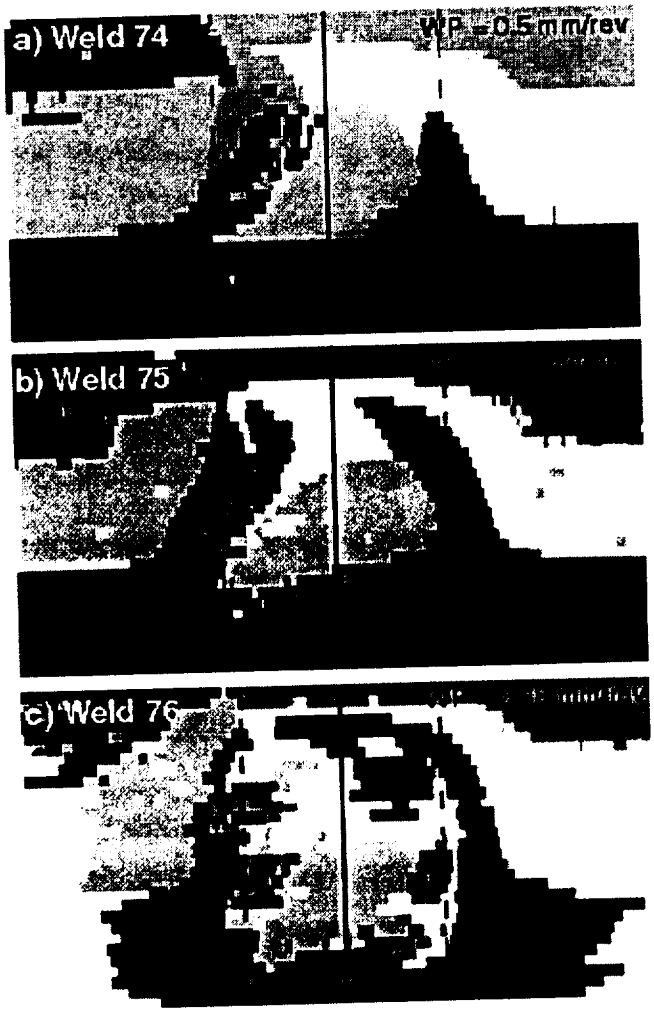

Figure 5-13 Vertical mixing in Weld 74 (a), Weld 75 (b), and Weld 76 (c). The mixing increases with decreasing weld pitch (increasing specific weld energy, here: increased tool rotation). The dashed lines denote the pin diameter, which was the same for the three welds.

The effect of decreasing the weld pitch on the vertical mixing within the welds can be clearly observed by examining the final positions of the lower retreating side marker for Welds 38, 74, 74, and 76 corresponding to weld pitch changes from 0.61 mm/rev to 0.19 mm/rev (Figure 5-8 and Figure 5-10). As the weld pitch decreases (and weld energy increases) the portions of the bottom marker on the retreating side move higher and higher in the weld. In Weld 74 (highest weld pitch) it can be seen that the retreating side bottom marker is being pushed upward, however, it does not reach to the mid-plane (in z direction). In the weld with the lowest pitch, Weld 76, the marker is entrained in the flow arm and pulled completely across the top of the weld nugget. At the intermediate weld pitches, the markers are displaced upward less than in Weld 76 and more than in Weld 38. In simple terms, the amount of vertical displacement of the retreating side bottom marker is inversely proportional to the weld pitch.

Although the reason for the increased mixing which accompanies decreasing weld pitch is not certain, the higher energy input may result in softening of a greater volume of material in the weld zone thereby facilitating material transport. Alternatively, the increased vertical transport at lower weld pitch may be due to the auguring effect of the threads acting on a given volume of material for a greater time (rotation is such that the threads push material down).

5.3 Pin Diameter Effects

Welds 38, 45, and 46 were performed with the same tool rotation rates and welding speeds (weld pitch = 0.61 mm/rev), but with different tools, all having the same shoulder diameter of 25.4 mm. As shown in Table 4-3, Welds 38, 45, and 46 were made using pin diameters of 9.9, 12, and 7.8 mm respectively. In Figure 5-14a-c the final marker positions are projected onto the y-z plane of the weld so that the transport of the marker material may be observed. In Weld 46 performed with the smallest pin (Figure 5-14a), the interface between the advancing and retreating side markers is near the weld centerline in the lower two-thirds of the weld. Only near the crown of the weld, where the influence of the shoulder is important, does a substantial amount of material cross the centerline. In Weld 38, (Figure 5-14b) made using the 9.9 mm diameter pin, a larger amount of material crosses the centerline in the bottom third of the weld due to the circulation about the longitudinal axis of the weld. Figure 5-14c shows that in Weld 45, a substantial amount of material crosses the weld centerline from advancing to retreating sides in the bottom two thirds of the weld. The increased material transport across the weld centerline caused by the use of larger diameter pins may result from an increase in weld energy at constant rotational and welding speed. It seems likely that more work goes into a weld made with a large pin than with a small pin: the nugget size increases as the pin size indicating that more material undergoes severe plastic deformation when a large pin is used. Measurements by Reynolds and Tang [69] have shown that the power delivered to the welds increased with increasing pin diameter.

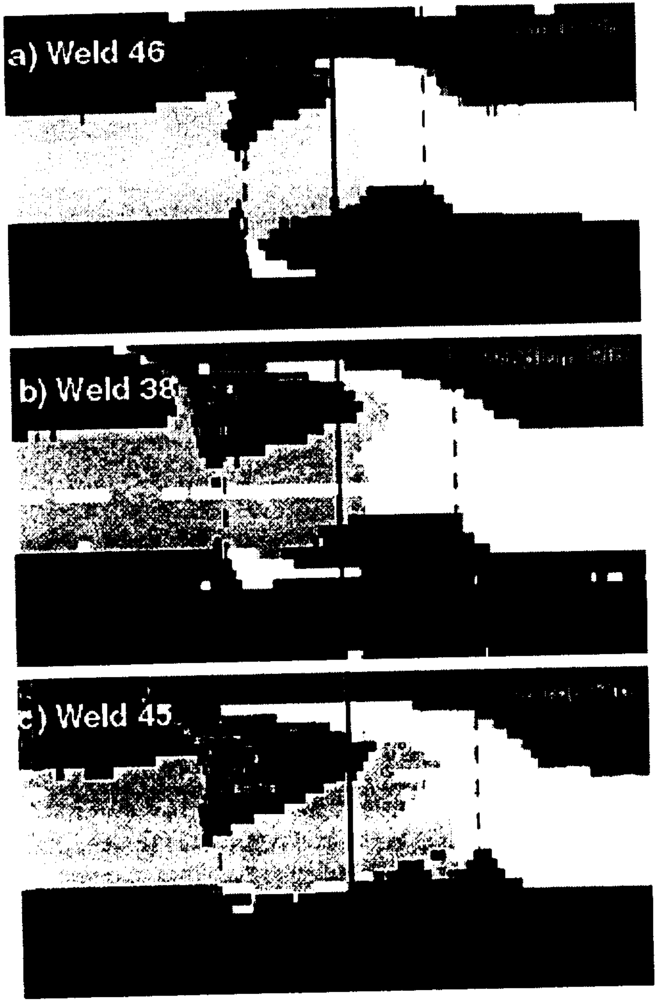

Figure 5-14 Vertical mixing for different pin diameters in Weld 46 (a), Weld 38 (b), and Weld 45 (c). Increasing the pin diameter increases the vertical mixing. Almost no vertical mixing occurred in Weld 46 (a), i.e. the interfaces between the three layers are almost horizontal. In Weld 38 (b) and in Weld 45 (c), an increasing amount of material was pushed downwards on the advancing side and upwards on the retreating side.

5.4 Shoulder Diameter Effects

AA2195-T8 was also welded varying only the shoulder diameter. As listed in Table 4-3, Welds 47, 38, and 48 were performed at the same rotational and translational velocities (WP=0.61 mm/rev) as well as the same medium pin diameter (9.9 mm) but with a 20.3 mm, 25.4 mm, and 30.5 mm shoulder diameter, respectively. Figure 5-15 shows the vertical flow patterns of the three welds. Even though the welds were performed at a high weld pitch of 0.61 mm/rev [1]some distinct differences exist. With increasing shoulder size more material at the top of the weld is transported from the retreating to the advancing side. More material is pushed towards the root on the advancing side causing more circulation around the longitudinal axis. The influence of the increased shoulder diameter can be best seen at the deviation of the centerline from the connection of advancing and retreating side markers. In Weld 47, performed with the smallest shoulder diameter, advancing and retreating side markers are connected closest to the centerline. Note, how especially in Weld 48 the marker on the bottom of the retreating side is pushed upwards and stays clearly on the retreating side.

It is believed that the effect of decreasing weld pitch as shown in Section 5.2 is even more dominant with larger shoulder diameters since the material transport close to the tool shoulder is important for the vertical mixing in friction stir welding. However, the marker insert technique was not used to visualize the material flow in welds with varying shoulder diameters at different welding parameters.

---

[1] As shown in the previous sections, the weld pitch of 0.61 mm/rev produced the least amount of vertical mixing for the range of weld pitches that were investigated.

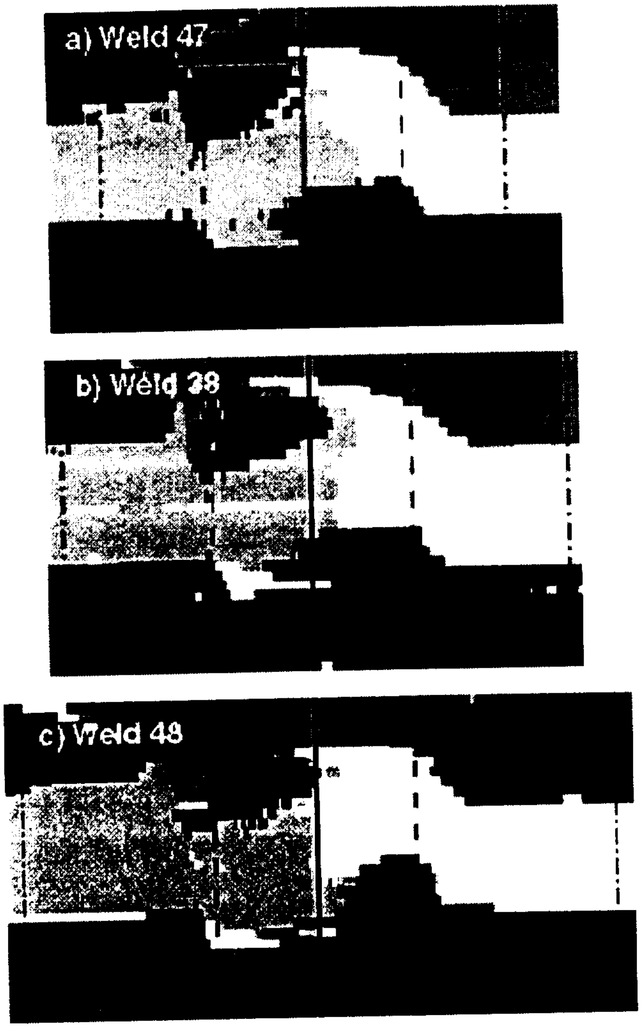

Figure 5-15 Vertical mixing for different shoulder diameters in Weld 47 (a), Weld 38 (b), and Weld 48 (c). With increasing shoulder diameter a larger volume of material is transported from the advancing to the retreating side. Therefore, the vertical mixing is increased. From Weld 47 (a) over Weld 38 (b) to Weld 45 (c), an increasing amount of material is pushed downwards on the advancing side within the pin diameter and upwards the pin on the retreating side as well as on the advancing side outside the pin diameter.

5.5 Material Flow of Different Aluminum Alloys

Welds in 2024-T351, 2219-T87, 5083-O, 6061-T6, 7050-T73, 7075-T7351 were performed at the welding parameters, which are listed in Table 4-7. The welds are categorized as "cold", "nominal", and "hot" based on differences of the weld pitch. Even though the weld pitch is not a unique welding parameter[2], the terms "cold", "nominal", and "hot" shall be still used for this investigation to refer to the different welding parameters (rotational and welding speed). The material flow patterns in the AA2024 and AA2219 welds as well as in AA7050 and AA075 welds are fairly similar. Thus, only AA2024, AA7050, AA5083, and AA6061 are presented in this section. Images of the AA2219 and AA7075 welds can be found in the Appendix A.

The main differences between the alloys with respect to FSW are the different material properties. Bill Arbegast from Lockheed Martin Michoud Space Systems provided flow stress data of the alloys AA2195, AA2219, AA6061, AA7050 at elevated temperatures and varying strain rates.

The alloys of the 2XXX and 7XXX series are heat-treatable alloys with high flow stresses. The flow stress of AA6061 is lower than the one of the alloys of the 2XXX and 7XXX series. The flow stress of the above alloys is highly temperature dependent with a significant drop at elevated temperatures. The temperature dependence of the flow stress of AA5083-O is different – AA5083 is not heat treated in the O temper condition. The base material is in a minimum strength condition.

---

[2] The same weld pitch can be calculated from different sets of RPM and welding speed.

Consequently, the flow stress decrease of AA5083-O at elevated temperatures is not as big as in the heat treated alloys. The other material property to consider is the thermal conductivity; the differences in the specific heat between the aluminum alloys are negligible. The thermal conductivity of AA2024, AA2219, and AA5083 is lower than the one of AA7050 and AA7075. The thermal conductivity of AA6061-T6 is the highest of the examined alloys. In general, welding a material with a higher thermal conductivity will result in higher longitudinal tool forces and torque as well as more heat generation. In such welds heat conducts more easily from the heat source (the deforming material) to the surroundings. Therefore, the rate of heat generation is increased.

5.5.1 Material Flow in AA2024-T3

Figure 5-16 shows the vertical flow in AA2024 at the three welding conditions "cold", "nominal", and "hot" as listed in Table 4-7. The flow patterns are almost identical as those of the AA2195 welds shown in Figure 5-13 for AA2195-T8. Note that the welding parameters of the "nominal" and "hot" weld are the same as of Weld 75 and 76, respectively. The "cold" weld in AA2024 was performed at a higher welding speed than Weld 38, which was the weld with the highest weld pitch (0.61 mm/rev) in AA2195. The "cold" AA2024 weld of Figure 5-16-A shows very little mixing throughout the whole weld height. The connection of advancing and retreating side is still close to the centerline after welding throughout the total height even at the top of the weld close to the shoulder, where material is usually transported from the retreating side to the advancing side. The vertical mixing in the "nominal" and "hot" welding conditions is qualitatively the same as shown for AA2195 in Weld 75 and 76, respectively. Within the pin diameter, material is pushed downwards on the advancing side and upwards on the retreating side. Outside the pin diameter, material is pushed towards the crown of the weld on both sides. In addition, increasing the RPM (here, from "nominal" to "hot") increases the mixing of material even further. It is worth mentioning that some details may be lost due to the lower resolution[3] in the AA2024 welds.

---

[3] The resolution (in vertical direction) of the marker insert technique in the AA2195 welds was twice as high as in AA2024 because a new layer was cut every 0.5 mm instead of every 0.25 mm as in AA2195.

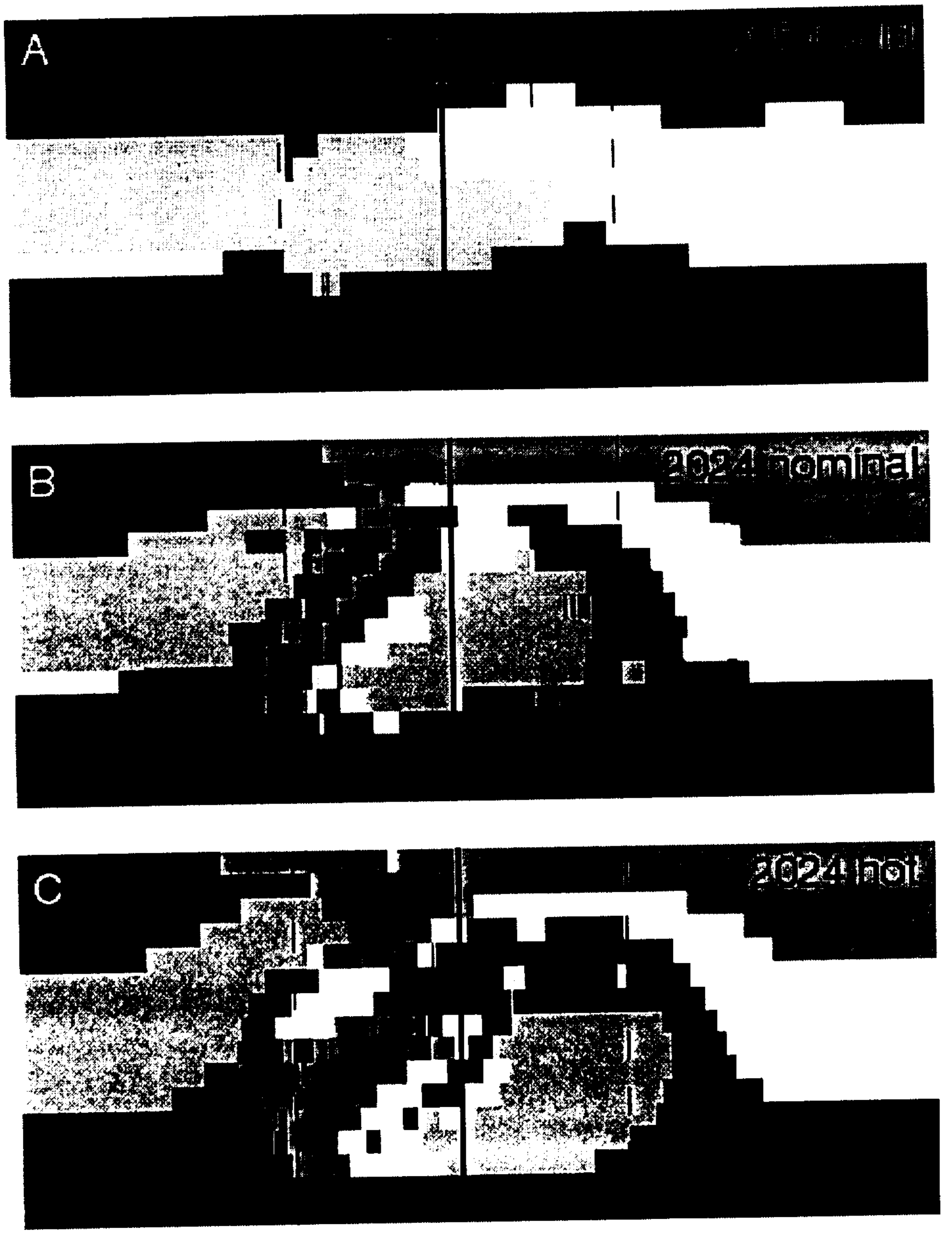

Figure 5-16 Vertical flow in three AA2024 welds. The “cold” weld (A) was performed at 232 RPM and 3.3 mm/s. The “nominal” (B) and “hot” (C) welds were both welded with 397 RPM as well as with welding speeds of 2.35 mm/s and 1.28 mm/s, respectively.

The three-dimensional shape of the deformed inserts is qualitatively the same for all three welds as shown in Figure 5-5 for AA2195. Figure 5-17 shows the 3-D plot of the "nominal" AA2024 weld projected on the y-z-plane looking in welding direction. The contour variable is the x-coordinate, which is the welding direction. The darker gray indicates backward transported material. A minimum backward transport occurs just below the region that is affected directly by the rotating shoulder. Here, the material movement due to the shoulder rotation and the extrusion of material past the pin coincide. Material, which is extruded around the pin experiences the counterclockwise rotation around the longitudinal axis on the way to its final position. It was seen in all the before mentioned welds that in the region of minimal backward transport, the marker from the middle of the retreating side is moved towards the advancing side while the markers from the bottom are pushing upwards. Maximum backward transport occurs at middle heights of the weld. The transport against the welding direction decreases towards the root of the weld.

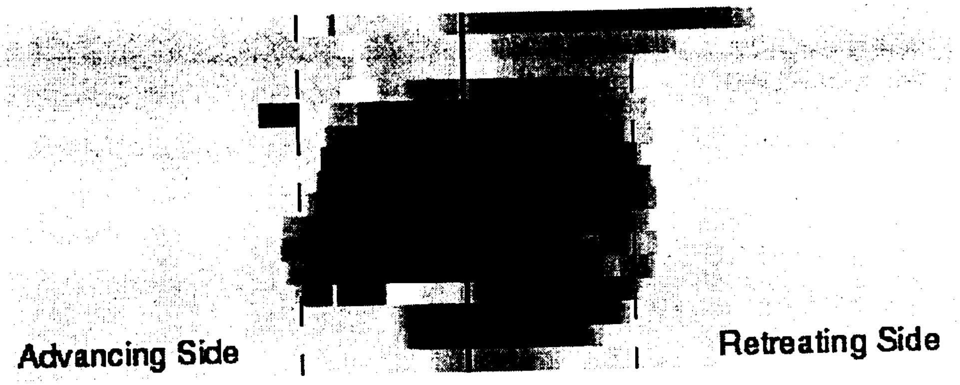

Figure 5-17 Projection of the 3-D plot of the "nominal" AA2024 weld on the y-z-plane when looking in welding direction. Dark gray indicates backward transported material.

Figure 5-18 Microstructure of the "nominal" AA2024 weld.

The microstructure of the "nominal" AA2024 weld can be seen in Figure 5-18. The dynamically recrystallized zone (DRZ or nugget) contains very fine, equiaxed grains. The "onion"-like pattern in the weld nugget is typical in FSW. However, no explanation has been found for its occurrence. The weld nugget does not extend to the top surface. The grains are larger in the region where material was transported with the rotating shoulder. The thermo-mechanically affected zone (TMZ) surrounds the nugget. The lines, described by the grains in the TMZ, point towards the crown of the weld except near the root. As shown in Figure 5-16B markers outside the pin diameter are pushed towards the top on advancing and retreating side.

The shape of the backward transported markers (Figure 5-17) agrees remarkably well with the shape of weld nugget in Figure 5-18. The "nose" in the lower part of the advancing side seen in the microstructure and in the deformed markers is very typical in FSW and can be found more or less distinctly in all welds. As already described in Section 5.1 and 5.2 material in the lower part of the advancing side is often distributed over a wide range in the horizontal plane even to positions in front of its original.

5.5.2 Material Flow in AA7050-T7

The aluminum alloy 7050-T7 was friction stir welded using the welding parameters of Table 4-7. Figure 5-19 shows the projection of the deformed markers on the y-z-plane when looking in welding direction. The vertical flow patterns are similar to those of the corresponding welds in AA2195 and AA2024. Very little mixing occurred in the "cold" AA7050 weld. Decreasing the weld pitch increases the vertical material transport. In the "nominal" and "hot" weld, material is heavily deformed within the pin diameter. Here, the marker from the middle of the advancing side is pushed towards the retreating side by the material that is pushed downwards on the advancing side. It should be mentioned that no markers were detected in parts of the lower third of the "nominal" and "hot" AA7050 welds. Here, material is "smeared" horizontally to positions even in front of its original position.

Outside the pin diameter not as much material is pushed upwards in the "nominal" and "hot" weld shown in Figure 5-19 B and C, respectively, as in the AA2024 and AA2195 welds. A look at the material properties may clarify the phenomena. The flow stress and the thermal conductivity of AA7050 are higher than the ones of AA2024. Assuming that the deformation of the AA7050 during the extrusion around the tool generates comparatively or more heat than AA2024, one would expect the deformed zone to be similar or larger than in the AA2024 welds. However, the opposite is the case. The generated heat is conducted faster than in AA2024. As a consequence, material adjacent to the zone of heaviest deformation (and most deformational heating) is cooling quicker than in AA2024. Hence, the material is not as vulnerable to deformation. In conclusion, the region of heavy material deformation (similar to the one in the corresponding AA2024 welds) is surrounded by material, which experiences less deformation than AA2024.

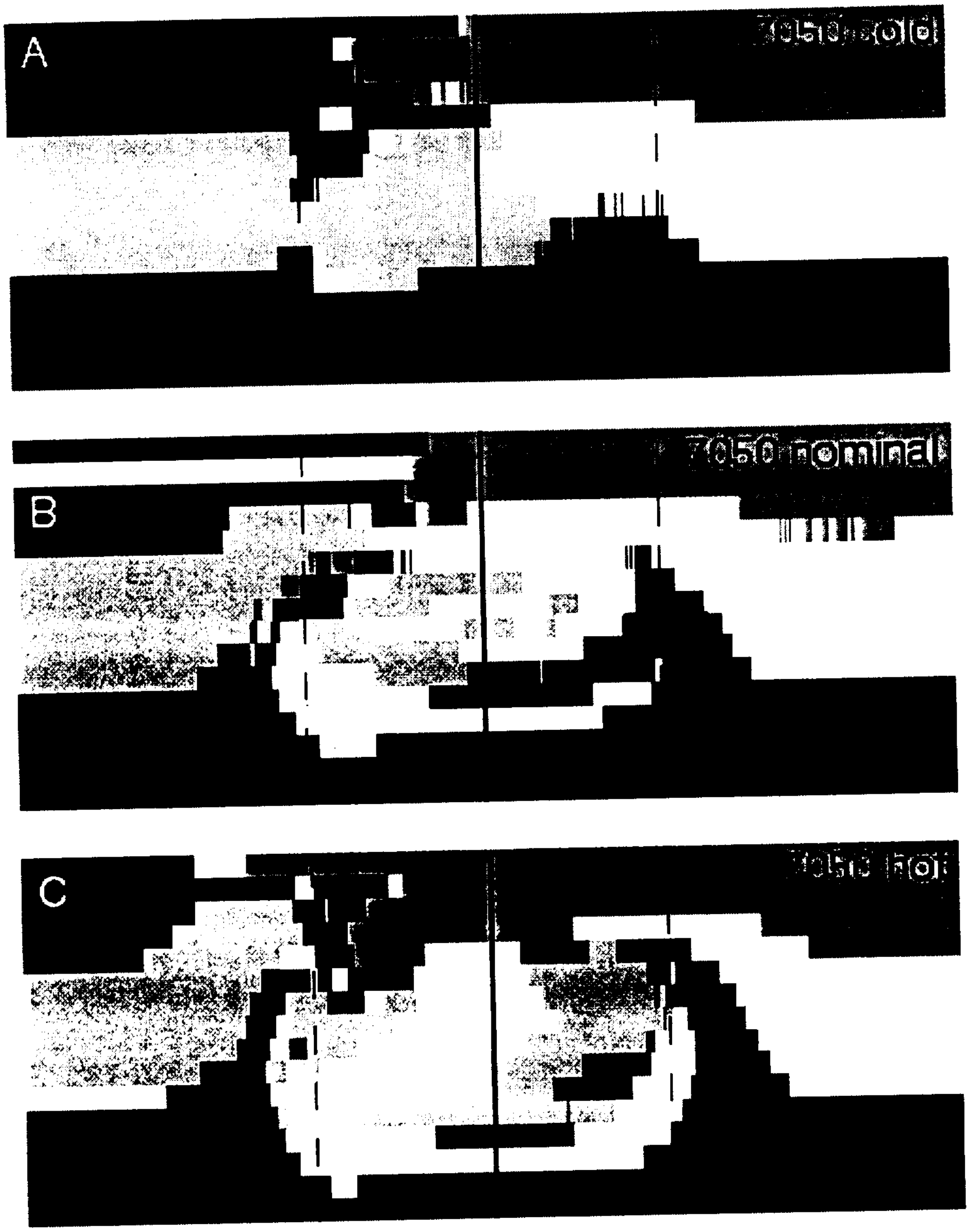

Figure 5-19 Vertical flow in the three AA7050 welds.

5.5.3 Material Flow in AA5083-O

The "cold" AA5083 weld was not analyzed using the marker insert technique. Figure 5-20 shows the vertical flow for the "nominal" (A) and "hot" (B) welding conditions listed partially in Table 4-7. The "hot" weld was performed at 637 RPM. 29

layers were cut in the AA5083 "hot" weld. Therefore, the resolution is higher than in the "nominal" weld. The material flow in the AA5083 welds is different from the previously shown alloys of the 2XXX and 7XXX series. The volume of deformed material is larger. Material is deformed more than 10 mm off the centerline on the retreating side in both welds. The FSW typical vertical flow pattern exists only in parts in the AA5083 welds. In the "nominal" weld, almost no material was pushed towards the top on the advancing side. Also in the "nominal" weld, the markers placed at the bottom of the weld truly mixed into the base material (not seen in Figure 5-20). In the "hot" weld, the transport towards the crown of the weld on the advancing and the retreating side is similar as already shown for the other aluminum alloys.

However, the material of the marker from the top of the advancing side (TA) marker is different. During the extrusion around the pin this marker is pushed towards the root of the weld. A substantial amount of material is deposited very close to the bottom. Not all of the TA marker can be seen in Figure 5-20 because it is hidden behind other markers. In addition, TA marker material is part of the material that is pushed towards the top outside the pin diameter. This phenomenon did not occur in any other alloy at any (investigated) welding condition.

Figure 5-20 Vertical flow in AA5083-O.

Figure 5-21 shows images of the seventh marker, which covered the total height and width of the weld, at three different heights in the "nominal" and "hot" welding condition, respectively. The distribution of material in the longitudinal planes can be best seen applying the marker insert technique to this marker; the 6 single markers provide information about the vertical flow. In Figure 5-21, the welding direction is from the top of the page to the bottom. The tool rotation was clockwise. Material is spread out in welding direction at the middle of the "nominal" weld (B) and at all shown levels of the "hot" weld (D, E, and F). It is worth mentioning that weld defects in the form of voids occurred in both welds. The defects are clearly visible in the middle of the “hot” weld as shown in Figure 5-21 E, whereas defects in the “nominal” weld were seen only sparsely.

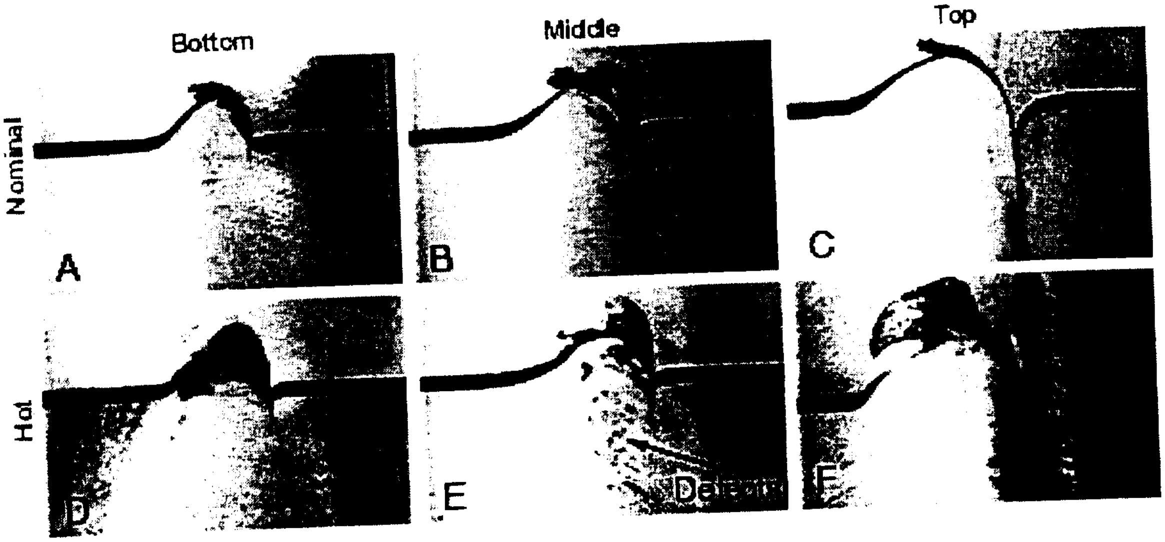

Figure 5-21 AA5083 hot and nominal welds at the bottom, middle and top, respectively. The images show the marker that covered the total height and width of the welded zone. The welding direction points from the top to the bottom of the page.

The clearly different flow behavior of friction stir welded AA5083-O may have several reasons. As already mentioned AA5083-O is the only aluminum alloy used in this research project that was not heat-treated. Therefore, the flow stress is less temperature dependent than that of the other alloys.

Additionally, defects were seen for the "nominal" and "hot" welding conditions. Failure locations of transversely loaded tensile specimen were in the nugget in the "hot" weld [51]. Specimen of the "nominal" weld failed in the heat-affected zone and in the nugget. Additionally, the joint efficiency was lowest in the "hot" weld. The occurrence of weld defects suggests that "colder" welding conditions are preferred than those used in AA5083-O.

5.5.4 Material Flow in AA6061-T6

AA6061-T6 was friction stir welded using the welding parameters of Table 4-7. The "hot" weld was performed at 832 RPM. Figure 5-22 shows the vertical flow in the "cold" (A), "nominal" (B), and "hot" (C) weld. Note that no marker positions (indicated by the white areas in the figures) could be extracted from the images in upper parts of the "cold" and "hot" weld due to the insufficiently etched surface. The missing data in the lower part of the "nominal" weld is a result of the high degree of mixing of marker and base material.

The typical FSW flow pattern appears in all three welds. Material that is extruded around the retreating side is pushed up on the retreating side before it is pushed down within the pin diameter on the advancing side. Material from the advancing side not participating in the "retreating side extrusion" passes the pin (outside the pin diameter) on the advancing side. In general, material on the advancing side outside the extrusion zone is moved upwards in welding direction. The vertical flow in the "cold" and "nominal" AA6061 welds is similar to the vertical flow of the corresponding welds in the 2XXX and 7XXX series. Only little vertical flow occurred in the "cold" weld since almost no material from the top of the weld was pushed downwards. The size of the deformed zone is much larger in the upper half of the "cold" and "nominal" weld than in the corresponding welds of the 2XXX and 7XXX series. The width of the deformed zone on the retreating side increases with increasing weld energy in all three welds. In addition, the deformed zone on the advancing side is smaller in the "hot" weld than in the "nominal" weld.

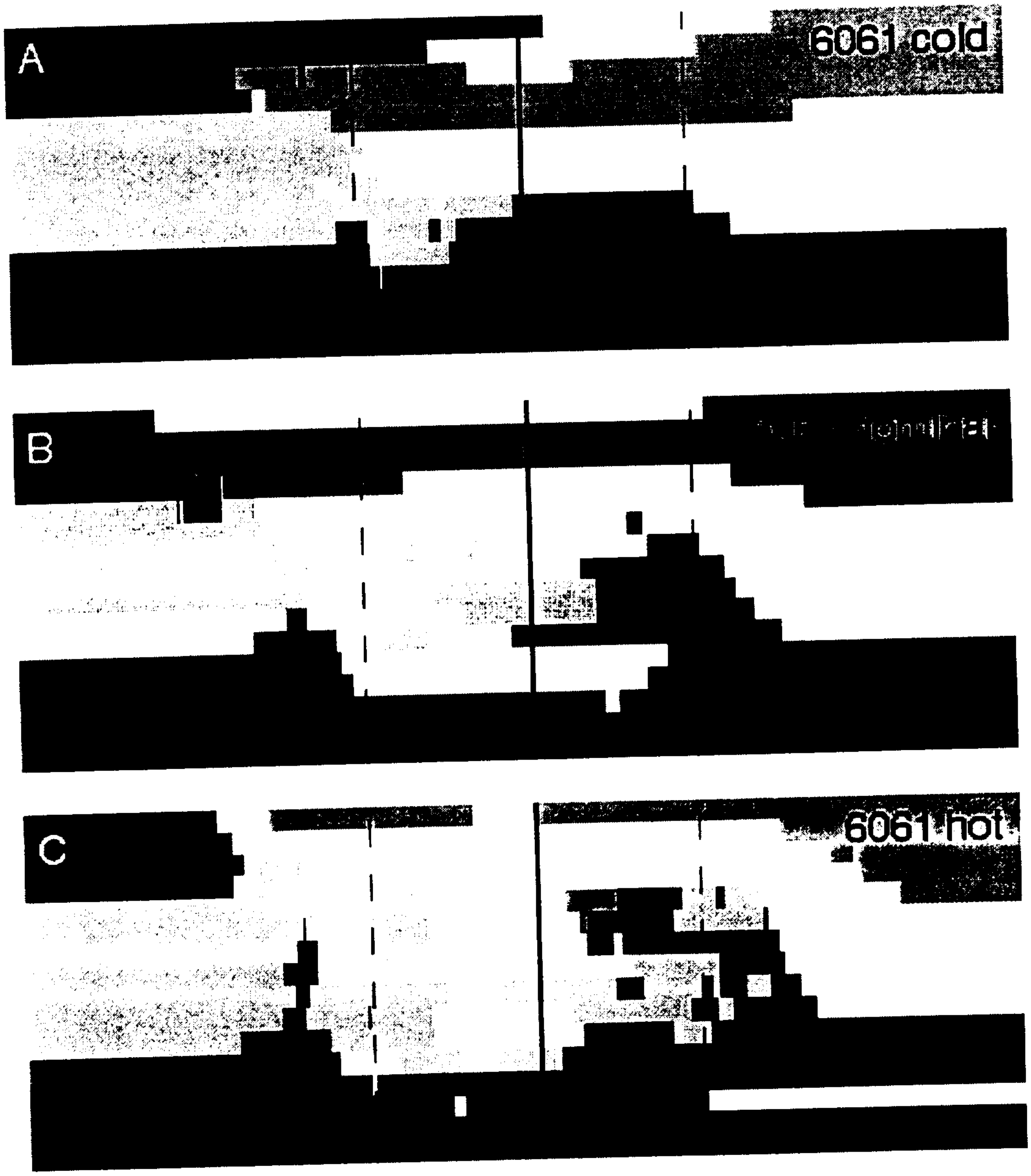

Figure 5-22 Vertical flow in AA6061-T6.

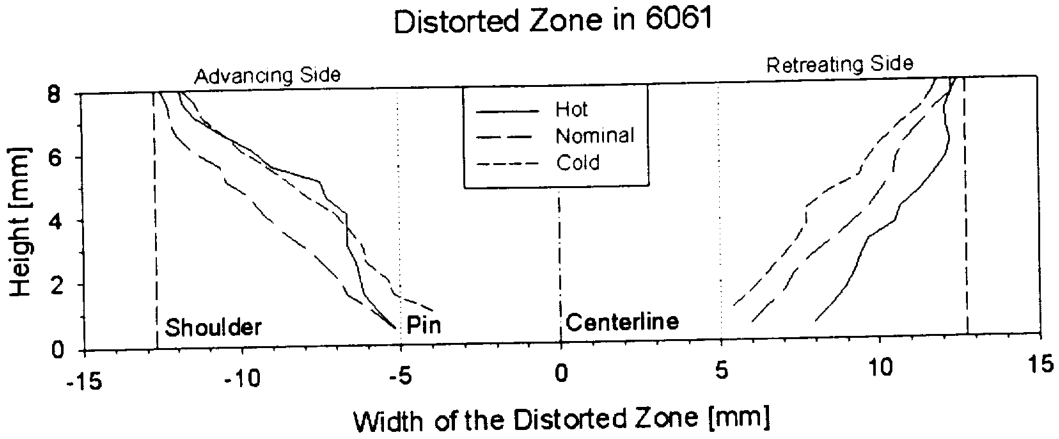

Figure 5-23 Width of the deformed weld zone in the three AA6061 welds. Note that abscissa and ordinate are true to scale.

The size of the distorted zone was determined from the images of the markers covering the total height of the weld. In every image, the distance in the transverse direction from the centerline to the transition between deformed and undeformed marker was measured on both advancing and retreating side. The distances in the images (in pixel) were then converted to real distances using the spacial calibrations. The same procedure was used to determine the maximum backward transport at each layer in each weld.

The influence of the weld pitch on the size of the deformed zone can be seen in Figure 5-23. On the retreating side, the width increases from the "cold" over the "nominal" to the "hot" weld. The width of the deformed zone on the retreating side increases almost linearly from the bottom to the top in all three welds. At top of the weld the width equals almost one shoulder diameter, in all three welds. On the advancing side, the width of the deformed zone also increases linearly from the bottom to the top of the weld in the "cold" and "nominal" weld, where the larger volume of material is deformed at the higher weld pitch. However, the shape of the deformed region in the "hot" weld is different on the advancing side. The width of the deformed zone is as small as in the "cold" weld in the upper third of the weld but larger in the lower two-thirds. However, it never exceeds the size of the deformed zone in the "nominal" weld.

A look at the maximum transport against the welding direction illustrates the different shape of the deformed zone in the "hot" weld. Figure 5-24 shows the maximum backward transport of the AA6061 "nominal" and "hot" weld. The "cold" weld is not shown in this figure because the shape is qualitatively the same as for the "nominal" weld. The shape of the deformed marker of the hot weld is qualitatively the same as shown in Figure 5-9 and Figure 5-12 for AA2195. Hence, the deformed zones in both, the "cold" and the "nominal" AA6061 weld deviate from the common shape.

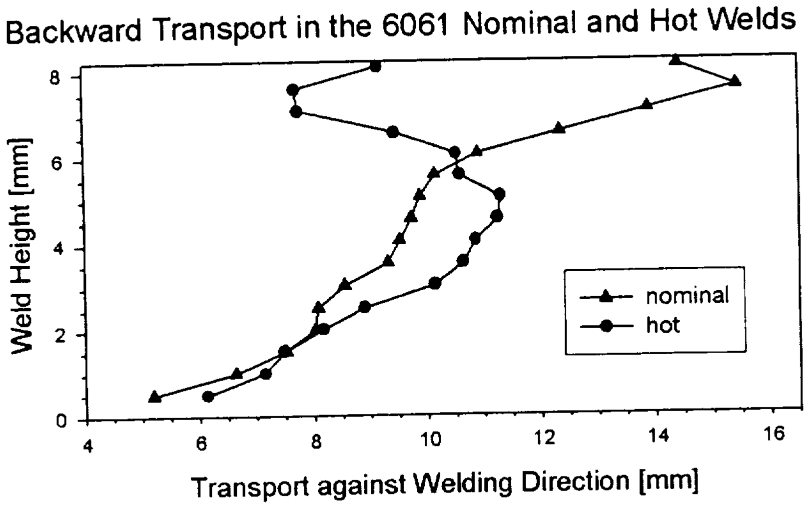

Figure 5-24 Comparison of the backward transport in the AA6061 "nominal" and "hot" welds.

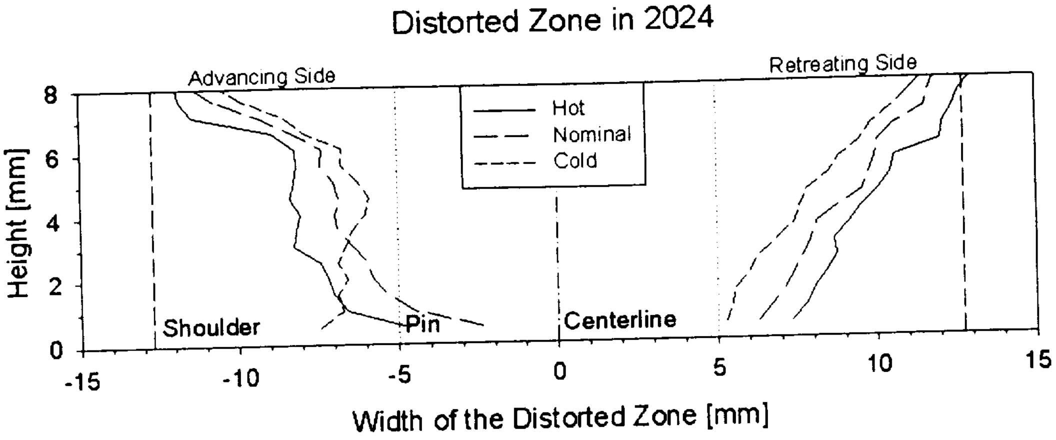

Figure 5-25 Width of the distorted zone in the AA2024 welds from Section 5.5.1. The deformed zone on the retreating side is similar to the AA6061 welds. However, only the welded zone in the "hot" AA6061 weld has a similar shape as the AA2024 welds.

The width of the deformed zone of AA2024 is shown in Figure 5-25 to clarify the difference in the AA6061 welds. On the retreating side of the three AA2024 welds (Table 4-7 and Section 5.5.1), the pattern of the deformed zone is the same as in the AA6061 welds. The zone increases linearly from the bottom to the top of the weld. Decreasing weld pitch increases the width of the zone on both sides of the centerline. However, on the advancing side the increase of the width of the zone is different in the upper third than in the lower two-thirds of the weld similar to the change in the "hot" AA6061 weld. The "cold" AA2024 may be an exception because the width of the deformed zone is not changing in the lower half of the weld. Note that the width of the deformed zone in the AA2024 welds is representative for the welds of the 2XXX and 7XXX series.

After having made these observations, two obvious questions arise: Why is the shape of the deformed markers in AA6061 different than in welds of the 2XXX and 7XXX series? Moreover: Why is the shape in the "hot" weld different from that in the "cold and nominal" weld?

A look at the material properties of AA6061-T6 may answer the questions. The flow stress of AA6061 is lower than the flow stress of the 2XXX and 7XXX alloys. Moreover, the thermal conductivity of AA6061 is the highest of all investigated alloys. In an alloy with the lower resistance to plastic deformation less heat will be generated during the deformation. On the other hand, more material may be vulnerable to plastic deformation because of the lower flow stress. In an alloy with the higher thermal conductivity heat is transferred faster from the heat source (the deforming material) to the surroundings. The combination of both material properties makes the AA6061 friction stir welds special. It may be that in the "hot" weld with the very low weld pitch of 0.092 mm/rev "enough" heat is generated to overcome the high thermal conductivity of the material. Both of these factors may reduce the gradients in temperature and flow stress. Therefore, deformation may occur in a larger volume.

In the following, the influence of the marker inserts on the material flow will be investigated. A well-defined interface between material originally on opposite sides of the weld centerline is present in the "cold" AA6061 weld. It cannot be seen in the welds that were performed at lower weld pitch. The different etching characteristics of the thin oxide layer on the aluminum plates makes the interface of advancing and retreating side material visible in the digital images of the marker insert technique. Figure 5-26 shows the images taken at the seven marker locations near the top surface of the "cold" AA6061 weld. The images are assembled in the same sequence as the seven markers were placed in the weld. In Figure 5-26 the welding direction was from the top to the bottom of the page. The interface of both plates can be seen as a white line at the center of each image progressing from one image to the other. With the presence of the AA7075 markers the white line slightly deviates from the vertical line. The influence of the markers occurs after the tool has passed the marker ensuring the reliability of the marker insert technique. However, using the marker insert technique, small uncertainties have to be accepted. It is worth mentioning that the interface of the two plates changes throughout the weld height as seen in the projection of the vertical on the y-z-plane (Figure 5-22 A).

Figure 5-26 Images are taken close to the top of the "cold" AA6061 weld at the seven original marker locations. The white line in the middle of each image is the connection of the plates from advancing and retreating side.

5.6 FSW Flow Visualization Summary and Conclusions

Friction stir butt welds were analyzed with respect to the material flow for different welding parameters. The material transport was visualized using marker inserts in the faying surface of the two plates to be welded. The marker insert technique gives insight in the TMZ by the reconstruction of the piecewise cut-off welded zone. As a result, full three-dimensional plots of the deformed markers provide a good, qualitative characterization of the material flow in these friction stir welds. However, this technique does not reconstruct the actual flow path of the material.

The tool rotation produces deformation heating in the workpiece leading to a reduction in the flow stress of the base material, allowing the material in the weld zone to flow. Increasing the heat input by the tool results in reduced flow stresses and increases, as a side effect, the mobility of material in the weld. The material transport in FSW is a result of the two tool motions – translation and rotation. The bulk of material is moved around the pin to final positions behind its original position. The marker insert technique does not reconstruct the actual flow of material past the tool. Knowing only the shape of the deformed markers, the material flow seems possible around either side or just around one side of the tool. However, it is well accepted that all the material within the pin diameter (or the extrusion zone) is passing the tool on the retreating side. During the extrusion material is first pushed upwards on the retreating side and then pushed downwards on the advancing side. Material outside the extrusion zone on the advancing side is generally pushed in welding direction towards to top of the weld. The material transport due to the broad shoulder has a strong influence on the vertical mixing in the weld. The more material is moved from the retreating side to the advancing side, the more material is pushed down within the pin diameter on the advancing side, resulting in a secondary, vertical, counterclockwise, circular motion around the longitudinal axis of the weld. Outside the pin diameter, material is pushed towards the crown of the weld. The maximum material transport against the welding direction was not larger than one pin diameter.

The amount of material involved in the vertical mixing depends strongly on the welding conditions such as the rotational and the translational speed of the tool. A friction stir weld performed at low rotational and medium translational speed shows almost no vertical mixing at middle to low heights in the weld. Therefore, the process is nearly two-dimensional in a sufficient distance from the tool shoulder. The mixing in FSW increases with increasing weld energy.

The material flow patterns in aluminum alloys of the 2XXX and 7XXX series are fairly similar. The existing differences may be explained with the different material properties such as flow stress and thermal conductivity.

The material transport in AA6061 clearly deviates from the common flow pattern. The width of the deformed zone is much larger in the "cold" and "nominal" weld than in the "hot" weld. The maximum backward transport in those two welds occurs close to the top of the weld, which is usually a region of minimum backward transport. Additionally, the deformed zone increases linearly in transverse direction with increasing weld height on advancing and retreating side in those two welds. The shape of the deformed zone in the "hot" AA6061 weld is qualitatively the same as in welds of the 2XXX and 7XXX series. The AA6061 flow characteristics may be explained with the high thermal conductivity of the material.

The material flow in AA5083-O is most different from all the other aluminum alloys. It is believed that the different temperature dependence of this alloy's flow stress causes the widely spread material in the longitudinal planes. Additionally, the width of the deformed zone is fairly large in AA5083.

Influences of the tool-to-workpiece-normal angle, the thread size, and many more FSW related parameters on the flow field were not investigated. Furthermore, the resolution of the flow visualization is limited by the size of the markers. However, the marker insert technique was the first method that provided three-dimensional plots of the welded zone visualizing a detailed flow pattern.

6 Physics of the FSW Process Model

In this research, FSW was modeled using the Eulerian flow formulation. The commercial software FLUENT was used to simulate the process. Assuming that the elastic behavior of the aluminum alloy can be neglected due to the expected high strains, the analogy between pure plastic deformation and fluid flow was used. The material flow was simulated using fluid mechanics, hence, a viscosity function for the alloy was formulated.

The development of the FSW process model was divided into three phases.

I. FSW as a two-dimensional process
II. Validation and Testing of the 2-D model
III. Expansion of the 2-D model to 3-D.

In Phase I of the process model development FSW was interpreted as a two-dimensional process. A circular cylinder represents the tool, i.e. the pin, in the 2-D simulation. The material flow was modeled as a two-dimensional, steady state, laminar flow of an incompressible non-Newtonian fluid past a rotating, non-threaded cylinder. Due to the steady state condition, no moving mesh model is required. The goal of Phase I of the model development was the investigation of the influence of boundary conditions, fluid properties, and different flow parameters as well as the determination of the best-suited solver algorithms. Even though FSW is a three-dimensional process, a 2-D model was developed because it uses less CPU time than a 3-D model and the Phase I results are easier to understand in 2-D.

As shown in Chapter 5, the vertical mixing in FSW is minimal at so-called "cold" welding conditions. In those welds (performed with a medium translational and a low rotational speed), the tool shoulder affects only the upper part of the weld height. Once the influence of the tool shoulder is diminished material is transported almost only in the longitudinal plane. The 2-D model simulates the material flow at middle and lower heights of such "cold" welds.

Laminar fluid flow condition was assumed during the flow past the rotating cylinder. From the expected small Reynolds numbers ($Re = UD\rho/\eta$), where U denotes the maximum velocity, D the pin diameter, ρ the density and η the dynamic viscosity, one can conclude that the flow is rather laminar than turbulent. Since the viscosity at elevated temperatures and high strain rates is still very high (10^3 Pas and larger), very small Re-numbers (approx. 10^{-5}) were expected close to the pin. The flow visualization with the marker inserts, even though it shows only the final position in the weld, supports the laminar flow condition. No signs of a random or chaotic flow pattern were observed in the experiments.

In Phase I of the FSW process model steady state conditions were assumed. The investigation of the transient plunging of the tool, the beginning of the forward motion of the tool and the end of the weld were not of interest in Phase I. Considering a rotating cylinder without forward motion but with material that is passing the cylinder, the process becomes steady-state. For the fluid mechanics based modeling approach, the steady state conditions means that no deforming or moving mesh models are necessary. The discretized flow domain does not change during the solution of the governing equations.

The material flow past a cylinder is a well-studied problem. The occurrence of Karman vortex streets at Reynolds numbers higher than 35 in the flow past a cylinder was first reported by Karman [70] in 1921 and can be found in many textbooks nowadays ([71] – [73]). However, many aspects of the flow past a circular cylinder can be studied. Badr and Dennis [74] investigated the transient flow past a suddenly started rotating and translating cylinder for two Reynolds numbers (200 and 500) and compared the numerically predicted vortices with experimental observations. Dhahir and Walters [75] analyzed the behavior of non-Newtonian fluids in the flow past a freely rotating cylinder at small Reynolds numbers. Juarez et al. [76] modeled directly the flow past a freely rotating cylinder using an explicit algorithm to simulate the cylinder-fluid interaction and a high-order Lagrangian FEM formulation to solve the Navier-Stokes equation. They found that the direction of the cylinder rotation depends on the Reynolds number and the distance to the surrounding wall. The material flow past a cylinder becomes fairly complicated at medium Reynolds numbers, even in laminar flow conditions. The friction stir welding related properties that influence the Reynolds number like the fluid density, the viscosity, welding and rotational velocity as well as the pin diameter suggest that the Reynolds number is well below 1. No formation of Karman vortices is expected and therefore, the simulation of FSW as a flow past a rotating cylinder does not lead to false results as far as vortex shedding is concerned.

In Phase II of the model development, the influence of the different boundary conditions is tested. Therefore, the welding parameters such as the rotational and the welding speed as well as the other boundary conditions are varied. Strictly speaking, the 2-D model is only valid for "cold" welding conditions to simulate FSW. However, the welding parameters are varied over a broad range in Phase II. Some key experiments are used to validate the prediction behavior of the 2-D model.

The 2-D model is expanded to three dimensions in Phase III. Different possible tool geometries are presented. Depending on the tool details such as tool-to-workpiece angle and threads on the pin, different solution methods are suggested. In its simplest form, the non-tilted tool consists of a flat shoulder and a non-threaded pin. The significance of the thermal boundary conditions will be discussed, i.e. at the interface of workpiece and backing plate. Data such as torque and forces recorded during welding are used to validate the models.

6.1 Material Properties

6.1.1 The Non-Newtonian Flow Properties

The application of a fluid mechanics based model requires a viscosity function to simulate the material flow behavior of the aluminum alloy. The FSW process was modeled using different material constitutive equations. First, a constant, high Newtonian viscosity was assumed. Next, a temperature dependent viscosity, estimated from the temperature dependence of Young's modulus, was implemented. None of the simulations was able to capture a friction stir welding like flow pattern. It was, therefore, obvious that only a temperature and deformation rate (strain rate) dependent viscosity would sufficiently describe the "true" rheological properties of the alloy at elevated temperatures and high rate of deformations.

If the elastic deformation of the alloy is neglected (especially true for large deformations) the strain rates in terms of viscoplasticity from equation (1-1) are given as (Zienkiewicz and Godbole [7] and Zienkiewicz et al [8]) using the indicial notation:

$$\dot{\varepsilon} = \Gamma_{\mathrm{ijkl}}\, \sigma_{kl} \tag{6-1}$$

where

$$\Gamma_{ijkl} = \Gamma(T, \varepsilon_{\mathrm{kl}})$$

is a symmetric tensor, T the temperature, and ε_{kl} are the strains. For a Von Mises type of plastic or visco-plastic material the tensor, Γ can be obtained using Perzyna's viscoplasticity model (Zienkiewicz and Cormeau [9]) and, hence, equation (6-1) can be written as:

$$\dot{\varepsilon}_{ij} = \frac{1}{2\eta} s_{ij} \quad \text{with} \quad s_{ij} = \sigma_{ij} - \delta_{ij} p \quad \text{and} \quad p = \frac{\sigma_{ii}}{3} \tag{6-2}$$

with the viscosity η

$$\eta = \frac{\sigma_y + \left(\bar{\dot{\varepsilon}} / \gamma\sqrt{3}\right)^{1/n}}{\sqrt{3}\,\bar{\dot{\varepsilon}}} \,. \tag{6-3}$$

In equation (6-2) and (6-3), p is the pressure, σ_{ij} and s_{ij} are the components of the stress and the deviatoric stress tensor, respectively, γ and n are physical constants for the viscoplastic model, and σ_y is the uniaxial yield stress. The effective strain rate is defined as

$$\bar{\dot{\varepsilon}} = \sqrt{\tfrac{2}{3}\dot{\varepsilon}_{ij}\dot{\varepsilon}_{ij}} \tag{6-4}$$

with the rate of deformation tensor $\dot{\varepsilon}_{ij}$ calculated from the velocity gradients $\partial u_i / \partial x_j$, where u_i and x_j denote velocity and coordinate vectors, respectively.

$$\dot{\varepsilon}_{ij} = \frac{1}{2}\left(\frac{\partial u_i}{\partial x_j} + \frac{\partial u_j}{\partial x_i}\right). \tag{6-5}$$

For ideal plastic flow, γ tends to infinity and equation (6-3) yields

$$\eta = \frac{\sigma_y}{3\,\bar{\dot{\varepsilon}}} \,. \tag{6-6}$$

Replacing in equation (6-6) the uniaxial yield stress with the effective deviatoric flow stress $\sigma(T, \bar{\dot{\varepsilon}})$ one obtains a generalized form of the viscosity.

$$\eta = \frac{\sigma(T, \bar{\dot{\varepsilon}})}{3\,\bar{\dot{\varepsilon}}} \tag{6-7}$$

Note the temperature and strain rate dependency of the effective deviatoric stress in equation (6-7), which describes a temperature dependent non-Newtonian viscosity. Furthermore, it is important to notice that the viscosity tends to infinity for small strain rate values; therefore, a numerical cut-off value must be chosen in the numerical computation.

Another form of the viscosity describing the plastic deformation of metals is the Bingham plastic, which describes materials that do not flow if the shear stress is below a certain yield value τ_f (Eirich [71] and White [73]). Bingham plastic models are also used in the simulation of semi-solid thixo-forming processes of aluminum alloys (Sigworth [78]). Jaluria [79] discussed the numerical simulation of the coupled heat transfer and fluid flow in some material processing technologies and pointed out the importance of the right choice of the viscosity model. Jaluria suggested the use of a power-law model, which included temperature dependence for several materials.

The determination of an "exact" constitutive behavior of the aluminum alloy is important for the accurate simulation of a process. High temperature and high strain rate properties of numerous materials have been published in the past. Malas and Seetharaman [80] proposed a dynamic material model for γ-Ti-Al alloy and showed a processing map on a strain rate temperature map. Mukai et al. [81] investigated the strain rate sensitivity of fine-grained IN905XL aluminum alloys. They observed at strain rates lower than 10 s^{-1} negative strain rate sensitivity and at high strain rates positive strain rate sensitivity. Oosterkamp et al. [82] measured the flow stress and strain rate sensitivity of the two aluminum alloys AA6082 and AA7108 at three temperatures over a strain rate range from 0.1 to 3000 s^{-1}. The strain rate sensitivity of both precipitation hardenable alloys was very low; at strain rates higher than 2000 s^{-1} a trend of even negative strain rate sensitivity was seen. Altan and Boulger [83] summarized temperature and strain rate dependent flow stress data of numerous metals including some aluminum alloys, steels, copper alloys, and titanium alloys.

Zener and Hollomon [84] reported in 1944 on the effect of strain rate on the plastic flow of steel. They proposed equivalence "of the effects of changes in strain rate and in temperature upon the stress-strain relation in metals". Zener and Hollomon correlated stress data at different temperatures and strain rates using the now-called Zener-Hollomon parameter Z, which represents the temperature compensated strain rate.

$$\sigma = f\left(\bar{\dot{\varepsilon}} \exp\left(\frac{Q}{RT}\right)\right) = f(Z) \tag{6-8}$$

In equation (6-8) $\bar{\dot{\varepsilon}}$ is the effective strain rate, R is the universal Gas constant, Q is the activation energy, and T the absolute temperature. Sellars and Tegart [85] and Sheppard and Wright [86] subsequently modified the constitutive flow stress relationship yielding.

$$\sigma(T,\bar{\dot{\varepsilon}}) = \frac{1}{\alpha}\ \ln\left\{\left(\frac{Z(T,\bar{\dot{\varepsilon}})}{A}\right)^{1/n} + \left[\left(\frac{Z(T,\bar{\dot{\varepsilon}})}{A}\right)^{2/n} + 1\right]^{1/2}\right\} \tag{6-9}$$

Equation (6-9) describes the effective deviatoric flow stress of aluminum alloys and other metals as a function of temperature and strain rate using the constant fitting parameters A, α, and n. A more common form of equation (6-9) uses the hyperbolic sine, sinh:

$$Z(T,\bar{\dot{\varepsilon}}) = \bar{\dot{\varepsilon}}\ \exp\left(\frac{Q}{RT}\right) \ = \ A[\sinh(\alpha\sigma)]^n \tag{6-10}$$

The constitutive relationships from equations (6-9) and (6-10) have been widely used in hot working processes. Sheppard [87], Zhou and Clode [88], Clode and Sheppard [89], and Sheppard and Jackson [90] applied a modified Zener-Hollomon equation to the extrusion process. Sheppard and Jackson published the constants of the constitutive law (6-9) for aluminum alloys from the 1XXX to the 7XXX series.

Shimansky and McQueen [91] found good correlation between experimental torsion data and the constitutive law for AA8009. McQueen and Lee [92] determined the necessary constants for the high strength aluminum alloy 6060. Wang et al. [93] applied the constitutive law to TiAl alloys and concluded from the derived values of the activation energy Q that the plastic deformation was atomic diffusion controlled.

Aukrust and LaZghab [94] reported experimentally and analytically on thin shear boundary layers in the flow of AA6082 in a channel with parallel walls. They calculated the velocity profile from the equation of motion in flow direction and the viscosity based on equations (6-7) and (6-9). An exponential velocity was predicted at high strain rates suggesting the existence of a shear boundary layer, which agreed very well with changes in the grain structure of the alloy. Aukrust and LaZghab concluded their paper with a recommendation for numerical modeling of hot forming processes using very fine meshes in regions of expected high strain rates in order to capture the high velocity gradients.

It should be mentioned that a number of more sophisticated material constitutive laws are proposed including the accumulated strain and internal variables accounting for microstructural changes (e.g. [95], [96] and [97]). Due to the availability of the material constants and its relative simplicity, the constitutive law from equation (6-9) was used in the present research. Strain hardening is neglected. Combining equations (6-7) and (6-9), one obtains the final form of the viscosity used to simulate FSW.

$$\eta(T,\dot{\bar{\varepsilon}}) = \frac{1}{3\,\dot{\bar{\varepsilon}}\,\alpha}\,\ln\left\{\left(\frac{Z(T,\dot{\bar{\varepsilon}})}{A}\right)^{1/n} + \left[\left(\frac{Z(T,\dot{\bar{\varepsilon}})}{A}\right)^{2/n} + 1\right]^{1/2}\right\} \qquad (6\text{-}11)$$

As mentioned above, a cut-off value for the viscosity had to be chosen to avoid infinite values at low strain rates. The maximum viscosity was set at 10^{12} Pas, which was approximated from low strain rate and moderate temperature values. In the present model, regions of low strain rates correspond to the undeformed material in

FSW. Therefore, no mistake is made, if a constant high viscosity is used in regions where the material is not deforming.

Alloy	**α [MPa]**	**n**	**Q [kJ/mol]**	**ln A [s^{-1}]**	**R [J/mol-K]**
6061	22.22	3.55	145.0	18.3	8.314
2024	62.5	4.27	148.88	19.6	8.314

Table 6-1 Material constants of AA6061 and AA2024 for the viscosity in equation (6-11). The constants are published in [90].

The two different alloys shown in Table 6-1 have been used in the present research. The constants of AA2024 and AA6061 were taken from Sheppard and Jackson [90]. Figure 6-1 shows equation (6-9) over a broad temperature and strain rate range using the values for AA6061 from Table 6-1.

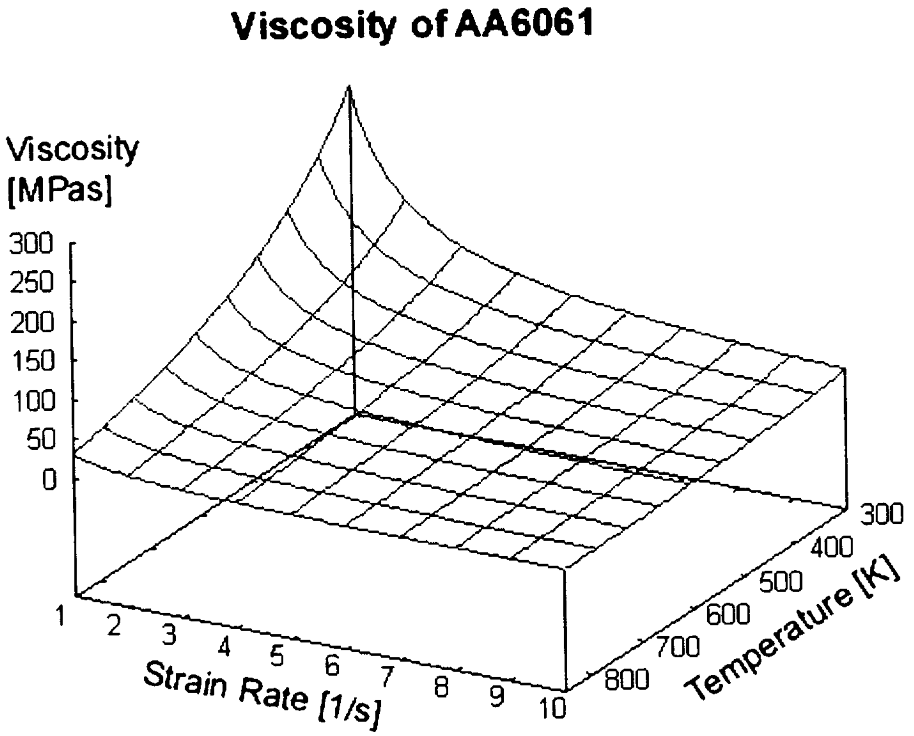

Figure 6-1 The viscosity (equation (6-9)) of AA6061 of a function of temperature and strain rate using the constants of Table 6-1.

As mentioned above, heat is generated due to viscous dissipation in the fluid. The viscosity of the alloys drops dramatically several orders of magnitude once the solidus temperature is reached and first particles become liquid. If the material is less resistant to deformation, less deformation heat will be generated. Therefore, it is obvious that heat generation in a real material is self-limited. The viscosity above the solidus temperature T_s was defined in the following way. Within the first 50 °C above T_s, the viscosity drops 3 orders of magnitude maintaining the strain rate dependence. Thereafter, the viscosity is strain rate dependent only. The viscosity of semi-solid aluminum alloys is of the order of several Pas, which is approximately 3 orders of magnitude lower than the viscosity of hot worked aluminum alloys. The temperature range in which the viscosity drop occurs was chosen arbitrarily because no published flow stress or viscosity data in that temperature region is available. The viscosity drop might be an area to adjust the material properties in the model to those more closely to a real material such as AA6061.

6.1.2 Thermal Conductivity and Specific Heat

Both, the thermal conductivity k and the specific heat c_p are temperature dependent functions. Linear fits have been used to approximate the behavior over the expected temperature range.

Alloy	**T_s [°C]**	**k [W/m-K]**	**c_p [J/kg-K]**
6061	582	115.23 + 0.1594 T	789.90 + 0.4959 T
2024	502	87.243 + 0.1168 T	718.29 + 0.4754 T
2195	560	0.27718 T	634.59 + 0.8562 T

Table 6-2 Solidus temperature, thermal conductivity, and specific heat of AA6061 and AA2024. Note that the absolute temperature is used in the linear equations.

Table 6-2 lists the thermal conductivity and specific heat of AA6061 and AA2024 using the absolute temperature. The 2D model, which is described below, was used to perform parametric studies with respect to the material properties. Therefore, the offset of the linear function of k and c_p was varied holding the slopes constant. The exact numbers are listed in Section 7.4.6. A constant density of 2700 kg/m^3 is assumed in all cases.

6.2 Governing Equations

The basic equations solved by the computational fluid dynamics (CFD) code FLUENT are the three laws of conservation for physical systems

- Conservation of mass (continuity)
- Conservation of momentum (Navier-Stokes equation)
- Conservation of energy (first law of thermodynamics)

Using the indicial notation, the conservation of mass in Eulerian terms can be expressed its most general form as

$$\frac{\partial \rho}{\partial t} + \frac{\partial}{\partial x_i}(\rho u_i) = 0 . \qquad (6\text{-}12)$$

In equations (6-12), x_i and u_i denote coordinate and velocity vectors. If the density ρ is constant as it is in incompressible flows, the continuity equation (6-12) reduces to

$$\frac{\partial u_i}{\partial x_i} = 0 . \qquad (6\text{-}13)$$

The conservation of momentum is derived from Newton's second law, which expresses the balance of applied forces and the resulting acceleration of a particle with a finite mass. In the case of steady state fluid flow neglecting gravitational and external body forces, the conservation of momentum yield the following form of the Navier-Stokes equations:

$$\frac{\partial}{\partial x_j}(\rho\, u_i u_j) = -\frac{\partial p}{\partial x_i} + \frac{\partial \tau_{ij}}{\partial x_j}. \tag{6-14}$$

where p is the static pressure and τ_{ij} the stress tensor given by

$$\tau_{ij} = \eta(T, \bar{\varepsilon}) \left(\frac{\partial u_i}{\partial x_j} + \frac{\partial u_j}{\partial x_i} \right) \tag{6-15}$$

where η is the non-Newtonian viscosity of the incompressible fluid from equation (6-11).

The first law of thermodynamics states that the sum of work and heat added to a system results in the increase of energy of the system. The energy of a flowing fluid particle is a sum of internal and kinetic energy if potential energy changes can be neglected. If heat transfer to a fluid element obeys Fourier's law of heat conduction and the work done on the system is due to the shear stresses one obtains the following form of the steady state energy equation:

$$\rho\, c_p(T)\, u_i \frac{\partial T}{\partial x_i} = \frac{\partial}{\partial x_i}\left(k(T) \frac{\partial T}{\partial x_i} + u_j\, \tau_{ij} \right) \qquad (6\text{-}16)$$

The two terms on the right hand side of equation (6-16) represent the conductive energy transfer and the viscous dissipation, respectively.

Equations (6-13), (6-14), and (6-16) form a non-linear set of fully coupled, partial differential governing equations of the steady-state flow of a non-Newtonian, incompressible fluid neglecting body forces and source terms. Note that the velocity gradients occur simultaneously in all three governing equations as well as in the viscosity function (6-11).

6.3 Heat Generation

It is well known from many metal forming processed that about 90% of the mechanical work involved is transformed into heat. The material flow in Friction Stir Welding can be interpreted as an interaction of extrusion of material past the rotating pin and a forging shoulder. The material flow visualization has successful shown that material is severely deformed in FSW.

If one assumes that frictional heating is the heat source one may estimate a friction coefficient as shown in this paragraph.. Midling and Grong [38] estimated the heat input in friction welding from the torque and angular velocity assuming a constant friction coefficient. Using the apparent similarity between friction welding and FSW and assuming that the pressure distribution is uniform under the FSW tool shoulder (resulting from the vertical tool force) (neglecting friction at the pin) one can estimate the heat generation. The heat input is calculated as follows if frictional heating occurs only at the tool shoulder:

$$\dot{Q} = \int \mu P \omega r \, dA = \int_{r_p}^{r_s} \mu \frac{F_z}{A_s} \omega r \, 2 \pi r \, dr = \mu \frac{2}{3} \frac{F_z}{A_s} \omega \left(r_s^3 - r_p^3 \right). \qquad (6\text{-}18)$$

In equation (6-18) $\dot{Q}$ is the net power, μ is the friction coefficient, P the uniform pressure under the tool, ω is the angular velocity, r is the radius, F_z is the vertical tool force, and A_s is the shoulder area. The indices r and s indicate pin and shoulder, respectively. Taking the welding parameters as shown and the tool dimensions of the friction stir welds as shown in Table 4-3 and comparing the estimated heat input with the actual measured power of the welds (Table C-2), the friction coefficients would be calculated between 1 and 1.7. However, friction coefficients larger than one are physically impossible. This simple comparison shows that frictional heating at the tool shoulder as the only heat source in friction stir welding may be insufficient.

Hence, we assume that it is necessary to consider viscous dissipation in the fluid as a heat source. It is assumed in the present model development that deformational heating is the only heat source in FSW. The last term in equation (6-16), which involves the viscous stresses, is often called dissipation function Φ, which is always positive.

$$\Phi = \tau_{ij} \frac{\partial u_i}{\partial x_j} \tag{6-19}$$

Combining (6-15) and (6-18) and using the velocity components u, v, w as well as the coordinates x, y, z one obtains the following form of the dissipation function:

$$\Phi = \eta(T,\bar{\dot{\varepsilon}})\left[2\left(\frac{\partial u}{\partial x}\right)^2 + 2\left(\frac{\partial v}{\partial y}\right)^2 + 2\left(\frac{\partial w}{\partial z}\right)^2 + \left(\frac{\partial u}{\partial y}+\frac{\partial v}{\partial x}\right)^2 + \left(\frac{\partial w}{\partial y}+\frac{\partial v}{\partial z}\right)^2 + \left(\frac{\partial u}{\partial z}+\frac{\partial w}{\partial x}\right)^2\right]$$

It can be seen from the above equation that viscous dissipation will be important where the velocity gradients are high. In FSW velocity gradients exist in the vicinity of the tool, with the highest values at the tool surface. Hence, the heat will be generated very close to the tool where the material undergoes the severe deformation.

6.4 Further General Assumptions for the 2-D and 3-D Models

It is assumed that no slip occurs between workpiece and FSW tool. The relative velocity between both is zero. Hence, the fluid at the tool surface rotates with the same velocity as the tool itself. Therefore, no friction occurs between tool and workpiece at the non-slip walls.

Adiabatic tools were used in all cases presented in the result chapter. Assuming zero heat flux from the workpiece to the tool violates reality to a certain degree. However, tool temperature measurements [100] have shown that the tool reaches its steady state temperature much later than the workpiece. The temperature measurements show very slow heating rates in the tool. It is concluded that despite other heat loses from the tool to the FSW machinery, only little heat flux occurs from the workpiece to the FSW tool. Therefore, the assumption of an adiabatic tool is acting as an upper temperature limit to the workpiece in the vicinity of the tool. As stated above, heat is generated in the vicinity of the tool.

7 The Two-Dimensional Process Model

Two goals are pursued modeling FSW as a two-dimensional process. The first is to prove the suitability of the flow solver as the right modeling tool and to find a solution method for solving the non-linear, coupled governing equations (equations (6-13), (6-14), and 6-16)). The second goal is to carry out parametric studies by changing the boundary conditions and the material properties. In the following sections, the flow domain, the boundary conditions, and the solution method is discussed before, the 2-D modeling results are presented in Section 7.4.

7.1 The 2-D Flow Domain

The flow domain includes a rotating cylinder representing the pin of the FSW tool. The cylinder is 10 mm in diameter in accordance with the FSW tool that was used in most of the experiments. Fluid enters and leaves the flow domain through the fluid inlet and outlet, respectively. The boundaries of the flow domain on the advancing and the retreating side are defined as moving walls. The flow domain is shown schematically in Figure 7-1. The fluid is flowing from the right to the left passing the clockwise rotating pin. Two different sizes of the flow domain were used. Domain I is 100 mm long and 50 mm wide. Domain II is 150 mm long and 100 mm wide. Both domains are smaller than the actual aluminum plates (200 mm wide and 610 mm long plates) that are usually friction stir welded at USC. Therefore, the edges of both flow domains on advancing and retreating side, respectively, are not at the edges of but within the actual butt-welded plates. It is worth mentioning that a FSW simulation using Domain II may be more accurate than using Domain I because in the latter the advancing and the retreating side are relatively close to the pin. However, the 2-D model with either domain is not thought to exactly match FSW relevant processing data such as forces and weld energy because of their simplified geometry assumption, i.e. no tool shoulder, threaded pin, or other tool details.

It was found during the model development that a high mesh density close to the pin is necessary to capture the high velocity and strain rate gradients. In general, the flow domain was discretized using an unstructured mesh of triangular cells. A mesh boundary at the pin containing very small rectangular elements accounts for the high gradients in radial direction.

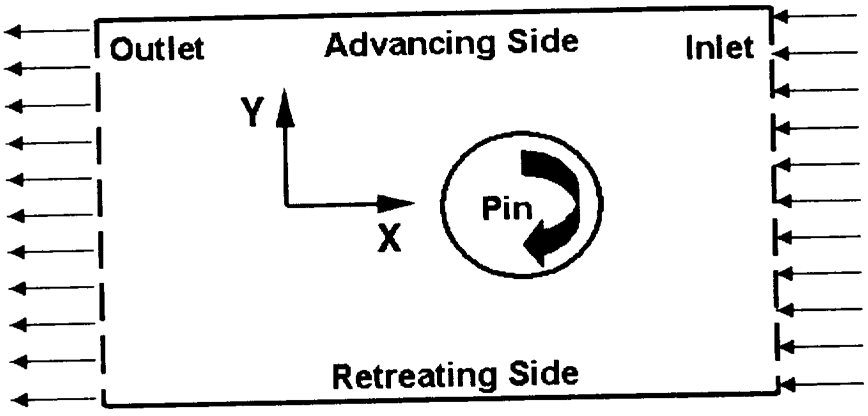

Figure 7-1 Schematic drawing of the 2-D flow domain. Fluid is flowing from the right (inlet) to the left (outlet) passing the clockwise rotating, circular pin.

Domain I consists of a rectangular zone with a cut-out hole (the pin). Cell nodes are placed at equidistance of 0.2 mm on the perimeter of the pin. The first row of rectangular cells in radial direction is 0.02 mm high. A total of 10 rows with increasing cell height are used for the mesh boundary layer in Domain I. Nodes were placed every 2.5 mm at the surrounding walls, inlet and outlet. The unstructured mesh in Domain I contains of 22177 cells (20607 triangular and 1570 rectangular) and 12022 nodes as shown in Figure 7-2. The mesh density is (unnecessarily) high in most of the flow domain. The flow Domain I was created only from one zone. Therefore, the mesh density is controlled by the node distributions at the pin and the surroundings.

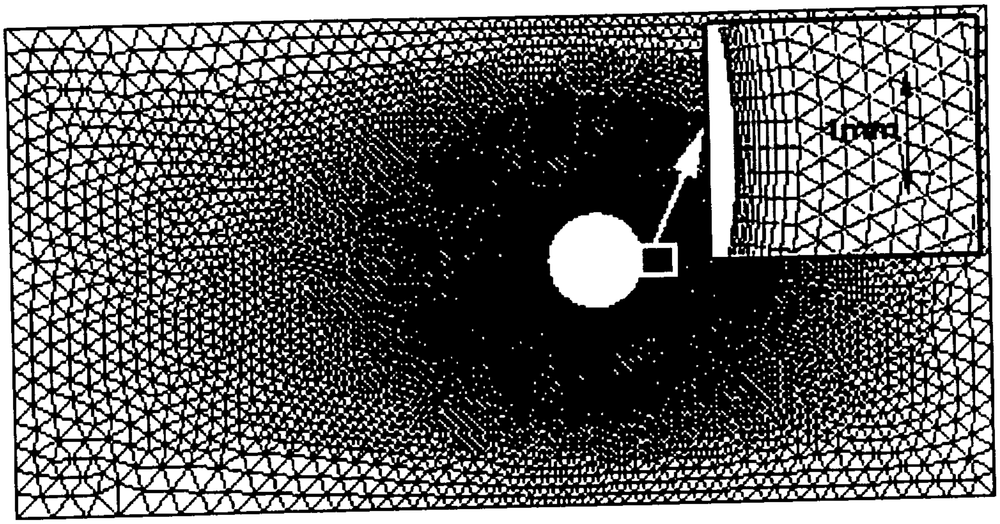

Figure 7-2 Mesh I. The magnified view at the pin shows the mesh boundary layer consisting of very thin rectangular elements.

Domain II overcomes the shortcoming of Domain I. Domain II consists of 10 different zones defining a fairly coarse mesh in the far field (nodes every 5 mm) and a very fine mesh in the vicinity of the pin. The spacing between the nodes at the pin is 0.1 mm and the height of the first row in radial direction is 0.01 mm.

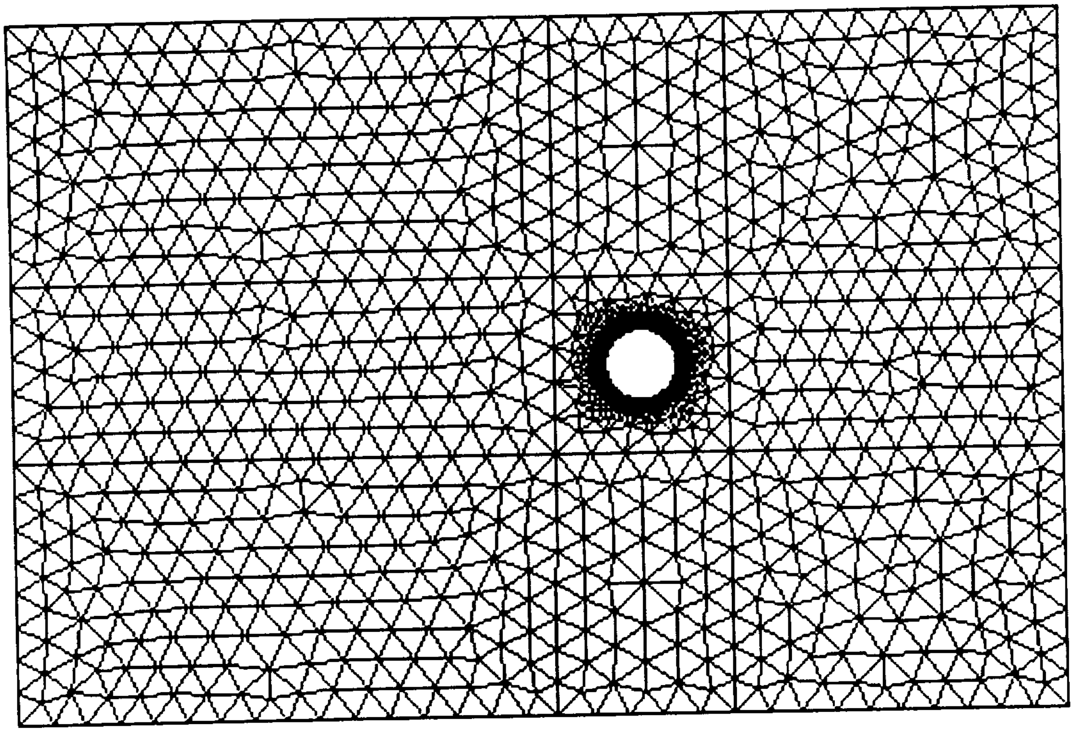

Figure 7-3 The discretized flow domain II. Mesh II is fairly coarse in regions where uniform, non-deforming material flow is expected. A high mesh density exists in the vicinity of the pin.

Figure 7-3 shows the meshed Domain II, which contains a total of 10088 cells (2826 rectangular cells in the mesh boundary layer and 7262 triangular cells). A close view of the vicinity of the pin, i.e. at the leading side, can be seen in Figure 7-4. The depth of the mesh boundary layer at the pin in the flow domain is 0.32 mm.

The mesh of Domain II is finer in the vicinity of the pin but coarser in the far field than the mesh of Domain I. It will be shown in the Section 7.4.1 that both meshes provide converged solutions. The demonstration of the mesh convergence is necessary to guarantee mesh independent solutions. In the following the meshes of Domain I and II will be referred as Mesh I, and II, respectively.

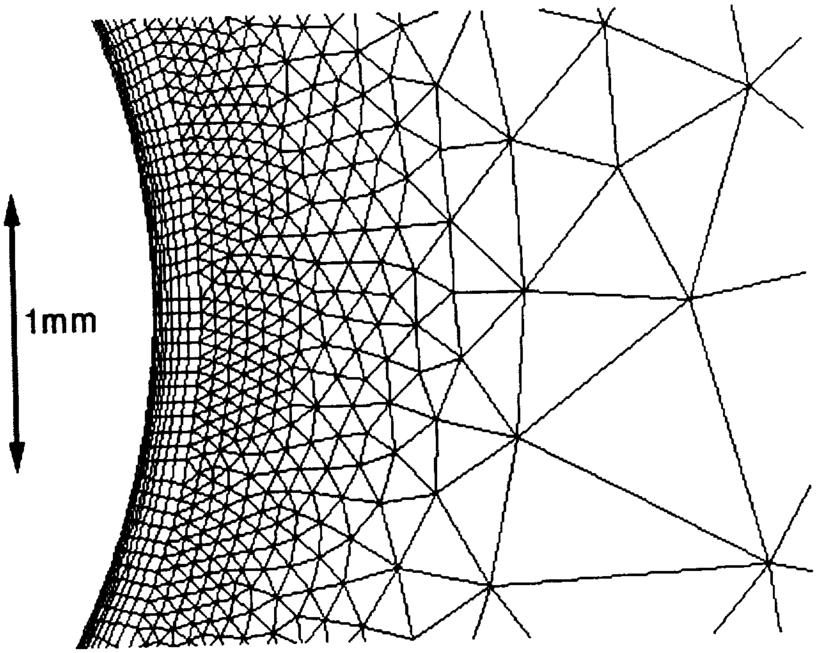

Figure 7-4 Magnified view of Mesh II at the leading side of the pin. The mesh boundary layer at the pin consists of rectangular cells, which are very small at the pin surface and increase with increasing distance to the pin.

Mesh II offers two advantages over Mesh I. First, the flow domain is larger making simulation with Mesh II a more realistic approach to simulate FSW. Second, and more important, it contains fewer elements despite its larger dimensions. Hence, simulations with Mesh II are more computational time efficient.

7.2 Boundary Conditions

In general, kinematic and thermal boundary conditions are required for solving the non-linear, coupled governing equations (6-12), 6-14), and (6-16). The welding and the rotational speed were imposed as the kinematic boundary condition at the boundaries on advancing and retreating side and at the pin, respectively.

7.2.1 Pin

The pin rotation is clockwise with a constant angular velocity. The angular velocity, or the rotational speed is one of the primary welding parameters and used as a variable in the 2-D model. A no-slip condition is assumed at the rotating wall. Consequently, fluid particles stick to the pin, in other words, the relative velocity of the fluid in contact with the pin surface is zero.

An adiabatic pin is used in the model. Neglecting the heat flux between workpiece and pin assigns an upper bound temperature to the workpiece because in actual welding the FSW tool acts as a heat sink pulling heat away from the hot, deforming material. However, tool temperature measurements have shown that for welding of aluminum with steel tools, the heat flux to the workpiece is much greater than that to the tool [60 and 100].

7.2.2 Other Boundary Conditions

Friction stir welded plates move relative to the tool with the welding speed. Therefore, fluid enters and leaves the domain at uniform velocity, the welding speed. The walls on advancing and retreating side also move at the welding speed. Therefore, the velocity gradients at the edge of the flow domain are zero.

The wall temperature on advancing and retreating side is constant at 27 °C if not stated differently elsewhere. Even though the temperature in friction stir welds is usually much higher than room temperature 25 mm off the centerline, the temperature at the boundary is not considered as a critical parameter in the 2-D model. However, we have to be aware that this results in an unrealistically high temperature gradient towards the domain boundary because the temperature drop in the transverse direction is larger than in FSW.

Moreover, the 2-D model ignores the shoulder of the FSW tool. The main focus was to create a somewhat realistic temperature distribution in the vicinity of the pin, which does not have to match exactly a real one in order to perform parametric studies.

7.3 Solution Method

In FLUENT 5.5 a segregated solution algorithm with an implicit linearization of the governing equations was applied to the discrete control volumes in the computational grid. A second-order discretization scheme for the pressure and a second-order upwind scheme for the momentum equations were used throughout the solution. The SIMPLE algorithm was used for the pressure-velocity coupling. Further information can be found in the FLUENT manuals [77]. The high viscosity of the aluminum alloy requires a certain solution method to guarantee the convergence of the solved flow field. The divergence of the solution was avoided using the following steps.

1. First, a flow field was established based on a constant pin temperature, which was estimated from the finally expected, maximum fluid temperature. In general, with a good guess of the constant pin temperature, less iterations were used for the complete solution. If no estimated maximum temperature was available, the pin temperature was chosen as of 840 K, which is close but below the solidus temperature (855 K). During this step, the viscous dissipation was disabled in the energy equation. Depending on the boundary conditions, 4000 to 5000 iterations were necessary to decrease the values of the velocities and velocity gradients to stable and reasonable levels. The velocity maximum was used as a criterion of the end of step one. The maximum velocity occurs at the edge of the retreating side; it should not exceed the product of angular velocity and pin radius.
2. Once the solution yielded a sufficiently accurate approximation of the flow field, the viscous dissipation was included in the energy equation. About 500

to 1000 iterations were necessary to stabilize the solution before further changes were made.

3. As a last step, the heat flux at the pin was set to zero. The convergence of the solution was judged from the convergence of the drag coefficient at the pin since the convergence of the pressure distribution was slowest. Depending on the welding parameters 15000 up to 40000 iterations were necessary for an accurate, converged solution.

7.4 Results and Discussion of the 2-D Model

In this section the results of the 2-D models are presented and discussed. First, the proof of mesh convergence of the two computational domains is shown. Thereafter, the flow field in the vicinity of the pin is discussed for AA6061 for different welding parameters and compared the experimentally observed flow pattern (Section 7.4.2). The modeling results such as power and forces are then compared to measurements in Section 7.4.3. The 2-D model was also used to conduct parametric studies. Therefore, the welding parameters were varied over a wide range in Section 7.4.4. Additionally, different materials (AA2024 and artificial materials) were tested with the 2-D model (Sections 7.4.5 and 7.4.6)

Simulation results include the velocity, velocity gradients, the pressure and the temperature distribution in the flow domain. In the following, the velocity field is analyzed with respect to the streamlines. Parametric studies of the welding and the rotational speed as well as of the thermal diffusivity were performed. The different weld energies, the forces and torques at the tool are shown as functions of the weld pitch (WP). All quantities of the two-dimensional model are recalculated for 8.1 mm thick plates for comparison with corresponding experiments.

7.4.1 Mesh Convergence

The mesh convergences are demonstrated for one set of welding parameters, respectively. In the following, the rotational velocity of the pin is 232 RPM and the welding speed (defined at inlet and outlet as well as the moving walls on advancing and retreating side) is 2.35 mm/s. A mesh is considered being converged if the solution yields practically the same results as the solution with a refined mesh. The refined mesh is defined by dividing every cell of the original mesh into four new cells.

7.4.1.1 Mesh I

The refined mesh of Domain I contains 88708 cells and 47791 nodes. The convergence of the mesh is judged with the force in welding direction (x-force), the torque at the pin, and the power generated during the deformation. The x-force is the sum of the viscous force (shear force) and the pressure force. The torque results from the integration of the wall shear stress along the pin perimeter. The weld power is calculated from the energy balance on the system boundaries.

Quantity	Mesh I 22177 cells	Refined Mesh I 88708 cells	Absolute Change
Force Magnitude [N/m]	1352218	1353714	+0.11 %
Torque [Nm/m]	9563.9	9575.6	+0.12 %
Power [W/m]	229886	231769	+0.82 %

Table 7-1 Demonstration of the convergence of Mesh I. Note that the quantities are presented per unit length (1 m plate thickness).

As shown in Table 7-1, the differences between the model responses of Mesh I and its refined version are very small. The refinement of Mesh I does not result in a significant change of force, torque and power. Therefore, it is assumed that the cell density in Mesh I is sufficiently high to yield a converged solution. Note that the force in welding direction is negative indicating that the fluid pushes the pin in flow direction. Flow and welding direction are of opposite sign.

7.4.1.2 Mesh II

The refined Mesh II contains 40352 elements and 26246 nodes. The components of the force vector acting on the pin, the torque and the power are listed in Table 7-2. The differences between Mesh II and its refined mesh are very small indicating the mesh convergence.

Quantity	Mesh II 10088 cells	Refined Mesh II 40352 cells	Absolute Change
Force Magnitude [N/m]	-1035549	-1059563	-2.27 %
Torque [Nm/m]	8637.36	8632.02	-0.62 %
Power [W/m]	208214.4	208214.7	+0.00 %

Table 7-2 Prove of the convergence of Mesh II.

Note that the torque, power, and the forces calculated with Mesh II are about 10 to 20% smaller than with Mesh I. Since both meshes yield accurate solutions, the differences are due to the different sizes of flow domain. The identical boundary conditions were used in both cases. The temperatures in transverse direction at the center of the pin are higher in the larger flow domain (not shown in a figure). Hence, lower tool forces may be expected if the viscosity in the vicinity of the pin is lower. It is already seen here how the boundary conditions on the advancing and the retreating side influence the model predictions. However, the following section will focus of on variations of the welding parameters such as rotational and welding speed as well as different materials, since the 2-D model is (only) a simplification of the FSW process. It is believed that in FSW the conduction heat transfer to the backing plate at the bottom of the welded aluminum plates is far more significant than the convection heat losses to the ambient air [60]. The 2-D model, however, does not account for any changes in the vertical direction.

Additionally, Domain II was discretized using a coarse node distribution at the pin. Nodes were placed every 0.3 mm on the pin perimeter. The first row of rectangular elements in the mesh boundary layer was 0.03 mm thick. The mesh, which is called Mesh III, contained a total of 3091 triangular and rectangular elements. The reason for a fairly coarse mesh was to test the mesh convergence, especially with regard to the discretization of a three-dimensional flow domain. The torque and power were calculated as 99 % and the force magnitude as 97 % of the values of Mesh II.

7.4.2 The Velocity Distribution and the Flow Field in the 2-D Model

All models in this section were carried out in the larger flow domain using Mesh II. In two-dimensional, steady state fluid flow, the concept of the stream function is most suitable to analyze the velocity distribution [73]. The stream function Ψ is defined as:

$$\frac{\partial \Psi}{\partial y} = \rho u \quad \text{and} \quad \frac{\partial \Psi}{\partial x} = -\rho v \tag{7-1}$$

Streamlines are lines of constant stream function. They represent at every instant a picture of the velocity distribution. In steady state fluid flow, streamlines and pathlines are identical.

Fluid flowing at the welding speed is material not within the domain of influence of the welding tool. Fluid at the constant and uniform welding speed does not experience any deformation. The region of uniform velocity extends over the whole flow domain except for a small region around the rotating pin. Due to the relatively high rotational speed of the pin and the high viscosity of the fluid, only a region close to the pin is affected by the tool rotation. The fluid is flowing at the constant and uniform welding velocity upstream and downstream of the pin. Outside the region affected by the pin, the material flow is that of a rigid body motion where no deformation occurs and no power is dissipated.

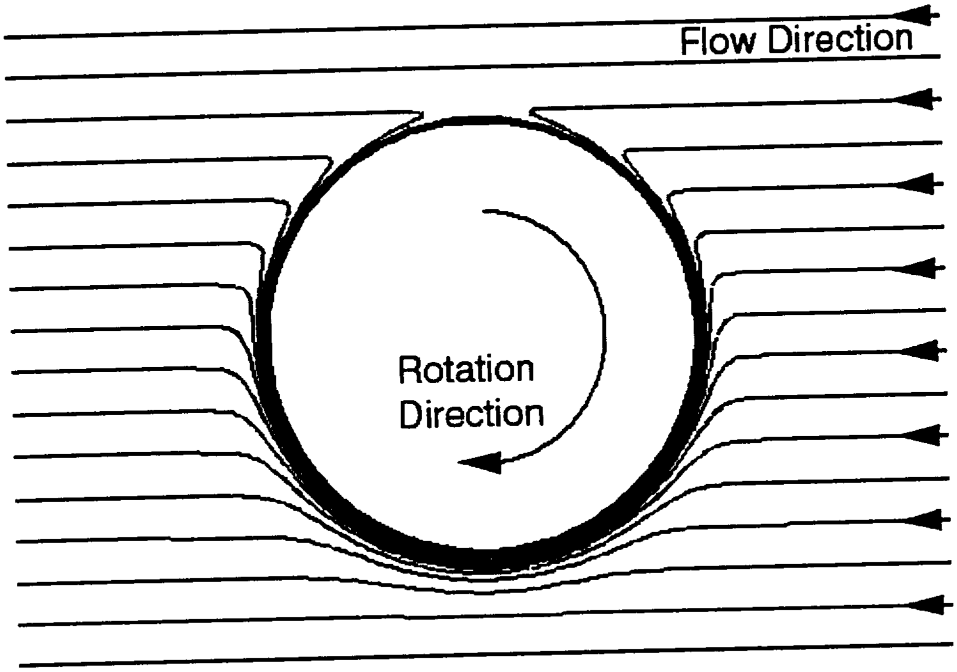

Figure 7-5 Streamlines in the vicinity of the pin. The flow direction is from the right to the left of the image and the pin rotation is clockwise. Material within the pin diameter passes the pin only on the retreating side and ends up at the same relative position to the centerline as it was before.

Figure 7-5 shows streamlines of AA6061 in the 2-D flow domain close to the pin for WS=3.3 mm/s and 232 RPM, which is a relatively high advance per revolution (weld pitch 0.853 mm/rev). In Figure 7-5, the material flow is from the right to the left past the clockwise rotating pin. The streamlines in the flow domain indicate that material, originally within the pin diameter, is transported only in the rotation direction around the pin. No material within the pin diameter is passing the pin on the advancing side whereas all the material is transported around the retreating side. The width of the deformed region is smaller on the advancing side than on the retreating side. Since all of the material inside the pin diameter must pass the pin on the retreating side, the region of deformed material is wider on the retreating than advancing side.

Furthermore, streamlines downstream end up at the same distance from, and at the same side of the centerline, as they were upstream. Since the flow is laminar, particularly creeping, the streamlines do not cross. Knowing only the final position of the marker material in a friction stir weld as shown in 5, the flow around both sides of the pin is conceivable as well. However, it will be shown that only the material flow around one side, i.e. the retreating side, explains the flow patterns observed in flow visualization experiments by Seidel and Reynolds [49]. In general, streamline plots are fairly similar for different materials (so far AA2024 and AA6061 have been tested) to those in Figure 7-5 over a certain range of rotational and translational velocity. The range of welding speed and RPM producing flow pattern as shown in Figure 7-5 depends on the material properties. It will be shown that material flow around both sides of the pin is possible at extreme ratios of the rotational to the translational velocity.

The model also predicts the presence of a "plug" of material represented by circular, closed streamlines, extending approximately 0.1 mm into the flow field as seen in Figure 7-5. Material rotates with the pin in the thin layer as a result of the no-slip condition at the boundary. It will be shown in Section 7.4.4.4 that the thickness of the "plug" depends on the welding parameters. The publication by London et al. [55] and Nunes [63] indicate that the plug is a feature of FSW. Figure 7-6, courtesy of Nunes [63], shows an enlarged view of the leading side of the pin. Close to the pin, fine-grained material is seen close to the pin. The black line seen in Figure 7-6 denotes the faying surface of the to AA2219 plates.

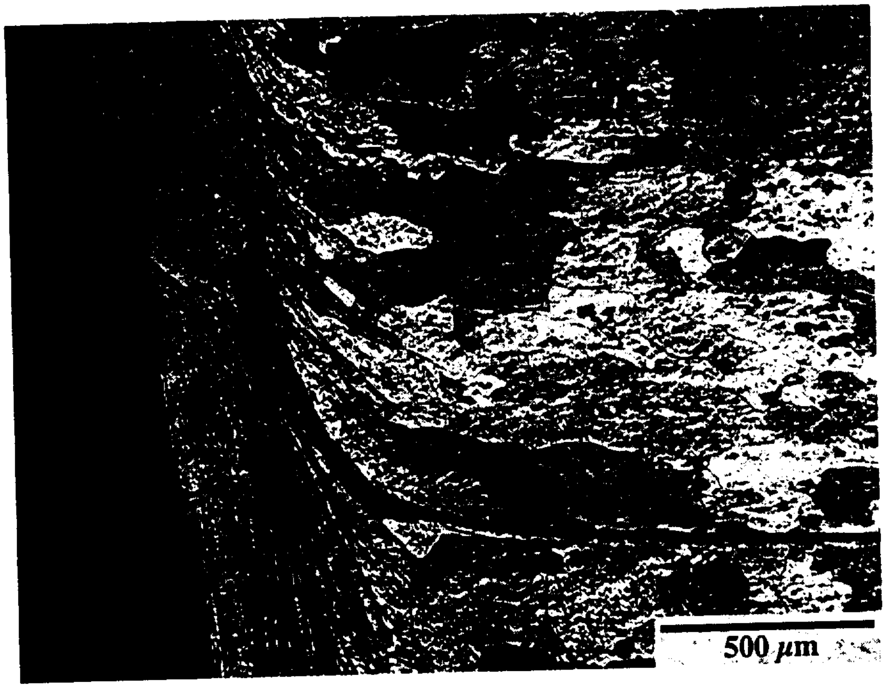

Figure 7-6 Enlarged view of a section of a Friction Stir Weld looking down from the crown on the leading side of the pin where metal is wiped onto the tool. A FSW weld in 0.317 inch thick 2219-T87 aluminum plate made at 220 RPM and 3.5 inches per minute travel speed was emergency-stopped, the tool unscrewed from the plate, and approximately 0.150 inches of metal removed from the crown side of the plate before polish and etch. The epoxy-mounting medium filling in the region formerly occupied by the FSW pin-tool exhibits bubbles (Nunes [63]).

As described in Section 5.5.4, the material flow in an AA6061 weld with a weld pitch, WP, equal to 0.853 mm/rev was using the marker insert technique. To compare the predicted flow pattern with the results of the marker insert technique, the "final" position of particles relative to each other needs to be determined in the 2-D model. If the mass-less particles are released on a vertical line in transverse direction, they end up displaced relative to each other after passing the pin. The relative positions of such particles denote the "final" positions and can be determined on the streamlines (pathlines) of these particles.

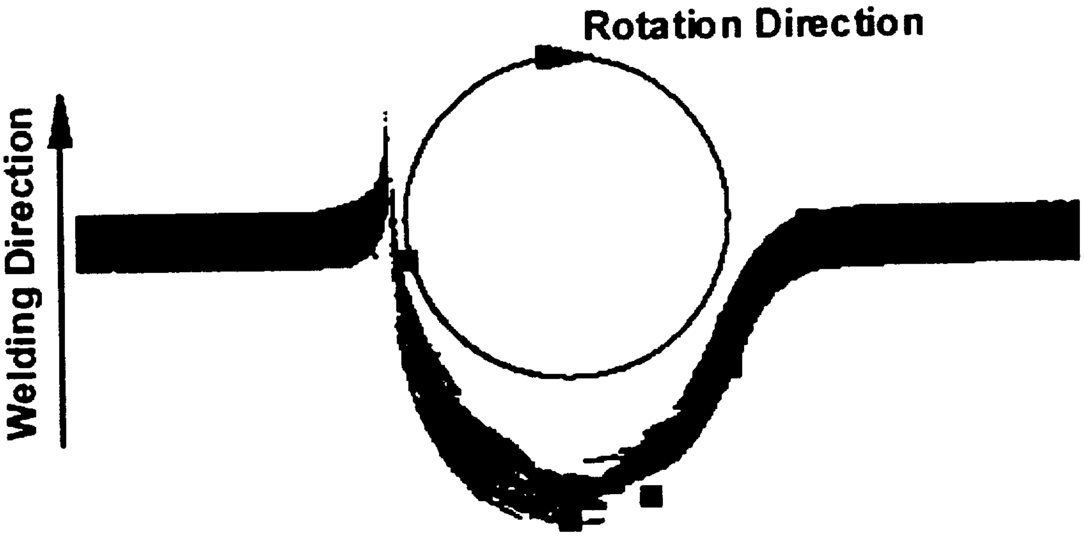

Figure 7-7 Comparison between the predicted final position and the marker inserts at the middle of the "cold" AA6061-T6 weld shown in Section 5.5.4.

Figure 7-7 shows the experimentally observed flow pattern of the "cold" AA6061 weld and the predicted final position in the flow field. The welding parameters (232 RPM and WS=3.3 mm/s) were used as input for the model. The markers from advancing (blue) and retreating side (red) at the mid-plane of the weld are shown before and after welding. The predicted final position of the particles relative to each other (black squares) and the marker position show excellent agreement. Note that in the model, particles, which are released at the centerline, end up at the centerline after passing the pin. In the actual weld, the connection of advancing side and retreating side (centerline prior to welding) is shifted slightly to the retreating side as a result of the circulation about the longitudinal axis of the weld as shown in Chapter 5.

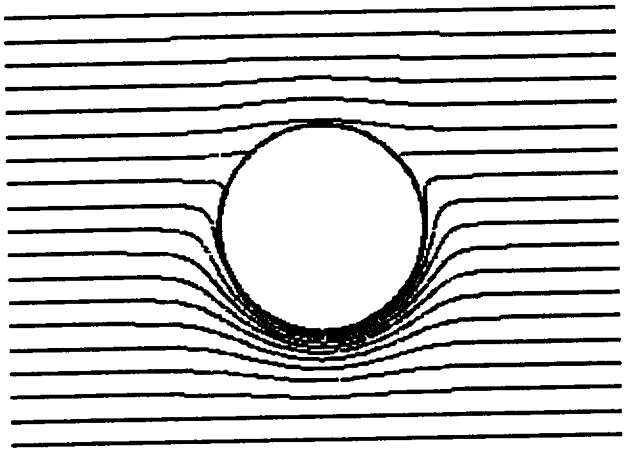

Figure 7-8 Streamlines show flow around retreating and advancing side. The simulation was performed at a weld pitch of WP=0.067 mm/s (1164 RPM and WS=1.28 mm/s).

In a series of models that were run at various RPM and welding speed it was found that material within the pin diameter could pass the pin on retreating and advancing side at very low and at very high WP. The material flow is symmetric about the centerline if the tool is not rotating. When the RPM is increased, more material within the pin diameter starts flowing around the retreating side (in the rotation direction of the tool). After exceeding a certain rotational speed, all material within the pin diameter is flowing around the retreating side only. It is believed that in "good" friction stir welds all material within the pin diameter passes the tool on the retreating side. The range of RPM and welding speed producing "good" welds depends merely on the material properties (i.e. the flow stress) if other process relevant parameters such as plate thickness and tool geometry are constant. If the RPM is increased even further, a second transition occurs where the material within the pin diameter starts to flow around the advancing side again. The effects of the different material flow patterns on the tool forces is discussed in Section 7.4.4.4. Figure 7-8 shows the streamlines for simulation carried out at a weld pitch of 0.067 mm/s using 1164 RPM and 1.28 mm/s welding speed. Here, material is flowing around both sides of the pin resulting in an increased volume of fluid affected by the pin.

In Figure 7-9 the positions of particles relative to each other are shown for two different rotational velocities (232 and 1164 RPM) at constant WS=1.28 mm/s. The final positions at 1164 RPM clearly deviate from the ones at lower RPM. If material originally within the pin diameter is passing the pin on advancing and retreating side, the experimentally determined flow pattern does not match anymore. It is worth mentioning that in a friction stir weld performed with 1164 RPM and WS=1.28 mm/s the deformed material would circulate around the longitudinal axis. The flow would be 3-D at all levels in the weld. Therefore, a comparison of the flow pattern of the markers and the two-dimensional model is not very meaningful.

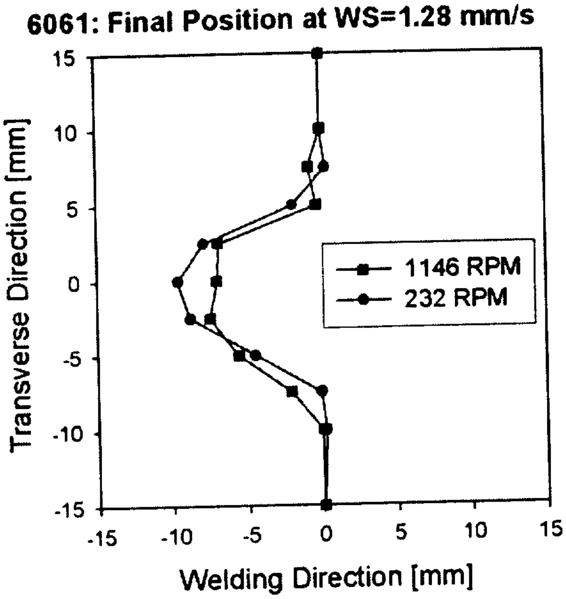

Figure 7-9 Predicted final position in AA6061 at 232 and 1146 RPM using the same welding speed (1.28 mm/s).

Strictly speaking, the 2-D model is valid only for middle and lower section of welds showing little or no vertical mixing. However, the experimental flow visualization has shown that decreasing the WP increases the vertical mixing in a weld dramatically. Even though flow in an additional third dimension exists in FSW and the flow past the pin deviates from the 2-D plane of the model, it is believed that the general material flow mechanisms (extrusion only around the retreating side) is the same as proposed in the 2-D model.

Furthermore, it is believed that material flow around the advancing side is related to weld defects in friction stir welds. Figure 7-10 shows two welds in AA2195 with weld defects. Even though the reasons of the defects were of different nature, the mechanism of the defect was the same. The transport of material from the advancing around the retreating side was inadequate in these welds causing large gaps between the two plates. It is worth mentioning that the defects seen here are extreme cases of insufficient material transport around the retreating side. It will be seen later in Figure 7-18 that some typical defects may originate in the lower part on the advancing side. In the friction stir welding defects, which are related to inadequate material transport around the retreating side, voids are left behind in the weld. In general, the "surplus" material then pushes other material towards the crown of the weld where it might appear as extra flash.

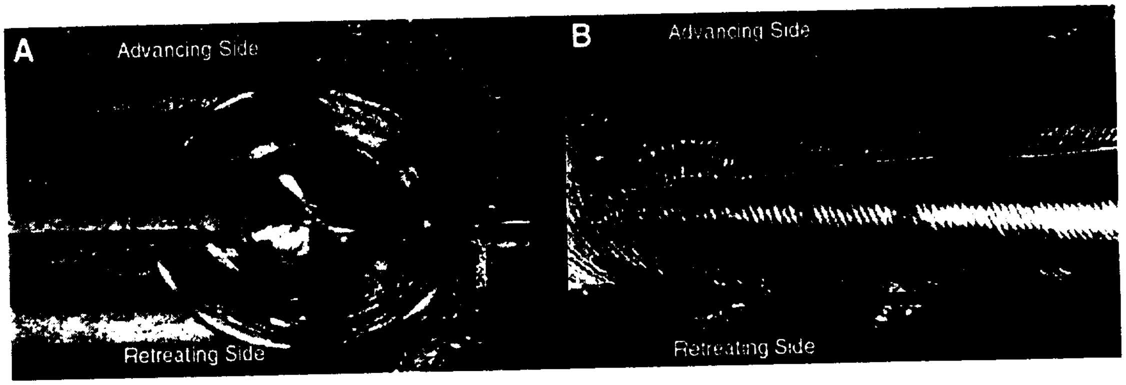

Figure 7-10 Image (A) shows an extreme case of a weld defect with a large gap between advancing and retreating side. This weld in AA2195 was performed at 832 RPM and 3.3 mm/s. The weld defect seen in (B) shows insufficiently transported AA2195 around the retreating side due to low clamping forces. The welding parameters were 390 RPM and 3.3 mm/s.

Figure 7-11 shows an exaggerated schematic drawing of a FSW defect as discussed above. If compared to the streamlines of the 2-D model as seen in Figure 7-8 the difference between the model and the FSW reality becomes obvious. Due to the fluid nature of the model, the fluid flowing around the advancing side always closes the apparent gap on the trailing side of the pin as seen in Figure 7-8. However, it is believed that material flow around the advancing side is causing the FSW defects occurring observed in actual friction stir welds.

To summarize, the occurrence of a weld defect might not be predicted at the correct welding parameters during a simulation, but the mechanism of the defect formation are likely the same in the model and in FSW, i.e. flow around the advancing side. It is worth mentioning that it is not known to what extent (if at all) a possible weld defect is related to the material transport in welding direction in lower parts of the advancing side within the extrusion zone as seen in Figure 5-7, Figure 5-9, and Figure 5-12.

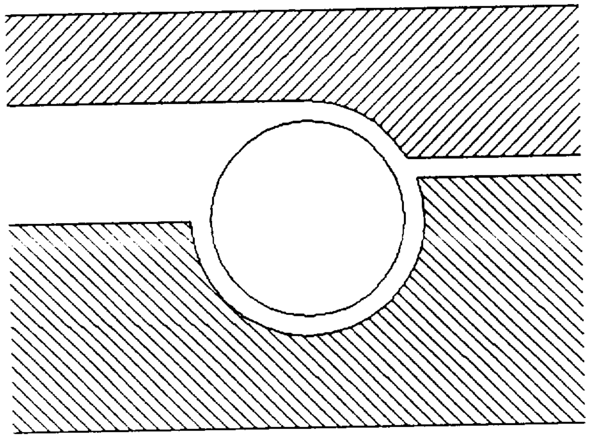

Figure 7-11 Schematic drawing of a possible weld defect due to insufficient flow around the retreating side of the clockwise rotating pin.

7.4.3 2-D Model Validation and Comparison with Experiments

As already shown in the previous section, the material flow predicted by the 2-D model matches the visualized flow pattern from the marker insert technique. For a better understanding of the quality of the model predictions more comparisons with experimental data are necessary. Friction stir welding with the FSW-PDS provides data such as the torque and the forces at the tool. In the model, the forces and torque at the pin are calculated from the pressure distribution and the wall shear stress at the pin. Additionally, the energy balance around the system flow domain provides the amount of generated power.

Furthermore, temperature measurements in a friction stir weld are available from Khandkar and Xu [98]. The comparison with the predicted temperature distribution offers an excellent opportunity to judge the correct calculation of the temperature dependent material properties.

7.4.3.1 Weld Energy and Forces

The model outputs are compared with the corresponding values measured on the FSW Process Development System at the University of South Carolina. Due to the 2-D nature and the other simplifying assumptions described above, the model cannot be validated with measurements of a real friction stir weld. However, the model should correctly predict trends that are captured in key experiments.

Load controlled friction stir welds were performed on the FSW-PDS at USC with 8.1 mm thick AA6061-T6 plates using a tool with a 10 mm pin and 25.4 mm shoulder diameter, respectively, as described in Section 4.1.2. The tool to workpiece angle was 2.5 degree. The welding parameters are listed in Table 4-3. Among other quantities, the longitudinal force (x-force), the torque, and the spindle speed were measured on the FSW-PDS. The specific weld energy or energy per unit weld length (PUWL) is a measure of the energy put into a weld and is calculated as the ratio of power to welding speed. Experimentally, the energy PUWL was determined from the torque, the spindle speed, the welding speed, and the motor efficiency.

RPM	Welding Speed [mm/s]	Weld Pitch [mm/rev]	Vertical Force [lbf] (FSW only)	Welding Date (FSW only)
232	1.279	0.331	5000	3/23/2001
	2.36	0.608	6000	3/23/2001
	3.3	0.853	6300	10/26/2001
390	1.279	0.197	4800	10/26/2001
	2.35	0.362	5000	5/21/2001
	3.3	0.508	6500	3/23/2001

Table 7-3 Welding Speed (WS) and rotational speed (RPM) of friction stir welds and models. The 2-D models were calculated using Mesh II, which is the larger flow domain.

2-D models performed with Mesh II (the larger flow domain) were calculated at the rotational velocity and the welding speeds as listed in Table 7-3. Note that the welding parameters of the models are almost the same as for the friction stir welds except for the lower rotational speed of 232 RPM instead 240 RPM.

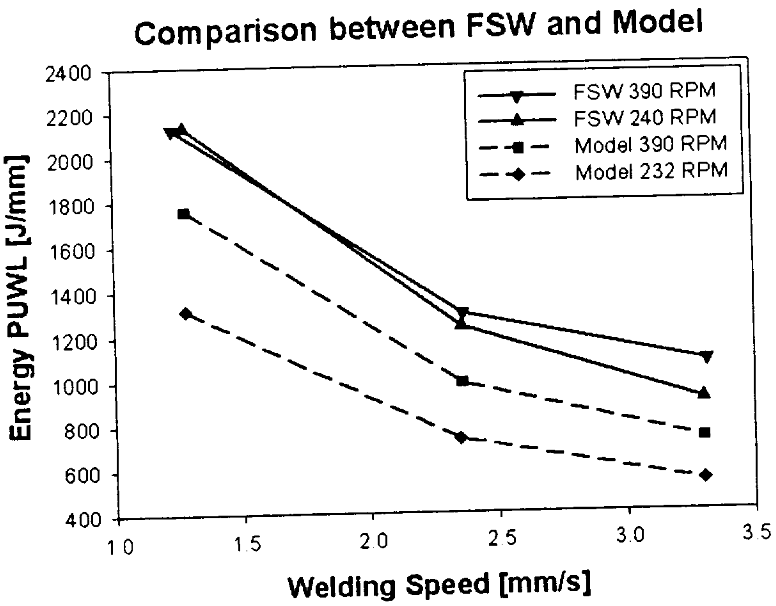

Figure 7-12 Comparison of the energy PUWL between FSW and the 2-D model using Mesh II. The decreasing energy PUWL with increasing welding speed at constant RPM is predicted correctly by the model. Note that the measured values include error margins of approximately 10%.

Figure 7-12 shows a comparison of the energy PUWL between FSW and the 2-D model using the welding parameters of Table 7-3. Generally, the measured energy is higher than the computed counterpart. Based on the differences between the 2-D model and 3-D reality, notably in the presence of the tool shoulder and the threaded pin in 3-D, the difference of weld energy is expected. The calculated energies PUWL at 232 RPM are approximately 40 % lower than the measured at 240 RPM. As seen in

Figure 7-12, the measured energy PUWL at WS=1.28 mm/s is lower at 390 RPM than at 240 RPM. At 390 RPM the energy PUWL is between 17 % and 32 % lower than measured. The 2-D model predicts the trends seen at the different welding parameters correctly. Increasing the welding speed at constant RPM (increasing weld pitch) decreases the energy PUWL in both, model and experiment. The energy PUWL also decreases in model and experiment when the rotational speed is decreased at constant welding speed with the exception at the low welding speed (1.28 mm/s). Note that the measured data (forces and torque) was acquired at different times (see Table 7-3). The early welds (old1 and old 2) were performed with not optimized vertical forces. In the most recent welds (new) the z-force was varied to obtain optimal forging pressure at the top. The optimization was done by visually characterizing the footprint of the tool on the weld surface and adjusting the z-force accordingly. Note that the torque and the x-forces are influenced by a varying z-force.

Furthermore, the measured values contain error margins of approximately 10%. These are mainly due to the inconsistency of the hydraulic oil pressure at the spindle motor of the FSW-PDS. For example, the torque measured with the tool unloaded was approximately 10% different on the different days when the friction stir welds were performed. To exclude the possible error source of inconsistencies of the measurements the average of several welds should be taken. However, in the present data only one weld was performed per welding condition.

It is believed that the anomaly at WS=1.28 mm/s (in the weld performed at 240 RPM the energy PUWL is lower than in the weld at 390 RPM) is caused by measurement uncertainties and the choice of the vertical tool force.

The forces on the tool against the flow direction are plotted in Figure 7-13 for the friction stir welds and the 2-D models using the parameters of Table 4-3 and Table 7-3, respectively. In general, the model and the experiments show the same trends. The predicted forces are at maximum two times higher than in the FS welds. Again, the shoulder effects the missing threads in the 2-D model are likely responsible for these differences. As mentioned above the measured data may contain error margins, which are not exactly known because only one weld was performed per welding condition. Regardless, the 2-D model appears to correctly characterize the effect of welding parameters on the forces and energies.

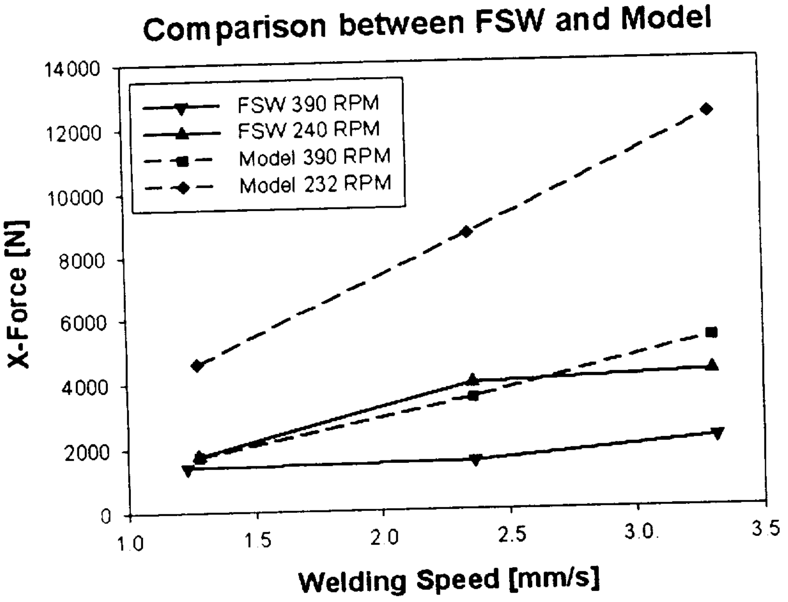

Figure 7-13 Comparison of the force in flow direction on the pin.

7.4.3.2 Comparison of Temperature Profiles

Khandkar and Xu [98] measured temperature profiles in a friction stir weld performed at 390 RPM and WS=2.36 mm/s in 8.1 mm thick AA6061-T6. They used 36 gauge K-Type thermocouples at various locations perpendicular to the welding direction at three different heights. Knowing the welding speed and the original locations of the TC's relative to the position of the tool, temperature time data was converted to the temperature-distance curves. The temperature distribution predicted with the 2-D model can be compared to the measured data. The data presented here, was acquired at the middle of 8.128 mm thick AA6061 plates.

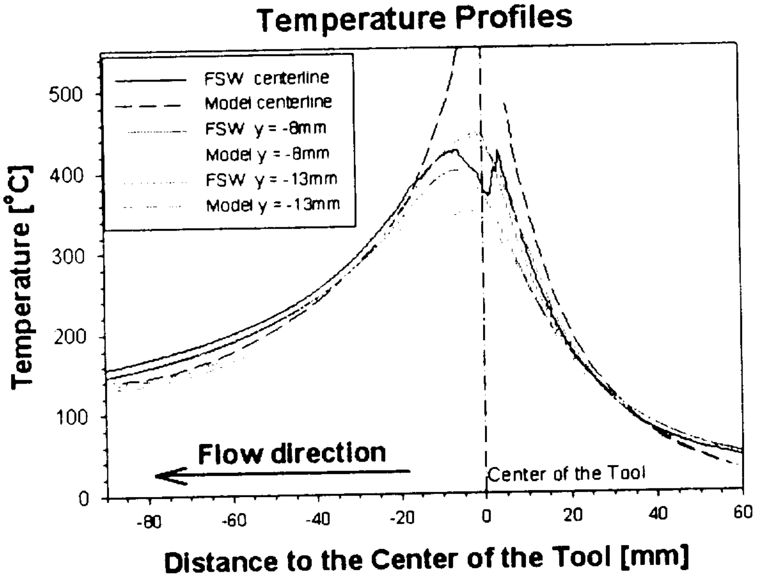

Figure 7-14 Comparison of the temperature profiles on lines in welding direction at different location perpendicular to the centerline. The welding parameters in AA6061 were 390 RPM and WS=2.25 mm/s. The measured data is taken from [98].

Figure 7-14 shows FSW and model temperature profiles at three different locations on the retreating side (negative y). The temperature is plotted against the distance to the center of the tool. The distance is positive in front of the tool and negative behind the tool. It can be seen that the model predicts higher temperatures than measured at the centerline. Remember that no heat flux is assumed at the pin. Hence, higher temperatures in the vicinity of the pin were expected. It is important to mention that the thermocouple at the centerline was obviously removed from its original position by the tool during welding. Therefore, a comparison with the model at the centerline is only meaningful at the ascending temperatures in front of the tool, i.e. at a positive distance to the tool.

At 8 mm off the centerline on the retreating side, the measured and predicted temperatures match almost perfectly. If the distance to the centerline increases (e.g. at $y = -13$ mm) the model underestimates the real temperatures. The primary reason is the thermal boundary condition on the advancing and the retreating side. A constant temperature of 27 °C was assumed at the edges of the flow domain. However, the measured temperature is higher than 27 °C and not uniform at the edges at Mesh II (± 50 mm off the centerline).

The assumption of a constant and relatively low temperature on the edges of the flow domain leads to an unnatural high temperature gradient in transverse direction as already discussed in Section 7.2.2. Figure 7-14 shows that the discrepancy between model and measured temperatures increases with increasing distance perpendicular to the flow direction. However, the predicted temperature distribution is considered good considering the simplifying assumptions of the 2-D model such as neglecting the tool shoulder, an adiabatic pin, as well as constant temperatures on the advancing and retreating side walls.

It is important to mention that the measured temperatures might be lower than the actual workpiece temperature because of improper mounting of the thermocouples. The measured temperature data is discussed in more detail in Section 8.4.1. Assuming that the welding temperatures are higher than shown in Figure 7-14 it becomes obvious that the 2D model under predicts the temperatures is FSW. Taking into account that the no shoulder effects[4] are included, one may expect lower temperatures in the 2-D model.

7.4.4 Parametric Studies of Rotational and Welding Speed

In the following, process relevant quantities are described as functions of the welding and rotational speed. Of interest are especially the forces acting on the tool, the torque, the power and the energy PUWL. In the following sections, the model data is usually plotted versus the weld pitch (WS / RPM) to combine variations of rotational and welding speed in one graph. It is important to mention that the weld pitch (WP) is not a unique welding parameter. Welding speed and RPM can be varied simultaneously resulting in a constant weld pitch, but other weld parameters may be changed: e.g. the weld power and energy per unit weld length. It will be shown that

---

[4] Due to the large strain rates close to the shoulder, more heat may be generated near the shoulder.

the welding response is different, if welds are performed at constant weld pitch but equally changed welding speed and RPM. Accordingly, "processing maps" shown as functions of the weld pitch are only valid for the welding speed and the rotational velocity that have been used to produce the results.

The welding parameters were varied over a wide range of rotational and translational speeds. Models were run at the 12 possible combinations of three different welding speed (1.28, 2.35, and 3.3 mm/s) and four different rotational velocities (116, 232, 390, and 464 RPM). Furthermore, several models were calculated at a constant weld pitch (0.423 mm/rev) varying RPM and welding speed simultaneously.

7.4.4.1 Power and Specific Weld Energy

In the model heat is generated due to viscous dissipation. Assuming that all mechanical work is converted into heat, the energy balance at the system boundaries yields the amount of generated heat.

$$\dot{Q}_{gen} = \dot{Q}_{out} - \dot{Q}_{in} \qquad (7\text{-}2)$$

Figure 7-15 shows the power at the 12 different weld pitches. A processing map as shown in Figure 7-15 is to be read as follows. Models, which were calculated at the same welding speed but at different rotational velocity are connected through solid lines. The weld pitch (WS / RPM) decreases with increasing RPM. Hence, one moves from the right to the left on the solid lines with increasing RPM. The dashed lines in Figure 7-15 connect the models at constant welding speed but varying RPM. Increasing the welding speed increases the weld pitch. Therefore, one moves from the left to the right on the dashed lines with increasing welding speed.

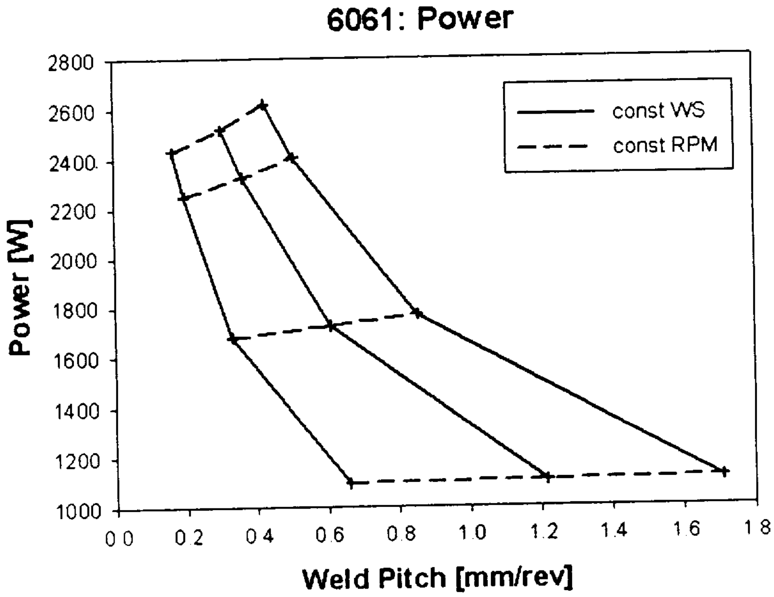

Figure 7-15 Power as a function of the weld pitch (WP). The heat generated due to viscous dissipation increases with increasing RPM at constant welding speed. Varying the welding speed at constant RPM has only little effect on the heat rate. At constant weld pitch increasing the RPM and welding speed simultaneously increases the generated power.

The higher the velocity gradients and, hence, the strain rate is, the more heat will be generated in a volume of fluid (see equation 6-16). Accordingly, the power dissipated in the workpiece increases with increasing RPM at constant welding speed as seen in Figure 7-15. Changing the welding speed at constant RPM (dashed lines) has less effect on the power generation. The power increases with increasing welding speed at constant RPM.

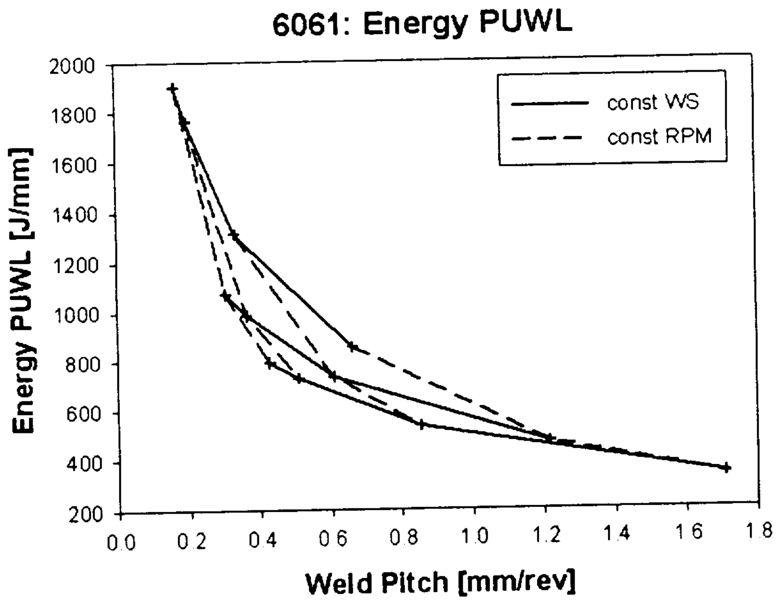

Figure 7-16 The energy per unit weld length (PUWL) is the specific weld energy. The energy PUWL is not linearly related to the weld pitch. Increasing the RPM at constant welding speed increases the energy PUWL. Increasing the welding speed at constant RPM decreases the energy PUWL. At constant weld pitch with increasing RPM and welding speed the energy PUWL decreases.

The faster the pin rotates and/or the slower the tool moves the higher the specific weld energy input. Figure 7-16 shows the specific weld energy (alternatively: energy PUWL) for the various models plotted versus the weld pitch. The energy PUWL increases rapidly at low weld pitch by either reducing the welding speed or increasing the RPM holding the other parameter constant. At high weld pitch, the slopes of the lines of constant welding speed and RPM are much lower indicating a lower energy "limit" required to produce welds. A certain RPM has to be maintained to generate enough heat for softening of the material. On the other hand, defects may occur in friction stir welds if the spindle speed is too high or too low compared to the welding speed (see Section 7.4.2). As shown above, the flow pattern (flow around the retreating side only), which explains the experimental flow visualization of Seidel and Reynolds [49], was obtained only in a certain range of rotational and welding speed.

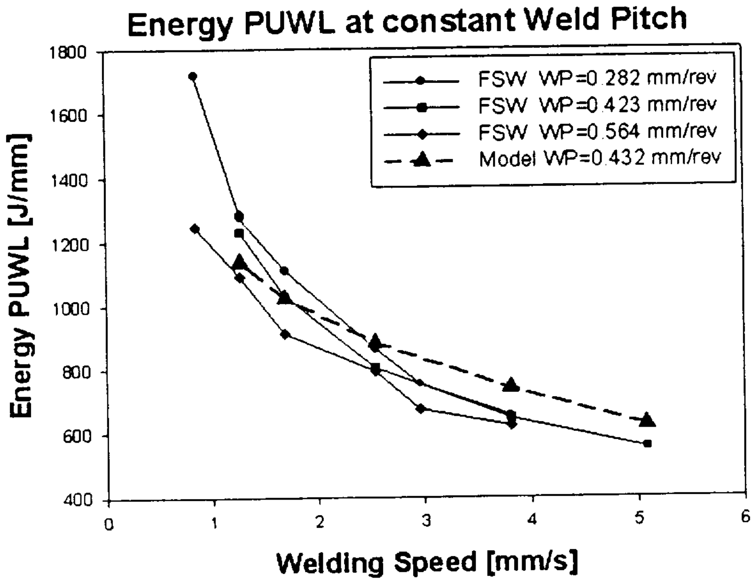

Figure 7-17 Energy PUWL at constant WP with simultaneously increasing welding speed and RPM. The FS welds were performed by [99] in AA7050-T76 whereas the models simulate AA6061.

As stated earlier, the weld pitch is not a unique welding parameter. Several models were calculated at constant WP but equally changed RPM and welding speed.

Figure 7-17 shows the energy PUWL versus the welding speed. At constant weld pitch the energy PUWL decreases with simultaneously increasing RPM and welding speed reaching a plateau at high welding speed. Furthermore, the energies PUWL at the two different weld pitch tend towards the same "constant" limit with increasing welding speed and RPM. It is worth mentioning that flow around the advancing side occurred in the cases with the highest RPM and welding speed, respectively.

Several friction stir welds were performed in AA7050-T76 using constant weld pitch by varying RPM and welding speed simultaneously. Three different weld pitches (0.282, 0.423, and 0.564 mm/rev) were used at rotational velocities between 180 and 810 RPM. In Figure 7-17 the energy PUWL is also shown as a function of the welding speed at three constant weld pitches. As in the 2-D models, the energy PUWL decreases with increasing welding speed at constant weld pitch. The three curves of measured energy PUWL in AA7050 flatten out at high welding speed. Additionally, weld defects occurred on the advancing side in welds performed at high welding speed and RPM. Evidently, the lower energy PUWL limit is accompanied by weld defects. Generally, these could be avoided by adjusting the z-axis force.

Figure 7-18 shows the microstructure of an AA7050-T76 friction stir weld performed at 540 RPM, WS=3.81 mm/s, and a z-force of 35.5 kN. The weld pitch of this weld was 0.423 mm/rev. In the lower part on the advancing side weld defects occurred.

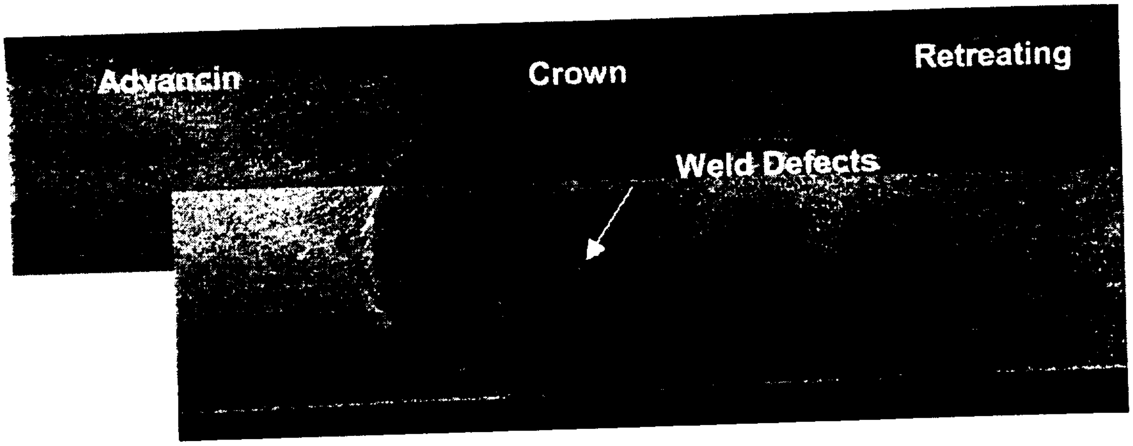

Figure 7-18 Microstructure of a friction stir weld in AA7050-T76 performed at 540 RPM, WS=3.81 mm/s, and 35.6 kN z-force. Weld defects can be seen in the lower part of the advancing side, which is on the left hand side. The image is taken with courtesy from [99].

So far, the causes of the weld defects seen at some welding conditions are not known. The 2-D model may clarify some of the unanswered questions. Both, the 2-D model and the friction stir welds show unusual behavior at high RPM and welding speed. Under these welding conditions the model predicts material flow around both sides of the pin instead of flow around the retreating side only. At the same time volumetric defects form on the advancing side in friction stir welds. Furthermore, model and experiments show the same tendency towards a lower limit of the energy PUWL. Again, it is worth mentioning that the 2-D model does not capture the 3-D aspects of the material flow in hot friction stir welds.

7.4.4.2 Torque

If the wall shear stress τ_w is integrated along the pin surface one obtains the torque at the pin.

$$M = \int \tau_w \, r \, dA = h r^2 \int_0^{2\pi} \tau_w \, d\varphi \tag{7-3}$$

In equation (7-3), M denotes the torque; r and h are the pin radius and the weld height, respectively, and φ is the angle.

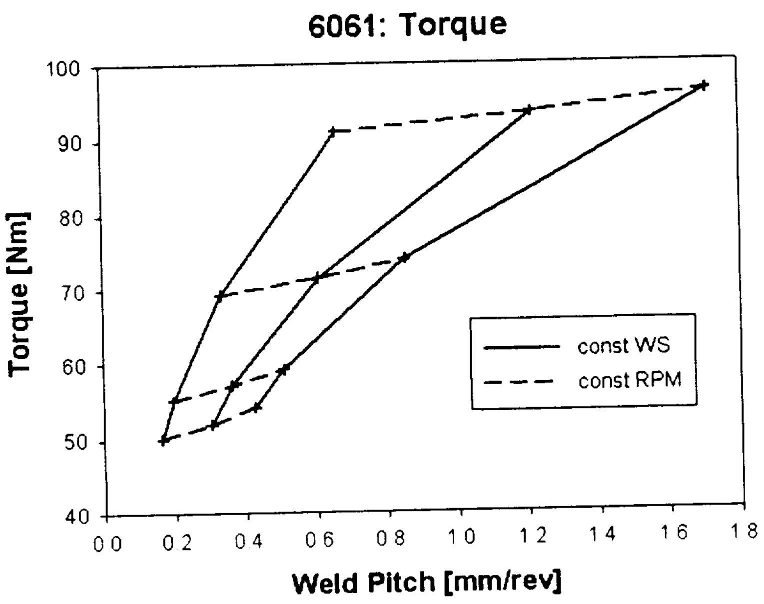

Figure 7-19 The torque at the pin decreases with increasing RPM at constant welding speed and with decreasing welding speed at constant RPM.

The torque at the pin decreases with increasing RPM at constant welding speed and increases with increasing welding speed at constant RPM as seen in Figure 7-19.

The softer the material gets as a result of increased strain rates and heating time the easier it is to maintain the pin rotation. Increasing the RPM at constant welding speed increases deformation speed resulting in a higher viscous dissipation rate and, hence, a hotter and softer material in the vicinity of the pin.

7.4.4.3 Forces

In general, the forces on the pin are the sum of the pressure and the viscous (or shear) force, respectively.

$$\vec{F} = \vec{F}_{\text{Pressure}} + \vec{F}_{\text{Shear}} = -\int p\,\vec{n}\,dA + \int \vec{\tau}\,\vec{t}\,dA \qquad (7\text{-}4)$$

In equation (7-4), p denotes the pressure, $\vec{n}$ is the unit normal of the surface, A is the area, $\vec{\tau}$ is the shear stress tensor, and $\vec{t}$ is the unit tangent of the surface.

Figure 7-20 shows the forces on the pin in longitudinal direction (x-force), which is the force of the fluid on the pin in flow direction. The x-force is linearly related to the difference of pressure minimum and maximum in the fluid (not shown in a figure). The pressure maximum and minimum always occur on the pin surface. In general, the pressure maximum and minimum are located on the leading and trailing side of the pin, respectively. The longitudinal force increases with decreasing RPM at constant welding speed and increases with increasing welding speed at constant RPM. Increasing simultaneously welding speed and RPM at constant WP increased the force in flow direction.

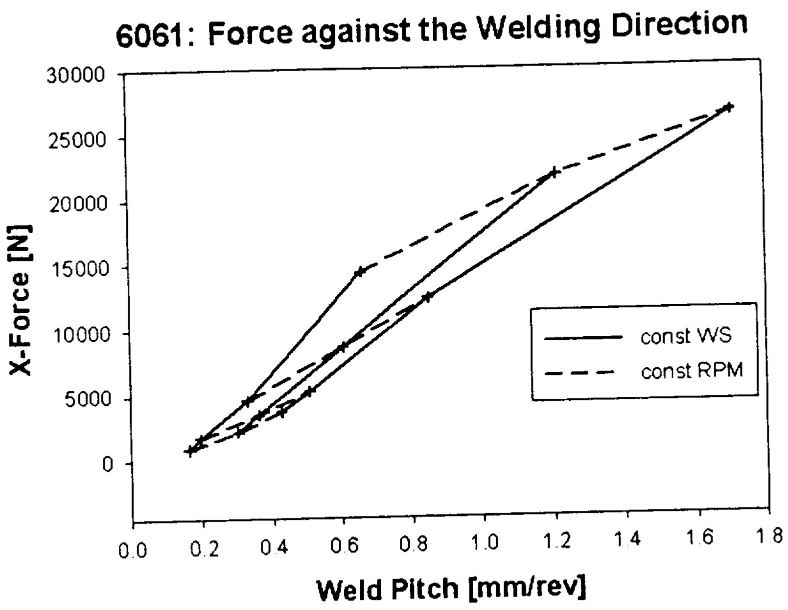

Figure 7-20 The force in longitudinal direction increases by either decreasing the RPM or increasing the welding speed holding the other parameter constant. The minimal x-force occurred at the highest rotational speed (464 RPM) and the lowest welding speed (1.28 mm/s)

The dependency of the force in transverse direction (y-force) on the weld pitch is different. As shown in Figure 7-21, the y-force changes its sign depending on the welding conditions. At 464 RPM (the highest rotational velocity) the fluid pushes the pin to the advancing side for all three welding speeds. For the other 9 simulated cases the force on the pin points towards the retreating side. If the y-force on the pin points towards the retreating side (negative sign), its magnitude increases with increasing welding speed and decreasing RPM holding the other parameter constant, respectively. At 464 RPM the y-force increases (now in the opposite direction) with decreasing welding speed. It is worth mentioning that at the magnitude of the x-force and the y-force is the same at low weld pitches. At 464 RPM and the welding speeds 1.28 and 2.35 mm/s, respectively, the magnitude of the force in transverse direction (towards the advancing side) is larger than the force in flow direction.

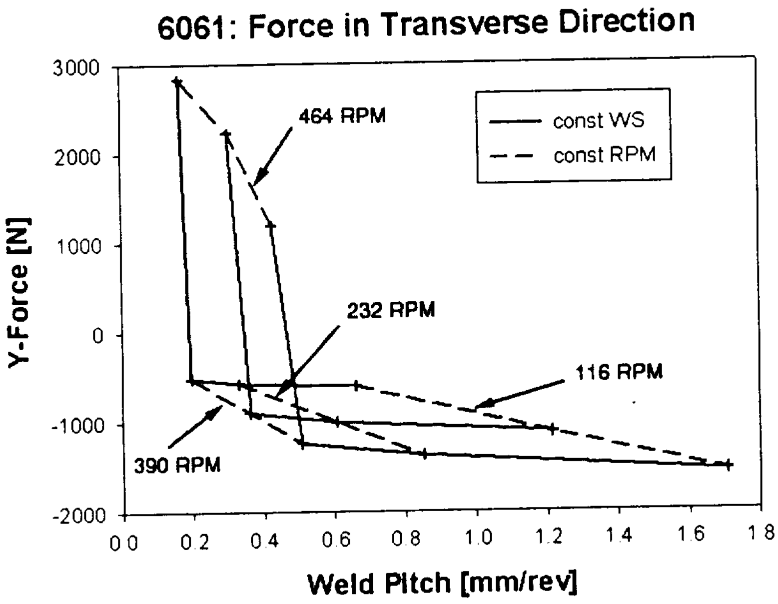

Figure 7-21 The force in transverse direction as a function of rotational and welding speed. At 116, 232, and 390 RPM the force on the pin points towards the retreating side (negative y-force). At 464 RPM the direction of the force vector is reversed. At the lower rotational velocities, the magnitude of the y-force increases with increasing welding speed at constant RPM and it decreases if the RPM is reduced at constant welding speed.

It is worth mentioning that only the force in transverse direction shows a different behavior at 464 RPM. Neither the x-force, nor the torque or the energy PUWL are qualitatively different at high rotational velocities.

Two questions arise at this point: What is different in the simulations at 464 RPM compared to the other simulated cases? And: What is causing the y-force to change its sign? A look at the pressure distribution and the streamlines may clarify these questions.

The pressure distribution in the case with the lowest weld pitch (WP=0.165 mm/rev, 464 RPM, and WS=1.26 mm/rev) is shown in Figure 7-22 and Figure 7-23, respectively. The reason to show the pressure contour plots in two separate images is to increase the number of contour level in the regions of low and high pressure, respectively. The pressure minimum and maximum occur both on the *trailing* side of the advancing side and retreating side, respectively. Even though not shown here, the pressure maximum occurs on the *leading* side of the pin in the cases calculated at the lower rotational velocities. In FSW the leading and the trailing side are defined as the front and back of the FSW tool, respectively.

Figure 7-22 The pressure minimum occurs on the trailing side of advancing side at 464 RPM and 1.28 mm/s.

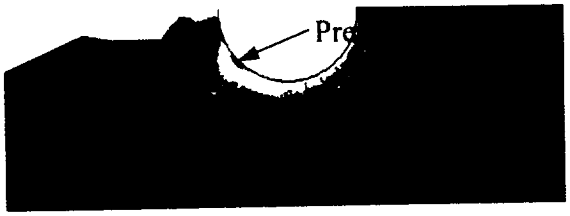

Figure 7-23 At 464 RPM and WS=1.28 mm/s the pressure maximum occurs on the trailing side of the retreating side.

The streamlines of the simulation at 464 RPM and 1.28 mm/s can be seen in Figure 7-24. Two phenomena occur in this case making it different from the streamline plot shown in Figure 7-5 for 232 RPM and 3.3 mm/s. First, the "plug" seen in the concentric streamlines, is thicker than in the other case. The plug thickness is discussed in more detail in Section 7.4.4.4. Second, streamlines within the pin diameter are separating earlier from the trailing side of the pin. Still, material is released at the same position in transverse direction as it was before passing the pin. The "plug" thickness reaches a maximum on the trailing side of the advancing side. The location of the maximum plug thickness coincides with the location of the pressure minimum. The pressure distribution (Figure 7-22 and Figure 7-23) and the streamline plot (Figure 7-24) are representative for all three simulations at 464 RPM.

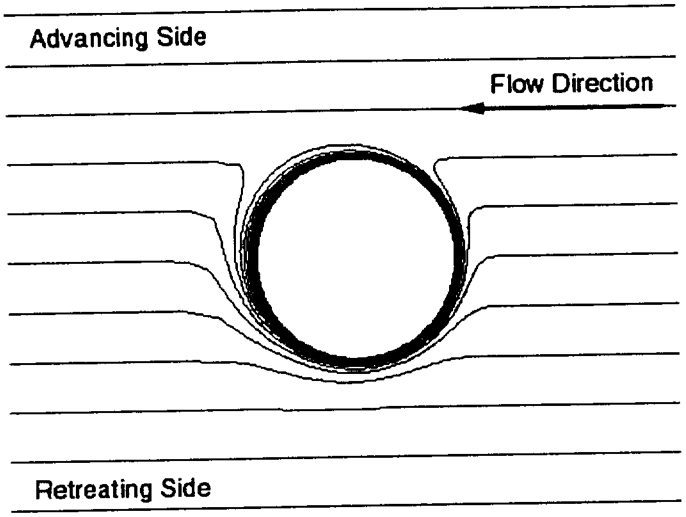

Figure 7-24 Streamlines at the pin, which is rotating clockwise at 464 RPM. The free stream velocity is 1.28 mm/s. On the leading side of the pin, the streamlines are separating earlier (meaning closer to the retreating side) from the pin than shown in Figure 7-5. In addition, the plug at the pin (concentric streamlines) is thicker than in the other case.

No measured force in transverse direction is available due to the "limited" data acquisition of the FSW-PDS. So far, the y-force in FSW was never published in the literature. Without experimental data confirmation, we cannot state if the anomaly of the y-force at high RPM is FSW or model related.

At this point two things are important to remember. First, the 2-D model simulates the FSW process only at so-called "cold" welding conditions (high weld pitch, high welding speed and low RPM), where the least vertical mixing occurs (Chapter 5). The lower the weld pitch is the more material is mixed vertically. Hence, the legitimacy of the 2-D model predicting the real process is decreasing with decreasing weld pitch. Second, the material flow in the "hot" AA6061 weld (Section 5.5.4) was qualitatively different than at the other two welding conditions. Further studies are necessary to investigate the behavior of the 2-D model at high rotational velocities.

7.4.4.4 The 2-D Model at high RPM

Nine 2-D models in this Section were calculated at one constant welding speed (2.35 mm/s) varying the rotational velocity between 30 and 955 RPM. In both extreme cases (30 and 955 RPM) material within the pin diameter passed the pin on advancing and retreating side similar to the case (1146 RPM and WS=1.28 mm/s) as shown in Figure 7-8. We will examine how the weld data such as power, forces, and the plug thickness changes with increasing the rotational speed and what the differences to the previously shown cases are.

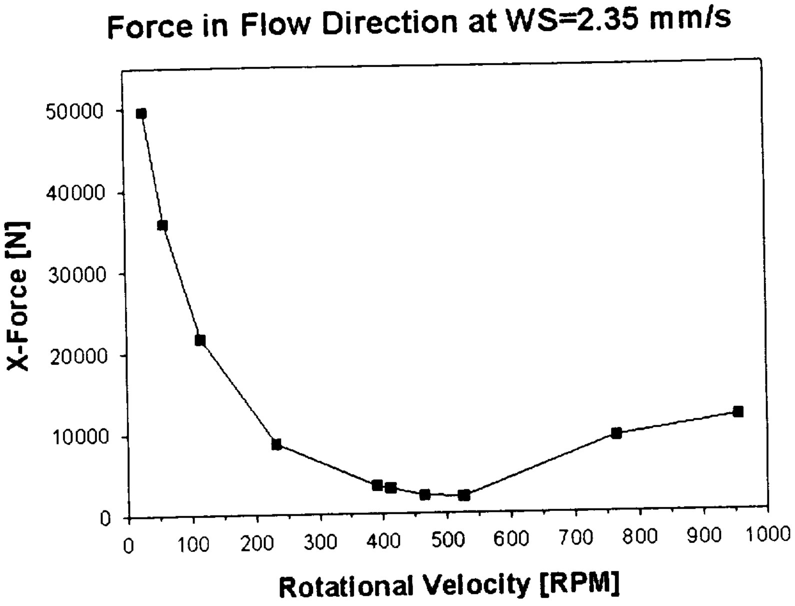

Figure 7-25 The x-force on the pin in flow direction at WS=2.35 mm/s as a function of the rotational velocity. The force decreases between 30 RPM and 525 RPM and increases between 525 RPM and 955 RPM.

Figure 7-25 shows the x-force in these cases as a function of the rotational velocity. Remember that in the previous Sections data is shown as functions of the weld pitch (WS / RPM), in which the rotational speed occurs in the denominator. Therefore, increasing the RPM corresponded to decreasing the weld pitch. As seen in Figure 7-25 the longitudinal force decreases when the rotational velocity is increased from 30 to 525 RPM. Here, the dependence of the x-force on the RPM is the same as seen in Figure 7-20. Increasing the RPM even further increases the x-force on the pin instead of further reducing the force. The minimum x-force for the cases studied is at 525 RPM. Note that at low RPM the x-force is increasing dramatically.

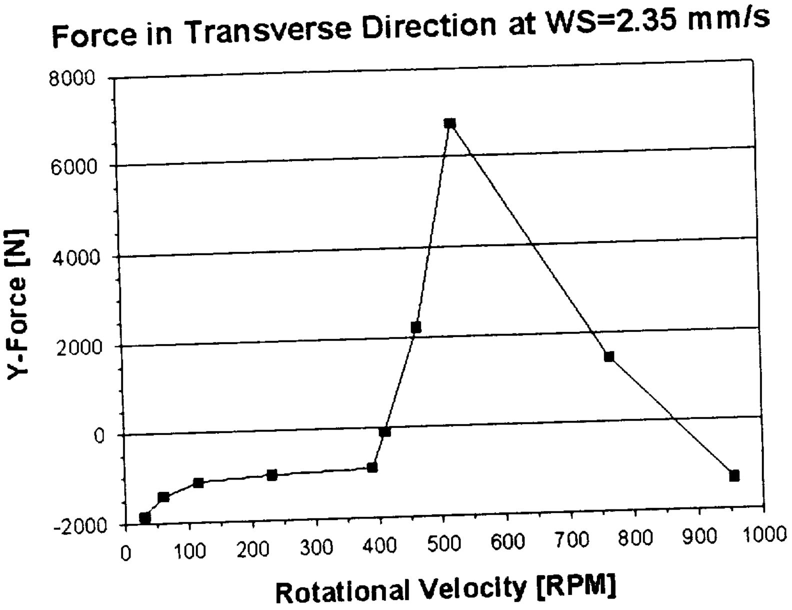

Figure 7-26 The force on the pin in transverse direction at WS=2.35 mm/s as a function of the rotational velocity.

The force in transverse direction is plotted in Figure 7-26. As already seen in Figure 7-21, the y-force changes its direction. At low rotational velocities the fluid pushes the pin towards the retreating side. At about 411 RPM the magnitude of the y-force reaches a minimum (closest to 0 N). At higher RPM, the force on the pin is positive, which corresponds to the fluid pushing the pin towards the advancing side. The maximum y-force in direction of the advancing side was at 525 RPM. Increasing the RPM even further decreases the y-force again. At 955 RPM, a case with flow around the advancing side, the pin is pushed towards the retreating side. Note that the minimum and the maximum of the magnitude of the x-force and the y-force, respectively, occur at the same rotational velocity of 525 RPM. The magnitude of the force vector is minimal at 464 RPM (not shown in a figure).

The generated power and the energy PUWL both increase with increasing RPM as shown in Figure 7-15 and in Figure 7-16, respectively. However, at the high rotational velocities (525, 764, and 955 RPM) both reach an upper plateau with only slightly increasing values. Additionally, the maximum fluid temperature is almost constant in those three cases. As a reminder, the viscosity function prevents the fluid from "overheating" due to its steep drop above the solidus temperature. Hence, exceeding a certain rotational speed does not result in more heat generation.

The material flow pattern in the vicinity of the pin changes depending on the welding conditions, here, in form of the rotational velocity. The most significant changes can be seen in the plug thickness. It is determined on the advancing side using the x-velocity as a criterion.. The sign of the x-velocity on the advancing side is positive (opposite to the flow direction) if material rotates with the pin (i.e. the plug). If material passes the pin on the advancing side, the x-component of the velocity vector never changes its sign. At the center of the pin on a line in transverse direction, the plug thickness is determined on the advancing side where the x-velocity is changing its sign.

Figure 7-27 shows the advancing side plug thickness dependent on the rotational velocity for the 9 simulated case. The plug thickness increases with increasing rotational speed up to 525 RPM. Even though not shown here, it also increases with decreasing welding speed. The maximum plug thickness of more than 1 mm occurred in the case with the lowest weld pitch performed at 525 RPM. At higher rotational velocities the plug is very thin with the minimum thickness at 955 RPM, where material within the pin diameter is passing the pin on advancing and retreating side.

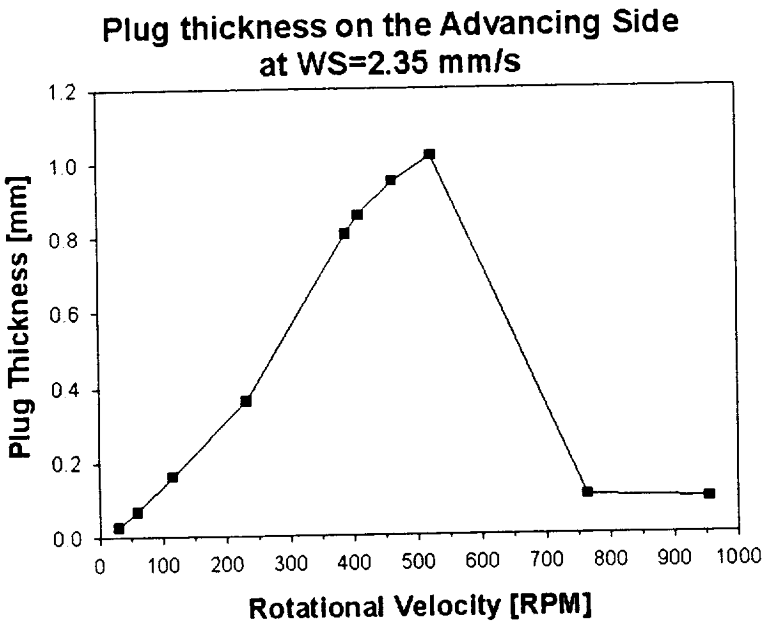

Figure 7-27 Plug thickness on the advancing side at WS=2.35 mm/s. The plug thickness increases with decreasing rotational speed before it drops to almost zero at high rotational velocities.

To summarize, at increasing RPM the forces and the plug thickness reach extrema before the flow field is changing qualitatively, i.e. flow around the advancing side. This may be interpreted as the onset of a changing flow field. The flow around the advancing side at low rotational velocities is primarily accompanied by a steep increase of the force on the pin.

7.4.5 2-D Model Simulations of the Material Flow in AA2024

The 2-D model was also used to simulate FSW in AA2024-T3. The main differences between AA2024 and AA6061 are the higher flow stress, the lower thermal conductivity, and the lower solidus temperature of AA2024. Models were carried out in the grid configuration Mesh II at the 9 possible combinations of three different welding speeds (1.28, 2.35, and 3.3 mm/s) and three different rotational velocities (80 RPM, 116 RPM, and 232 RPM). The constants of the viscosity function (equations (6-10) and (6-11)) are listed in Table 6-1 and the thermal conductivity as well as the specific heat are listed in Table 6-2. In the user-defined function (UDF) defining the viscosity of AA2024, the viscosity is forced to drop 4 orders of magnitude within 5 °C above and below the solidus temperature of AA2024 ($T_s = 502$ °C). Hence, the transition or "drop-off" temperature is 497 °C.

With the exception of the slowest welding speed, actual friction stir welds in AA2024 at the welding parameters used here, are considered to produce "cold" welds. As shown in Chapter 5 for aluminum alloys of the 2XXX and 7XXX series, the vertical mixing in a friction stir weld is minimal at "cold" welding conditions. Even though the lowest rotational speed used for the material flow visualization was 232 RPM it is assumed that welds at lower RPM produce even less vertical flow. At USC, defect free welds in the 7XXX series were performed at a weld pitch of 0.423 mm/rev using 90 RPM and WS=0.85 mm/s. In general, the window of welding parameters producing "good" and defect-free welds is smaller in the high flow stress alloys than in AA6061. The 2-D model predicts material flow around the advancing side for AA2024 at lower rotational velocities than for AA6061. For example, material flows consistently around both sides of the pin at 232 RPM at all three welding speeds used here. The streamline plots are similar to that shown in Figure 7-8 for AA6061. The other simulations at lower rotational velocities (80 and 116 RPM) revealed flow patterns similar to that of the AA6061 case shown in Figure 7-5 where all material within the pin diameter is passing the pin on the retreating side. Material flow around the advancing side is usually correlated with weld defects, i.e. wormholes, as discussed in Section 7.4.2. Its occurrence and the consequences are discussed in the following paragraphs.

Figure 7-28 shows the power generated in the 9 cases using the material properties of AA2024. The power reaches an upper limit at increasing RPM holding the welding speed constant (from the right to the left in Figure 7-28). The maximum temperature, which always occurs on the trailing side of the advancing side, is almost the same (about 498 °C) in all AA2024 cases at 116 and 232 RPM. As already mentioned in the previous section, almost no extra heat is generated in the fluid if the fluid temperature exceeds the "drop-off" temperature (here: 497 °C), above which the viscosity decreases significantly. This is especially true if the fluid temperature is above 497 °C in most of the region of the severe deformation, i.e. high strain rates. Remember that in the cases with the highest rotational velocity at 232 RPM, material flow occurred around both sides of the pin indicating a possible weld defect. The increase of power from 116 RPM to 232 RPM is lower than the increase from 80 RPM to 116 RPM. Hence, a decreasing slope of the power in the power-RPM plot accompanies the material flow around the advancing side.

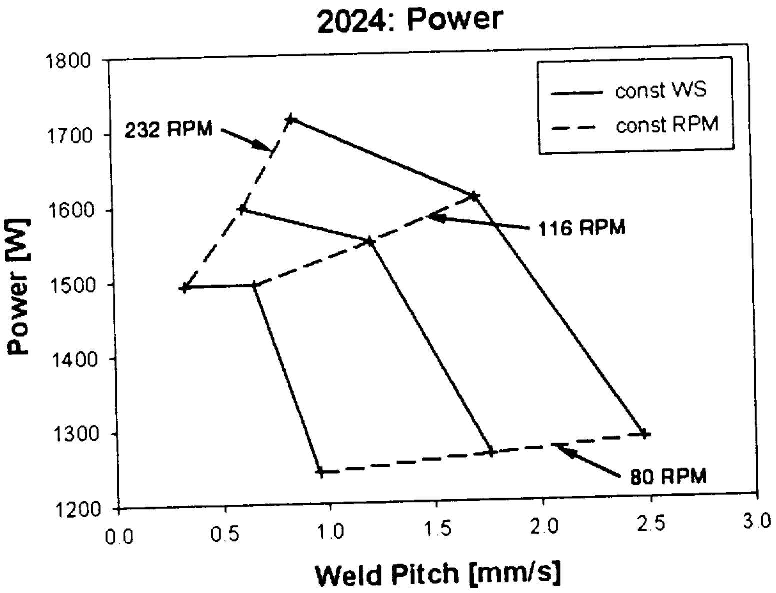

Figure 7-28 The generated power plotted versus the weld pitch in the 2-D AA2024 simulations using Mesh II.

The plot of the force in flow direction against the weld pitch in AA2024 seen in Figure 7-29 also shows a significant difference from the AA6061 x-force plot (Figure 7-20). For the cases at 80 and 116 RPM the following statement can be made. The force on the pin in flow direction increases with increasing welding speed and decreasing rotational velocity holding the other welding parameter constant. The same dependencies were shown for AA6061 in Figure 7-20. However, the x-forces at 232

RPM are <u>higher</u> than at 116 RPM at all three welding speeds. The same phenomenon[5] was already seen in AA6061 at WS=2.35 mm/s in Figure 7-25. The general dependency of the x-force on the rotational velocity is the following: Increasing the RPM at constant welding speed may result in a minimum force in flow direction if flow around the advancing side is encountered at high RPM.

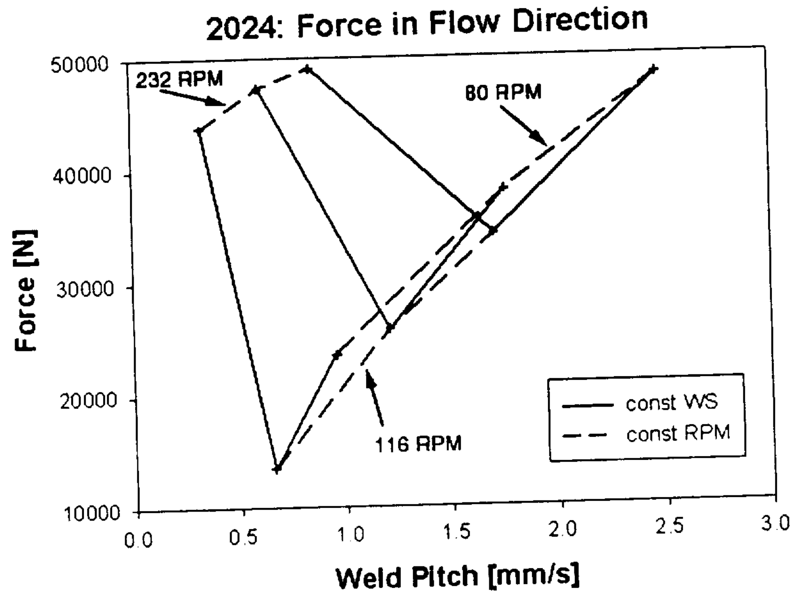

Figure 7-29 Force in flow direction in AA2024.

To summarize, the main difference between AA2024 and AA6061 is that material flow around the advancing side occurs at lower rotational velocities at the same welding speed. As already discussed in the previous sections, the force in flow direction (against the welding direction) goes through a minimum at increasing

---

[5] If material flow is only around the retreating side, the x-force <u>decreases</u> with increasing RPM. Above the rotational velocity at which material flow is also around the advancing side, the x-force <u>increases</u> with increasing RPM.

rotational velocity before the onset of advancing side flow. Additionally, the plug thickness on the advancing side is maximal at the minimum x-force as shown by combining Figure 7-25 and in Figure 7-27 for AA6061. If the RPM increases even further, the plug collapses and material at the edge of the advancing side is passing the pin on the same side instead of performing almost a full rotation around the pin.

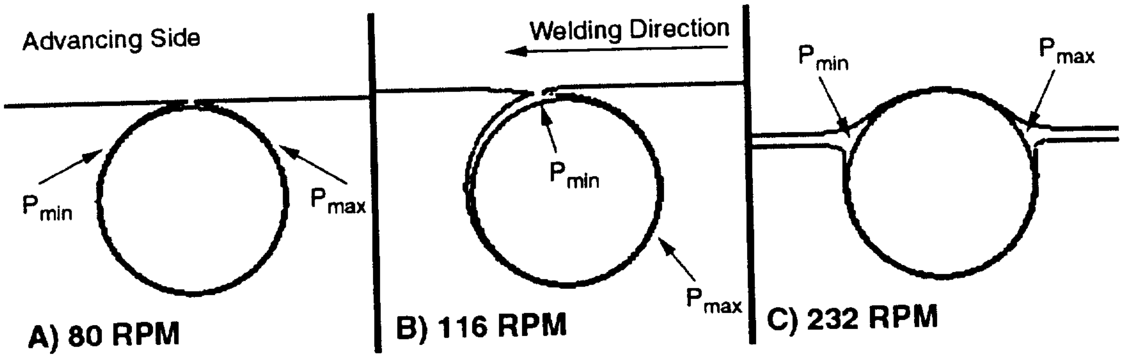

Figure 7-30 Streamlines on the advancing side of the clockwise rotating pin for three different cases at WS=1.28 mm/s in AA2024.

Figure 7-30 illustrates the different material flow at constant welding speed with increasing rotational velocity. Note that only the most significant streamline on the edge of the advancing side is shown in Figure 7-30. At 80 RPM (A) all material within the pin diameter passes the pin on the retreating side. Material flowing along the streamline, shown in (A), is almost rotating 360 degree in rotation direction around the pin. The streamline is nearly symmetrical to the center of the pin. At 116 RPM (B) the plug thickness increased and the streamline separates from the pin on the trailing side. The pressure minimum moved towards the advancing side to the location where material on this streamline is released in the uniform flow field. Finally at 232 RPM (C), material within the pin diameter is passing the pin on both sides. Note that in the latter case the pressure minimum and maximum are located at the separation of the streamlines, one passing the pin on the advancing side and the other passing it on the retreating side.

7.4.6 Artificial Materials

So far, the 2-D model was used to simulate the material flow of AA6061 and AA2024 at various welding conditions. For a certain material the material properties such as the viscosity, the thermal conductivity, and the specific heat are given in Table 6-1 and Table 6-2. The different welding characteristics of the two alloys are related to their material properties. However, it is difficult to relate a single property to the different welding responses; the influence of a single property is not known. In this section the material properties are subject to variation holding the welding parameters constant. Artificial materials are created varying one material property after the other.

To determine the influence of the viscosity on the flow field, the magnitude of the viscosity was varied. The temperature and strain rate dependence was not changed. Three cases were solved using fractions (1, ½, and $^1/_3$) of the viscosity of AA2024. The thermal properties of AA2024 were used in all 3 cases. The boundary conditions were the same in all cases using a rotational velocity of 232 RPM and a welding speed of 3.3 mm/s. The temperature at the inlet as well at the walls on advancing and retreating side was kept constant at 27 °C. The three cases were solved using Mesh II.

Table 7-4 lists the forces, power, energy PUWL, and the torque of the 3 cases. In the first case (already shown in the Section 7.4.5) material flow occurred around both sides of the pin, which is indicated by ADV+RET in the last column of Table 7-4. In the other two cases with lower viscosities material within the pin diameter passes the pin on the retreating side only. Decreasing the viscosity reduces the power, the torque, and the force on the pin in flow direction. The flow around the advancing side is accompanied by a steep increase of the x-force. At one third of the viscosity of AA2024 the force on the pin points towards the retreating side whereas it is of opposite sign in the cases of high viscosity. It was already seen in Section 7.4.4.4 in AA6061 at increasing RPM that the transverse force changes its direction before material actually starts flowing around both sides of the pin. However, the *viscosity* of AA2024 is varied in the present cases instead of the welding parameters.

Viscosity	**X-Force [N]**	**Y-Force [N]**	**Power [W]**	**Torque [Nm]**	**Comment**
η(2024)	49060.6	5085.2	1715.6	74.8	ADV +RET
η(2024) / 2	12256.6	4090.9	1676.1	70.1	RET
η(2024) / 3	10027.1	-1278.2	1386.4	58.0	RET

Table 7-4 Simulation data varying the viscosity only. The 2-D models are based on the simulation of AA2024 performed at 232 RPM and WS=3.3 mm/s using fractions of the viscosity of AA2024.

The thermal fluid properties such as the thermal conductivity (k) and the specific heat (c_p) were successively modified using the same boundary conditions in all cases (232 RPM, WS=2.35 mm/s, and T_{inlet}=27 °C). Both properties are temperature dependent as discussed in Section 6.1.2. The viscosity of AA6061 was used in all six different cases, which are listed in Table 7-5. The thermal conductivity was varied in the cases 1 – 5 a two different functions of the specific heat. Note that in the cases 1 – 3 the thermal conductivity was varied by changing only the offset of the linear function. The specific heat was changed in the cases 1, 6, and 5 using the same thermal conductivity. In the following the results are plotted against the thermal diffusivity[6] at constant temperature, which is calculated at T=27 °C (300 K) as listed in the last column in Table 7-5.

Case	Thermal Conductivity k [W/m-K]	Specific Heat c_p [J/kg-K]	Thermal Diffusivity at 300 K ($k/\rho c_p$) (10^5 m^2/s)
1	105.23 + 0.1594 T	789.90 + 0.4959 T	6.04
2	115.23 + 0.1594 T	s.a.	6.43
3	136.80 + 0.1594 T	s.a.	7.28
4	87.243 + 0.1168 T	718.29 + 0.4754 T	5.26
5	105.23 + 0.1594 T	s.a.	6.58
1	105.23 + 0.1594 T	789.9 + 0.4959 T	6.04
6	s.a.	634.59 + 0.8562 T	6.36
5	s.a.	718.23 + 0.4754 T	6.58

Table 7-5 Variation of the thermal properties.

---

[6] The thermal diffusivity, α, combines the thermal conductivity, the specific heat, and density:

$$\alpha = \frac{k}{\rho c_p}$$

Figure 7-31 shows the power generation in the various 2-D models as a function of the thermal diffusivity. Increasing the thermal conductivity increases the power significantly. Varying the specific heat has only little effect on the power in the range of the variation of the specific heat. Even though not shown here, the same dependencies were found for the force in flow direction. In the material with the higher thermal conductivity heat is pulled away from the heat source more easily. The heat source is the deforming material in the vicinity of the pin. Hence, the higher thermal conductivity yields the lower fluid temperatures as seen in Figure 7-32, which shows the temperature distribution along the centerline of the cases with the lowest (case 3) and the highest (case 4) thermal diffusivity. Consequently, the viscosity is higher in the vicinity of the pin causing higher tool forces and a higher torque.

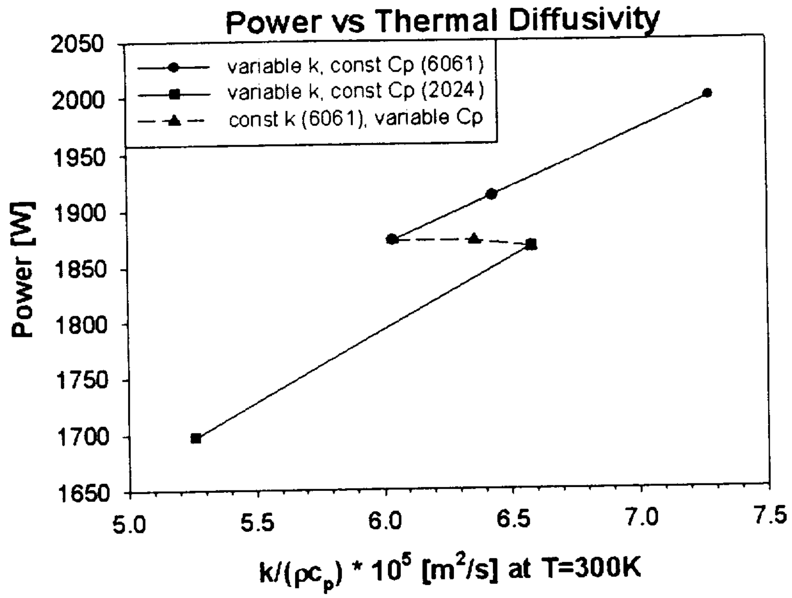

Figure 7-31 Power against the thermal diffusivity at 300K. The same welding parameters (232 RPM and WS=2.25 mm/s) were used in all six cases.

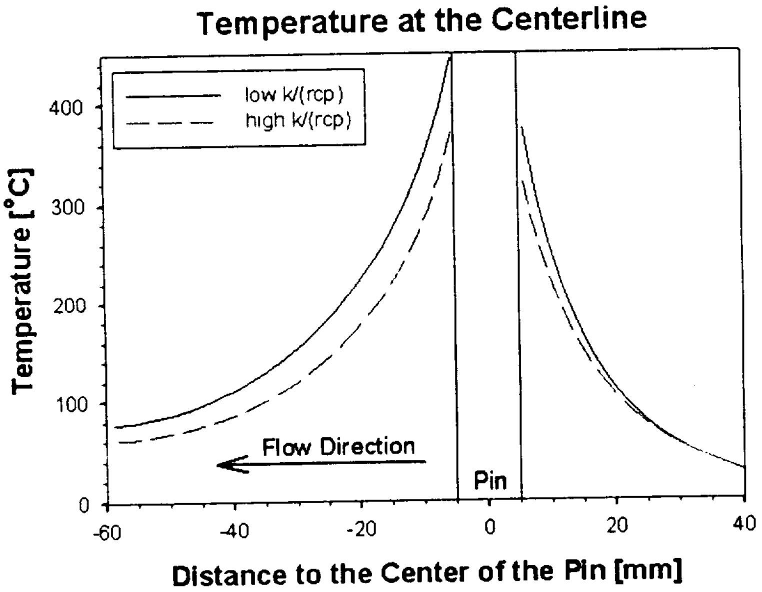

Figure 7-32 Temperature profile at the centerline for the cases of the lowest and highest thermal diffusivity.

7.5 Summary and Conclusions

A fluid mechanics based, two-dimensional process model of FSW was developed. FSW was simulated as a two dimensional, steady state, and laminar flow of a non-Newtonian fluid past a rotating circular cylinder where the FSW tool was represented by the pin only. The temperature and strain rate dependent viscosity of AA 6061 is based on a constitutive law of the flow stress of aluminum alloys using the Zener-Hollomon parameter. The thermal conductivity and the specific heat are temperature dependent. First, cold welding conditions (high weld pitch) were simulated with the 2-D model, since little vertical material movement occurred in such welds. Thereafter, the weld pitch was varied over a wide range of rotational tool velocities and welding speeds to conduct parametric studies.

The material flows at uniform constant velocity on straight streamlines towards the rotating pin. Material within the pin diameter passes the pin only on the retreating side and not on both sides of the pin. After passing the pin, material flows again at the constant welding speed at the same distance to the centerline as it was before, towards the domain outlet. The material experiences accelerations in the deformed region such that it flows further downstream than material, which passes the pin outside the pin diameter.

Particles, which were lined up in the transverse direction in the flow field before welding, end up at positions relative to each other, which match the experimentally observed flow pattern. The most obvious observation is the non-symmetric material flow about the centerline. The rotating pin transports material only around one side of the pin, namely the retreating side, to its final position in the weld. Material outside the pin diameter but still close to the pin, which passes the pin on the advancing side, experiences almost no deformation.

The model was also used to test its limits, i.e. at low weld pitch (high RPM, low welding speed). Material is flowing around the retreating and advancing side if the rotational velocity is high enough compared to the welding speed. Additionally, if the RPM were decreased at constant welding speed, material would eventually pass the pin on both sides. Finally, the flow field is symmetric about the centerline with a stationary pin. It was shown for the low weld pitch that the experimental marker position from [9] could only be matched if all material within the pin diameter is passing the pin on the retreating side. However, a meaningful comparison between the experimental "cold" weld (WP=0.853 mm/rev) and the numerical 2-D model at WP=0.067 mm/rev is not possible because a friction stir weld performed at low weld pitch produces a lot of vertical mixing.

Parametric studies of the rotational and translational speed were performed to create "processing maps" of the current 2-D model. The dependencies of power, energy per unit weld length, torque, and forces on the welding parameters can be seen in those maps. The force against welding direction at the pin increases with increasing welding speed at const RPM and decreases with increasing RPM at constant welding speed. The power increases with increasing RPM at constant welding speed and stays almost the same at varying welding speed and constant RPM. The more heat is generated in the deforming material (i.e. at low weld pitch) the less resistance the rotating and traversing tool experiences. The energy per unit weld length increases with increasing RPM and decreasing welding speed, respectively.

The measured forces are less than two times smaller and the energies PUWL are about 30% higher than predicted. However, more importantly, the same trends are shown for three different sets of welding parameters. Due to the absence of the tool shoulder, an important area of heat production is missing in the model. It is believed that a 3-D model including the tool shoulder and possibly a threaded pin will predict FSW more realistically. The 3-D model development is presented in the following chapter.

8 The Three-Dimensional Process Model

Friction stir welding is a three-dimensional process. As seen in Chapter 5, the material flow is highly three-dimensional for most of the welding conditions because of the shape of the FSW tool. The flow visualization has shown that the material flow mechanism due to the shoulder is different from that due to the pin. The validity of the 2-D process model presented in 7 is limited to the mid- section of so-called "cold" welding conditions. Hence, a more realistic process model, simulating the material flow and the heat generation in FSW, should be three-dimensional. Expanding the current 2-D model introduces many new challenges, which can be reduced to two basic questions:

1. What features need to be included in the3-D flow domain?
2. What are the appropriate boundary conditions?

To answer the first question, the following considerations were made. The more realistic the tool is represented, the more realistic the results may be. However, the influences of most of the tool details are not known. Even though friction stir welds have been performed using many different tool types [101], little research regarding tool design has been published. As shown in Sections 5.3 and 5.4, different pin and shoulder diameters were used in this research. However, all tools for the material flow visualization had common features such as a concave tool shoulder and a threaded pin with a convex tip. Additionally, the welds were performed with a fixed pin clearance at the bottom of the plates. However, the influence of neither of the above features was investigated so far.

Besides the tool geometry, the size of the flow domain comprises new modeling aspects. For example, including the backing plate avoids the unknown contact condition at the bottom surface of the plates to be welded. However, it introduces new, unknown boundaries conditions at the backing plate. Additionally, including the solid tool in the solution will complicate heat transfer calculations of the model.

As already pointed out, the influences of the tool details are not known. It is not known a priori if more details would enhance or unnecessarily complicate the model. The complications may be as follows. As shown for the 2-D model, a high mesh density is required near the tool to capture the high gradients. Including tool details and/or the backing plate may not only complicate the domain discretization, it may also increases the number of elements dramatically making the solution computationally very costly. The maximum number of elements was limited by the PC system, which was used to carry out the solution. The capacity of the system used in this research (1400 MHz CPU and 640 MB RAM) was approximately 500000 elements.

The second basic question concerned the appropriate boundary conditions, i.e. the thermal BC's. A 3-D model includes new boundaries such as the tool shoulder as well as thetop and bottom of the plates (or domain). The condition at the bottom surface of the aluminum plate is important in FSW, since it is believed that most of the heat generated during the deformation process is transferred to the FSW machine through the backing plate [100]. Even though the plates to be welded were clamped to the backing plate, it is likely that the contact resistance is not uniform at the bottom , i.e. below the tool. To the knowledge of the author, no research was ever conducted to investigate the influence of the vertical tool force on the thermal contact at the bottom of the workpiece. It was shown in the 2-D model that the assumption of an adiabatic pin yielded a reasonable temperature distribution. However, in a 3-D model the heat transfer boundary condition at the tool may require modifications, e.g. convective heat transfer.

To summarize, the development of a 3-D model automatically creates new boundaries. The boundary conditions at the new domain boundaries are not known.

8.1 The General 3-D Modeling Approach

The goal of the present research project is to model a conventional FSW butt weld as shown in Figure 2-2. The 3-D model considers only the steady-state part of FSW. The following simplifications and assumptions were made:

- Cylindrical, non-threaded pin

- Flat shoulder
- Flat top surface with convective heat transfer
- Convection at the bottom surface
- Advancing and retreating side boundaries "within" the FSW plate-size
- The flow domain does not include the backing plate or the solid FSW tool.

Using a non-tilted tool with a non-threaded pin and a flat shoulder avoids complications of the modeling techniques such as a moving mesh. Most of the friction stir welds presented in this research were performed with a tilted tool. However, the most recent tool development is focused on so-called zero-degree tools. Therefore, modeling a non-tilted tool is close to reality.

Modelling the flat top surface as a moving wall prevents material from "leaving" the domain vertically. Hence, the flash usually occurring in FSW is not captured by the 3D-model. However, excessive flash, as seen in Figure 7-10-A, does not appear under "regular" welding conditions. It is assumed that neglecting the free-deformable top surface of a friction stir weld does not alter the material transport greatly.

Convective heat transfer is assumed at the bottom and top surface of the flow domain. Chao et al. [60] and [100] modeled in their finite element heat transfer model the surroundings as convection boundaries. Chao et al. obtained the convection heat transfer coefficient at the bottom surface in an iterative process by matching experimental temperature data. The obtained values were used as starting values for the present 3-D model.

Excluding the backing plate from the model had basically two reasons. First, it did not further increase the number of elements. Secondly, the appropriate size of the backing plate and the boundary conditions are not known. Hence, including the backing plate would not improve the model. In contrast, it would further complicate the model since new unknown boundary conditions (e.g. at the bottom of the backing plate) need to be determined in an iterative process matching experimental data such as temperature profiles. However, an iterative process with a larger mesh size is computationally more expensive than with a smaller mesh size excluding the backing plate.

In the following sections the x, y, and z-coordinate denote the flow direction, the transverse direction, and the weld height, respectively. The origin of the coordinate system is at the bottom of the center of the tool. Accordingly, the weld height increases from the bottom to the top from 0 to 8.13 mm. The x-coordinate points in opposite direction of the flow direction. Fluid enters the flow domain at the flow inlet at x = 60 mm and leaves it at the flow outlet at x = -90 mm. Note that flow direction and welding direction are of opposite sign. The transverse direction points from the retreating to the advancing side. Hence, the y-coordinate is negative on the retreating side and positive on the advancing side (see also Figure 8-1). The coordinate system in the 3-D flow domain is consistent with the coordinate system of the 2-D model.

Figure 8-1 shows a schematic drawing of the initial 3-D flow domain projected on the x-z-plane. Note that the tool shoulder is modeled as a rotating wall at the same height as the top surface even though it is shown as a cylinder in Figure 8-1. Since most of the friction stir welds were performed with the "standard" tool (tool #1 in Table 4-6), a 10 mm pin and a 25.4 mm shoulder diameter were chosen, respectively. The cylindrical pin covers the total height of the flow domain unlike in FSW where the pin clearance at the bottom surface is approximately 0.08 mm. Hence, no material can pass the tool below the pin.

The dimensions of the three-dimensional flow domain in the x, y, and z-direction are 150 mm, 100 mm, and 8.128 mm, respectively. Note that the dimensions in the x-y-plane are the same as in the 2-D model using Domain II.

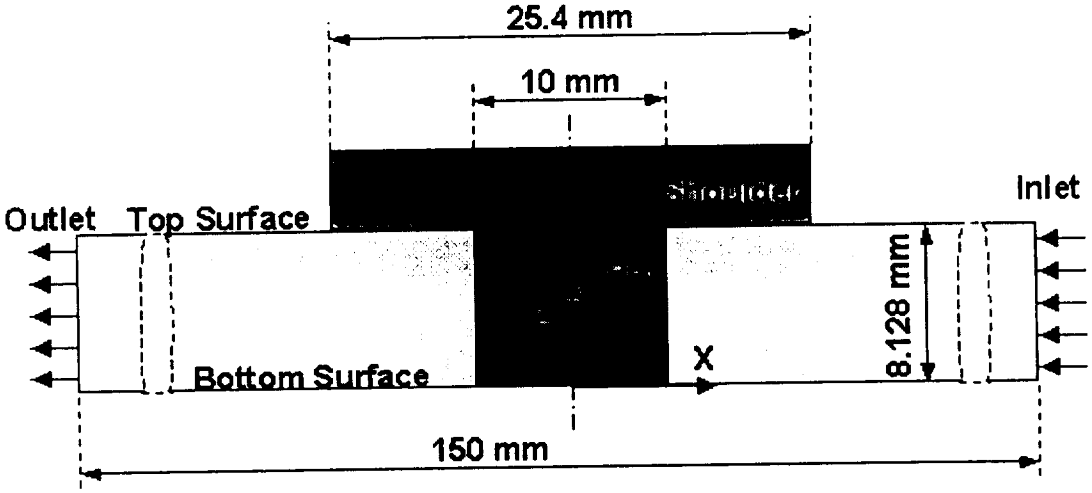

Figure 8-1 Schematic drawing of the 3-D flow domain projected on th x-z-plane.

The material to be modeled was AA6061-T6. The same material properties were used as in the 2-D model.

8.2 The 3D-Mesh

As already pointed out, the total mesh size is a critical factor for the discretization of the flow domain. It was shown in Section 7.1 for the 2-D domain that a high mesh density at the pin was necessary to capture the high velocity gradients. Hence, a high mesh density is required at pin and shoulder in the 3-D model. On the other hand, a fairly coarse mesh is sufficient in the region of uniform flow.

The mesh was created such that the transition from high to low mesh density occurs relatively close to the tool. Nodes were placed every 0.25 mm on the edges of the pin and the shoulder, respectively. The pin and shoulder surfaces were discretized using triangular elements. Additionally, a mesh boundary layer (similar to that in the 2-D mesh), consisting of very thin wedge elements, extends normal to the tool surface in the flow domain. Figure 8-2 shows parts of the 3-D mesh at the pin projected onto the x-y-plane. The elements within the mesh boundary layer (seen as rectangular elements in Figure 8-2) increase with increasing distance normal to the tool surface. The first row of elements at the tool surface is 0.025 mm high. In the far field, nodes were placed every 5 mm. The volume of the flow domain was meshed using tetrahedral elements. The final, three-dimensional mesh contains a total of 306728 wedge and tetrahedral elements.

Due to the high number of elements, no mesh refinement is possible. The refined mesh would contain roughly 1.2 million elements, exceeding the capabilities of the current PC-system. It is assumed that the mesh density is sufficient for mesh convergence. It was shown in the 2-D model that a Mesh III, created with a node distribution every 0.3 mm on the pin perimeter and a mesh boundary starting with 0.03 mm thin elements, yielded practically the same results as a model using a very high mesh density (Section 7.4.1.2).

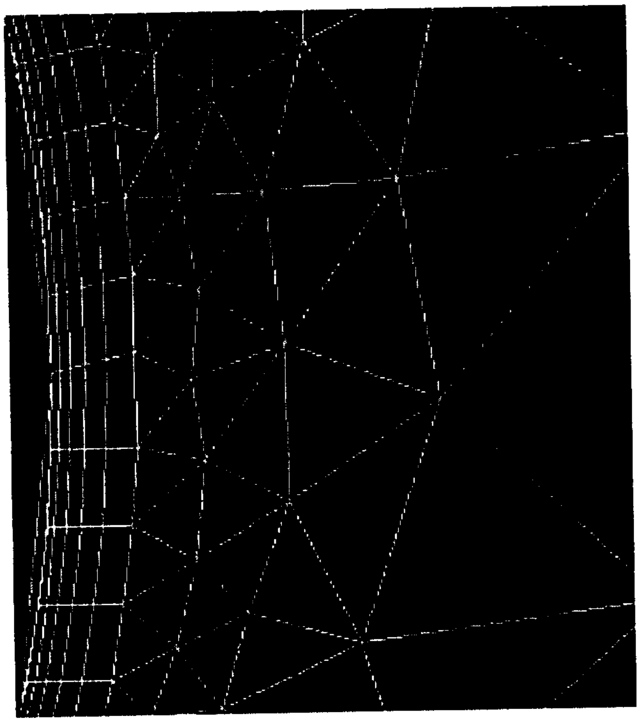

Figure 8-2 Projection of the 3-D mesh at the pin onto the x-y –plane. The image is a view from the bottom of the flow domain. The very thin hexahedral mesh boundary elements exist only at the tool surface. The rest of the flow domain is discretized with tetrahedral elements.

A second flow domain was created using a lower node density at the tool. The length and the width of the previous domain were doubled. The larger flow domain was 300 mm long, 200 mm wide, and 8.128 mm high. The size of the tool was not changed. The dimensions of the large flow domain y- and z-direction correspond to those of the actual aluminum plates that were friction stir welded. In the coarse mesh, nodes were placed every 0.4 mm instead of every 0.25 mm along the edges at the tool. The first wedge elements in the mesh boundary layer were 0.03 mm thin. The coarse mesh contained a total of 155308 tetrahedral and wedge elements. Models of this mesh were carried out to test the influence of the boundary conditions. Due to the lower mesh density, instabilities occurred for some conditions during the computation. These instabilities affected mainly the pressure distribution so that only "quasi-converged" solutions were obtained with the coarse mesh. Therefore, it was decided to use this mesh only for qualitatively judging the influence of the boundary conditions. However, the overall performance of the models for the coarse mesh that were carried out at the same boundary conditions as models in the fine mesh was relatively good. In general, power and torque were within 5 % and forces within 25 % of the values of the fine mesh. Results of models using the coarse mesh are discussed in Section 8.4.3.

In the following, the regular mesh is called 3D-test-9. The mesh of the large flow domain using the coarse mesh is called 3D-test-8-2.

8.3 Initial Boundary Conditions

The boundary conditions presented in this section are starting values for the 3-D model and may be subject to variation to fit the 3-D model to experimental data such as temperature profiles, torque and force data.

8.3.1 BC's at the Tool

The tool (pin and shoulder) rotates with a constant angular velocity. The spindle speed used in actual friction stir welds is used as an input. Since the 2-D model yielded promising results, it was assumed first that no heat flux occurs between the workpiece and the pin. Hence, the tool surface was assumed as an adiabatic, rotating wall. As already seen in the 2-D model, the adiabatic tool serves as an upper limitation to the fluid temperatures. The heat generation occurs close to the tool in regions of high velocity gradients. If no heat is transferred to the tool, all the generated heat must transfer to the surroundings of the flow domain. However, if heat is lost to the tool, the temperatures will most likely be lower than with an adiabatic tool.

Other models were carried out with approximated heat transfer coefficients at the tool, in order to simulate a heat sink at the tool.

8.3.2 BC's at the Top and Bottom of the Domain

The top and bottom of the flow domain are modeled as moving walls with convective heat transfer to the surroundings. Both walls are moving at the welding speed. The heat flux q" due to convection is computed as

$$q'' = h_f(T_w - T_f) = h_{ext}(T_{ext} - T_w) \tag{8-2}$$

where h_f and h_{ext} are the fluid side and external heat transfer coefficient, respectively. In equation (8-1), T_f and T_{ext} denote the fluid side temperature and the external heat sink temperature, respectively. The external heat transfer coefficient and the heat sink temperature are the user inputs.

In general, the top surface of a friction stir weld is exposed to air at ambient temperature. At the top surface, a convective heat transfer coefficient of 30 W/m^2-K is used. According to Chao et al., ([60] and [100]), the value is typical for natural convection between aluminum and air due to air flow caused by spindle rotation, there may be significant forced convection at the top surface.

Due to the high pressure at the bottom surface and the contact to the steel backing plate, a higher heat transfer coefficient is used. Chao et al. published values of 200 W/m^2-K and 350 W/m^2-K for 6.1 mm thick AA6061 and 8.1 mm thick AA2195, respectively. As already mentioned, they obtained their heat transfer coefficients in an iterative process from matching experimental and predicted temperature profiles.

Models were carried out with uniform convective heat transfer coefficients at the bottom surface, which was assumed as 500 W/m^2-K in most of the models presented here. A constant external heat sink temperature T_{ext} of 27 °C was used at top and bottom surface assuming that air temperature and the FSW machine temperature are the same.

8.3.3 BC's at the Walls on the Advancing and the Retreating Side

The moving walls on advancing and retreating side are within the 200 mm wide aluminum plates that are usually welded at USC. Hence, the model is surrounded by the workpiece in transverse direction. The most appropriate boundary condition is a temperature boundary condition. Khandkar and Xu [98] measured the temperatures at various locations in a friction stir weld of AA6061-T6 performed at 390 RPM and 2.35 mm/s welding speed. For example, they measured the temperature profile at the edge of the present flow domain on the retreating side at three different locations. Temperature measurements performed using an infrared camera have shown that the temperature difference between advancing and retreating side is negligible, 50 mm off the weld centerline. By neglecting the vertical temperature gradient at the domain edges at y=±50 mm one can linearly approximate the temperature profile at the edges of the flow domain as a function x, which is in the longitudinal direction of the flow domain. Figure 8-3 shows how the temperature at the walls on advancing and retreating side changes in x-direction

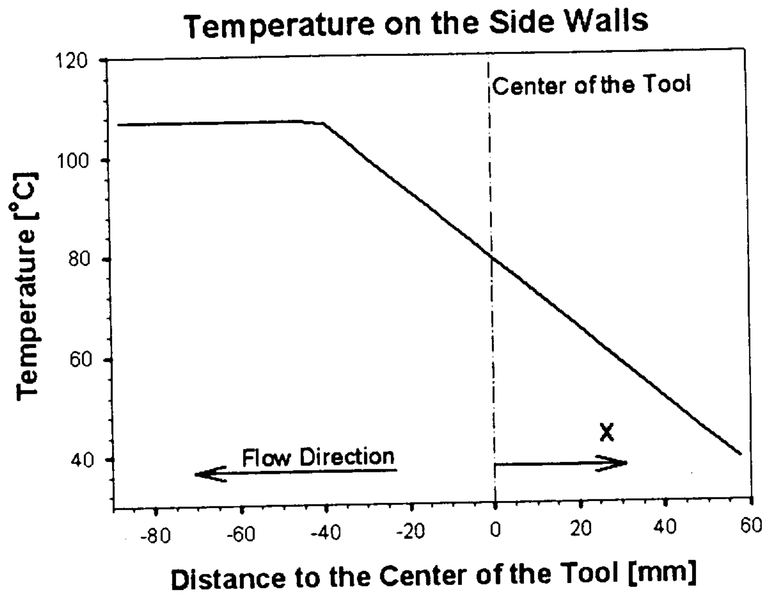

Figure 8-3 The temperature profile was prescibed at the moving walls on advancing and retreating side.

8.4 Results and Discussion of the 3-D Model

The solution method for the 3-D model was the same as for the 2-D model described in Section 7.3. The models were carried out on a 1400 MHz PC. The average computation time was about 40 hours.

Models were solved for two different rotational tool velocities (232 and 390 RPM) holding the welding speed constant at 2.35 mm/s. Additionally, the thermal boundary conditions at the tool and at the bottom surface were varied holding the welding parameters constant at 232 RPM and 2.35 mm/s, respectively.

The experimental data such as torque and tool forces in AA6061-T6 is available for two different FSW types. As described in Section 4.1.2, conventional FS welds were performed with a tilted standard tool, with features that include a threaded pin and a round pin tip. The other weld was a partial penetration weld using a zero-degree tool with a non-threaded, cylindrical pin. The pin tip of this tool was flat. The tool dimensions of the zero-degree tool (shoulder and pin diameter as well as the pin length) were by a factor of 1.25 larger than those of the standard tool.

In the 3-D model, the torque, M, at the tool was calculated as follows:

$$M = \int \tau_w \, r \, dA = h \, r_p^2 \int_{\text{Pin}} \tau_w \, d\varphi + \int_{\text{Shoulder}} 2\pi r^2 \, \tau_w \, dr \tag{8-1}$$

In equation (8-1) τ_w, r, r_p, and h are the wall shear stress, the radius, the pin radius (5 mm), and the height of the flow domain (8.128 mm), respectively. Note that the torque at the pin and shoulder are proportional to hr^2 and r^3, respectively. To account for the larger tool diameters and the longer pin that were used for the zero-degree welds, its welding data was scaled down. The scaling factor of torque, power and weld energy was 0.512 (0.8^3).

The 2-D model and the yet to be presented 3-D model show that the vertical and longitudinal forces at the tool in the 3-D model are mainly due to the pressure force at the shoulder and the pin, respectively. Since the radius and the pin length were 1.25 times larger in the zero-degree weld than in the model, the measured x-force and z-force were scaled down by the factor 0.64 (0.8^2) to compare the zero-degree weld with the3-D model.

Khandkar and Xu [98] measured temperature profiles at various locations in a friction stir weld performed at a rotational velocity of 390 RPM and a welding speed of 2.35 mm/s. The boundary conditions in the models presented in Section 8.4.3 were modified to match the temperature profiles. The material flow in the simulations is discussed and compared with the flow visualization in AA6061-T6 using the marker insert technique, which was presented in Section 5.5.4. It is worth mentioning that experiments cannot be matched exactly with the current 3-D model due to its the simplifying assumptions. For example, the 3-D model uses a non-tilted tool with a non-threaded pin. However, the tool was tilted in welds with the standard tool, which had threads in the pin and the round pin tip. The zero-degree tool had scrolls in the shoulder and was only partially penetrating the weld. Despite all the differences between 3-D model and FSW reality, quantitatively realistic results were expected.

8.4.1 The 3-D Model at 390 RPM

The following model was carried out using the regular mesh (3-D-test-9) as described in Section 8.2. The rotational and the welding speeds were 390 RPM and 2.35 mm/s. The convective heat transfer coefficients at the top and bottom surfaces were 30 and 500 W/(m^2K), respectively. The pin and shoulder were modeled as rotating adiabatic walls. As mentioned in Section 8.3.3, a temperature profile was prescribed at the moving walls on the advancing and the retreating side. The original viscosity function, which drops 3 orders of magnitude within 50 °C above the solidus temperature, was used for the current model.

Case	Torque [Nm]	Energy PUWL [J/mm]	X-Force [N]	Z-Force [N]
Standard FSW	74.81	1292.8	1518.1	22240
Zero-Degree FSW	64.49	1113.3	1831.8	18504
3-D Model	88.77	1616.6	3704	3137
Comparison w/ Standard FSW	119 %	125 %	244 %	14 %
Comparison w/ Zero- Degree FSW	138 %	145 %	253 %	21 %

Table 8-1 Comparison with welding data at 390 RPM and WS=2.35 mm/s. To account for the larger tool of the zero-degree weld, the 3-D the torque and energy PUWL of the model were scaled by a factor of 0.512. X-force and z-force were scaled by the factor 0.64, respectively.

Torque, energy PUWL, and tool forces of the 3-D model are compared to the two different friction stir welds (tilted standard tool and zero degree tool) performed at the same welding velocities (390 RPM and WS=2.35 mm/s). The first weld is a FSW using the standard tool, which was tilted 2.5 degrees to the vertical axis. The second weld is the so-called zero-degree weld described in Section 4.1.2. As mentioned in the previous section, the data of the zero-degree weld is scaled down to compensate for the larger tool diameters and pin length. The welding data of the two welds and the 3-D model predictions are listed in Table C-1. Remember that the vertical tool force, the z-force, was used as a control parameter in the load controlled welds. It is worth mentioning that the torque and the tool forces in the zero-degree weld were larger than in the conventional weld using the standard tool. It is believed that the main difference is due to the different pin designs (non-threaded versus threaded pin).

The torque and the weld energy PUWL of model and FSW compare very well despite the simplifying assumptions of the 3-D model. The model overestimates the torque and power of both welding types. The largest deviation of energy and torque is 25 % for weld performed with the standard tool and 45 % for the zero-degree tool.

The differences between the tool forces are quite significant; however, they were expected due to the different tool design of the 3-D model. The standard FSW tool is tilted against the vertical axis. It is believed the vertical forces on the threads of the standard pin contribute strongly to the overall vertical force. Furthermore, in both welds material is able to pass the tool below the round pin tip. The additional resulting vertical force is not captured in the 3-D model because the cylindrical pin extends throughout the whole flow domain. Hence, with the current 3-D model design it is impossible to match the tool forces. It is worth mentioning that no comparison of the third component of the force vector is possible because no force measurement in transverse direction exists.

The pressure distribution at the tool shoulder is shown in Figure 8-4. Note that the unit of the pressure is Pascal (Pa). A local pressure maximum and minimum occurs on the retreating and on the advancing side of the shoulder, respectively. The force resulting from the pressure distribution below the shoulder points in positive z-direction. Its contribution to the total z-force is almost 100 %.

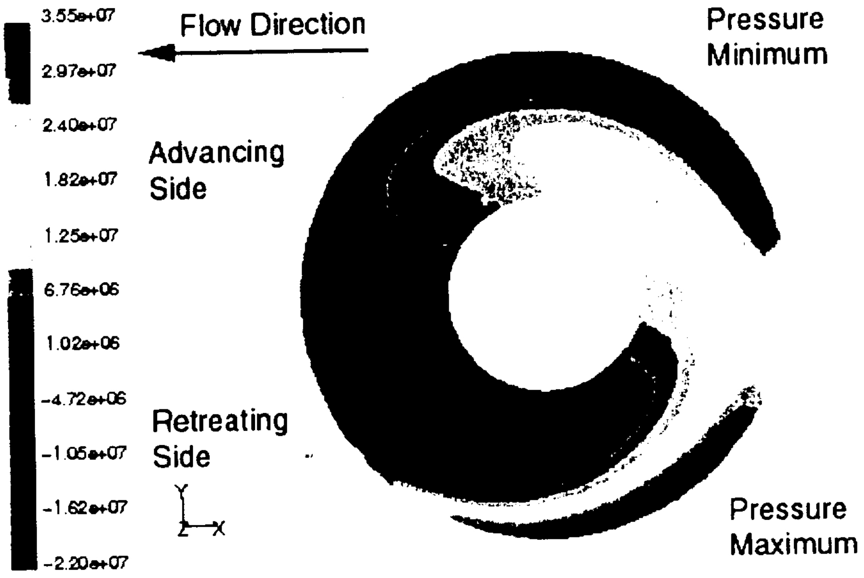

Figure 8-4 Pressure distribution at the shoulder at 390 RPM. A local pressure maximum and minimum exist on advancing and retreating side, respectively. The unit of the pressure is Pascal.

Figure 8-5 shows the pressure distribution at the pin. The global pressure maximum and minimum occur on the leading and trailing edge at the bottom of the pin, respectively. If a similar pressure distribution was present in the zero-degree, partial penetration friction stir weld described above one may assume that a high-pressure region existed below the flat pin. However, this pressure effect is not simulated in the present 3-D model. Furthermore, the scrolls machined in the shoulder surface may contribute additional force components, which are not captured by the 3-D model. The different tool design may cause the large differences of the tool forces.

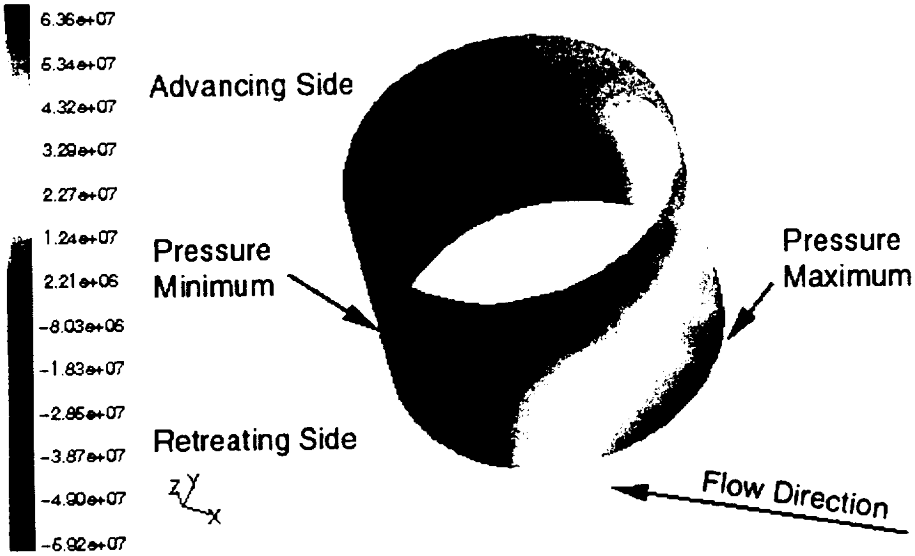

Figure 8-5 Pressure distribution at the pin at 390 RPM. The extreme values of the pressure are the global maximum and minimum, respectively. The unit of the pressure is Pascal.

Figure 8-6 shows predicted temperature profiles in comparison with the temperature measurements by Khandkar and Xu [98]. Both measurements and predicted temperatures are from various locations on the retreating side 2 mm above the bottom surface of the workpiece. In Figure 8-6, y denotes the distance to the weld centerline. The differences between model and measurements decreases with increasing distance from the heat source, which is the deforming material near the tool in transverse and in longitudinal direction. In general, the measured temperatures are higher than predicted. The maximum temperature difference at 8 mm off the centerline (green line) is 116 °C. The thermocouple at the centerline (black solid line) was moved by the tool but not destroyed. Therefore, only the ascending part of the curve (positive distance to the center of the tool) is a meaningful measurement.

The thermocouples (TC) were attached to the aluminum using the high thermal conductivity epoxy Omegabond 101. However, the maximum recommended temperature for this epoxy is 105 °C. Depending on the location of the thermocouple, the maximum allowable temperature of the glue may have been exceeded so that some thermocouples may have lost the contact to the workpiece, i.e. at the locations close to the weld centerline. It cannot be excluded that the thermocouple measurements did not measure the true workpiece temperature due to the inappropriate choice of the thermocouple attachment. Another uncertainty is inherent with thermocouple measurements. Even though thermocouples denote "point" measurements, the temperature is averaged over the area of the thermocouple junction. Therefore, some information is lost if the temperature across the TC junction is not constant, i.e. in regions of high temperature gradients close to the tool.

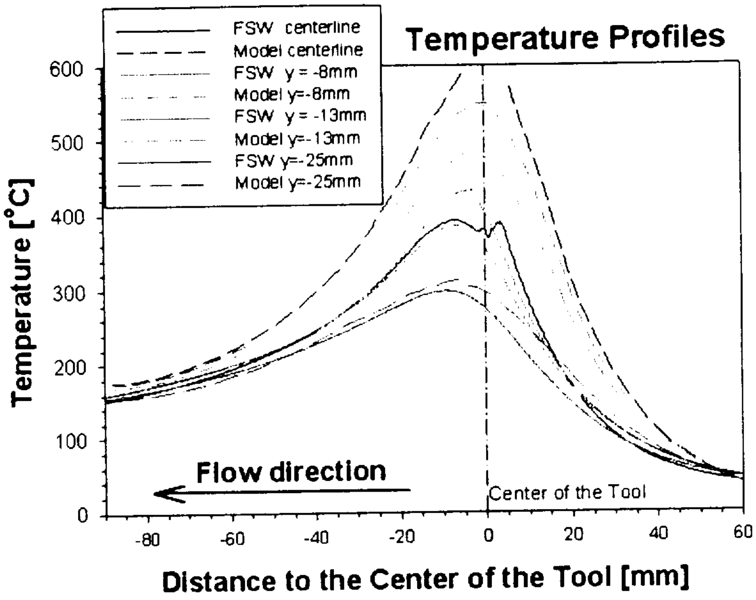

Figure 8-6 Comparison of temperature profiles 2mm above to the bottom surface. Measurements [98] were taken at various locations on the retreating side at 0, 8, 13, and 25 mm to the centerline.

Figure 8-7 shows isotherms at the mid-plane of the weld where the *negative* distance to the tool in welding direction denotes the distance *behind* the tool. It can be seen in Figure 8-7 that the isotherms deviate from the typical and expected egg-shape, i.e. behind the tool indicating measurement errors. If the method of the thermocouple attachment did influence the measured weld temperatures, the actual differences between model and measurement is smaller than indicated in Figure 8-6.

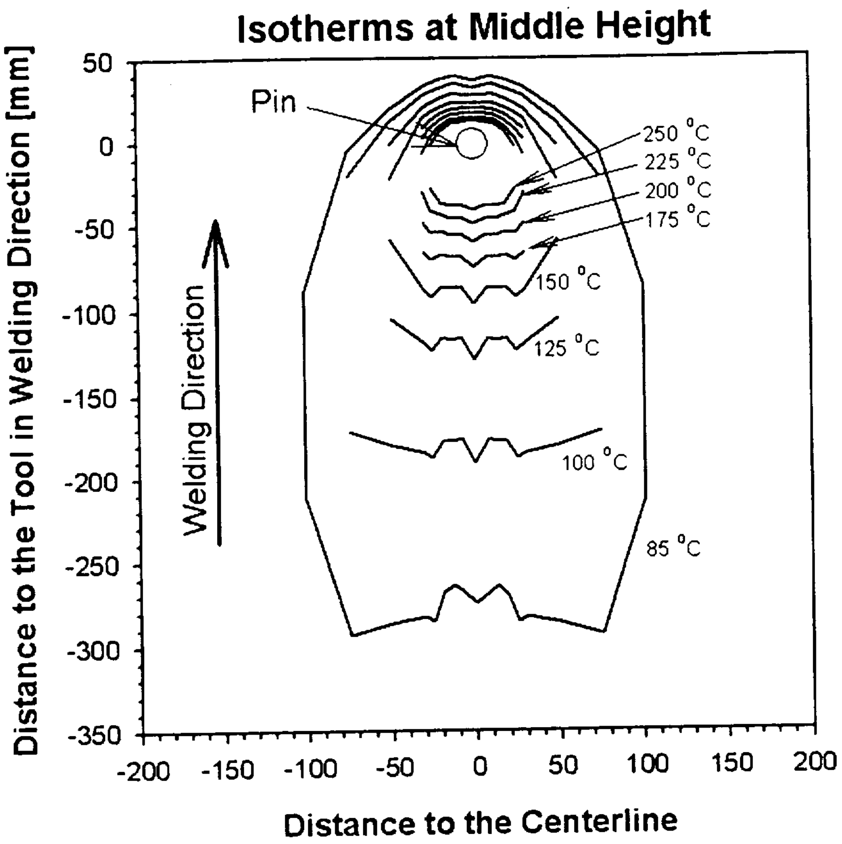

Figure 8-7 Isotherms at the middle height of the weld performed at 390 RPM and 2.35 mm/s [98]. The welding direction is to the top of the page. Advancing and retreating side are on the left and the right side, respectively.

To summarize, the 3-D model at 390 RPM and WS=2.35 mm/s compares well in parts with experimental data. The torque at the tool and the energy PUWL are within 25 % of the measured data. The tool forces are different from the measured forces; the differences can be related to the different tool designs. The differences of the temperature profiles are not too high considering the simplifying thermal boundary conditions at the tool and at the bottom surface. Furthermore, the difficulties of the temperature measurements may have contributed to the lower measured temperatures.

In the following, the material flow in the 3-D flow domain is studied. Figure 8-8 shows pathlines near the pin at three vertical levels (z = 1, 4, and 7.5 mm) for two different views. The left hand side of Figure 8-8 is the projection of the pathlines on the horizontal plane with the flow direction from the right to the left. The right hand side images are perspective views; the observer looks from the advancing side against the flow direction towards the retreating side. As already seen in the 2-D model, all the material within the pin diameter (and more) passes the pin on the retreating side. The pathlines close to the bottom (A and B) and at the mid-plane (C and D) are very similar to those of the 2-D model shown in Figure 7-5. It was shown in Section 5.1 that particles "extruded" around the pin encounter relative displacement to each other such that material within the pin diameter is moved further downstream than material outside the deformed zone flowing at a uniform welding speed. The resulting final relative position of such particles matched the experimentally observed flow pattern almost perfectly as seen in Figure 7-7.

During its way around the clockwise rotating pin, material is lifted on the leading side of the pin and pushed downwards on the trailing side of the pin. However, only little vertical mixing occurs in the 3-D model. Particles are at about the same vertical level before and after passing the pin. The influence of the tool shoulder on the vertical mixing is very small. Figure 8-8 E and F show that close to the tool shoulder material on the advancing side is rotating with the tool before it is released in the flow field.

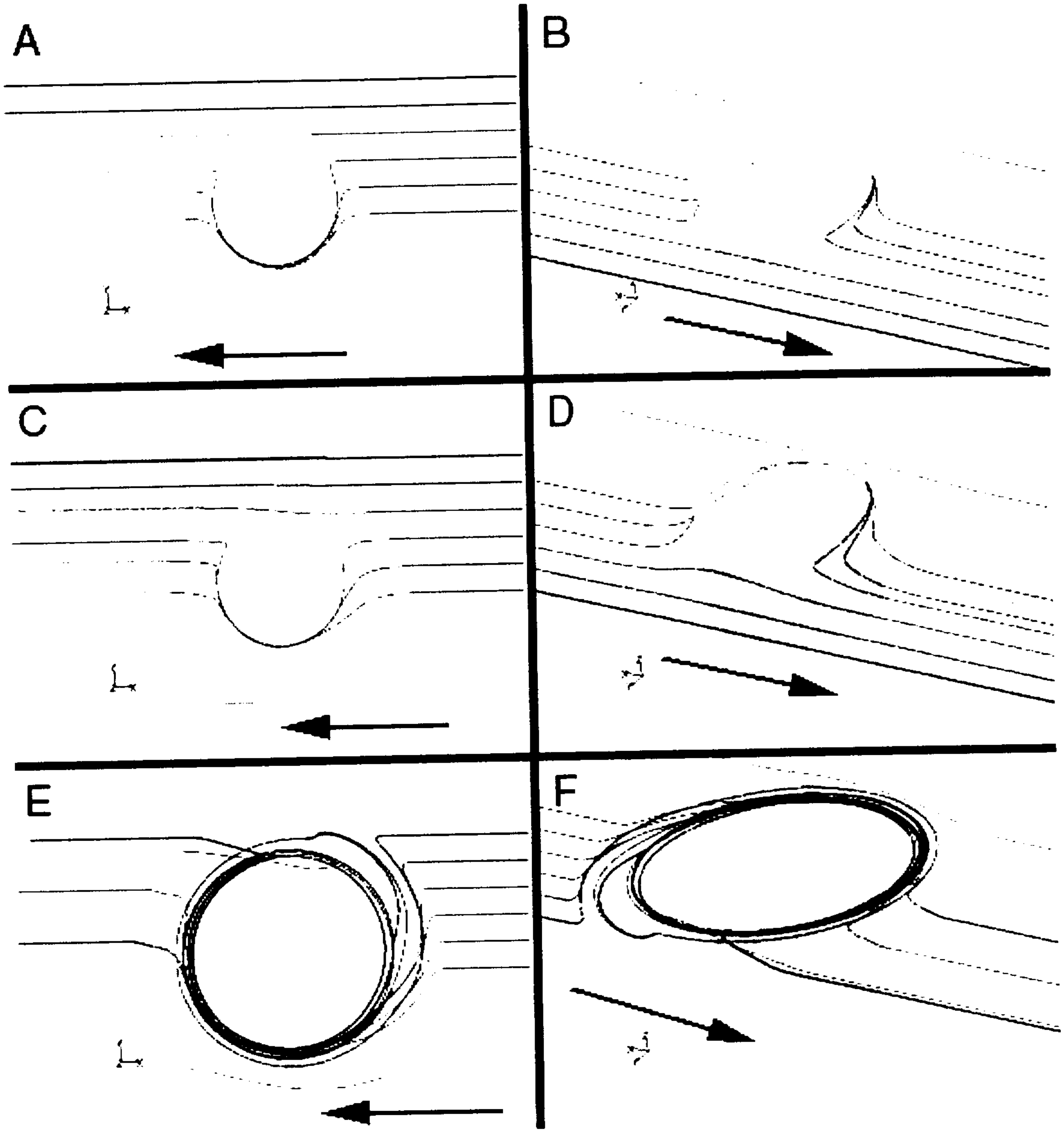

Figure 8-8 Images on the left hand side are the projection of the pathlines on the horizontal plane and images on the right hand side show a perspective view of the pathlines. The tool rotation is clockwise and the arrows indicate the flow direction. Particles are released close to the bottom surface (A and B), at the mid-plane (C and D) and near the top (E and F).

Comparing the pathlines of Figure 8-8 with the vertical flow pattern of the deformed markers of the "nominal" AA6061-T6 weld Figure 5-22 not many similarities can be observed. The flow pattern of the "nominal" weld is mainly characterized by the vertical mixing. Material is pushed upwards outside the "extrusion" zone on advancing and retreating side. Material within the pin diameter is pushed downwards on the advancing side and upwards on the retreating side. The weld was performed with a tilted tool and a threaded pin. The influences of the thread size and of the tilted tool angle were never investigated using the marker insert technique. Therefore, the comparison of the 3-D model with the details of the vertical flow in the "nominal weld is not meaningful.

In Section 5.5.4 the width of the deformed zone was discussed. In the "cold" and "nominal" AA6061 welds, the width of the deformed zone increased nearly linearly from the bottom to the top surface on advancing and retreating side, respectively (Figure 5-23). The width of the deformed zone on the advancing side in AA6061 was different from that of the welds in 2XXX and 7XXX series alloys. Here, the width of the deformed zone was almost constant in the lower two thirds of the weld; it increased only in the top third of the weld height to its maximum, the shoulder radius (Figure 5-25).

Figure 8-9 shows contour plots of the velocity magnitude (A), the strain rate (B), and the viscosity (C) at a plane perpendicular to the flow direction at the center of the tool at x=0 mm. The flow direction is out of the plane; advancing and retreating side are the left and right hand side, respectively. The pin is in the middle of the images and the shoulder at the top. The velocity magnitude (A) is shown at values greater than 3 mm/s, which is arbitrarily chosen. In general, material flowing faster than the welding speed (2.35 mm/s) denotes material deformation near the tool. As seen in Figure 8-9-A, the region of high velocities is much larger on the retreating side than on the advancing side. The line of constant velocity on the retreating side connects the bottom of the pin and the shoulder nearly linearly on the retreating side similar to the increasing width of the deformed zone on the retreating side in the AA6061 friction stir welds. On the advancing side, high velocities are limited to a narrow region near the tool. Here, fluid at velocities larger than 3 mm/s flows in rotation direction of the tool against the overall flow direction. The different velocity profiles on the advancing and the retreating side of the pin are somewhat intuitive knowing the overall flow pattern. All the material within the pin diameter is extruded around the retreating side only. On the other hand, the aluminum alloy (here: the fluid) is incompressible. Therefore, the fluid is accelerated to maintain the fluid flow. The result is the large region of high velocities and velocity gradients (Figure 8-9-B) below the shoulder on the retreating side.

Figure 8-9-B and C are the contour plots of the strain rate and viscosity, respectively. The strain rate and the viscosity are plotted for values greater than 0.5 $^1/s$ and less than $5*10^7$ Pa-s, respectively. Again, the cut-off values are chosen for demonstration purposes. The values are without any physical significance but using them helps to clarify the differences of the flow near the tool on the advancing and the retreating side.

The figures show that the decreasing strain rate causes the "stiffening" of the fluid. We remember that the viscosity is both strain rate and temperature dependent.

However, the temperature distribution on the advancing and the retreating side is very similar as seen in Figure 8-10. The shape of the viscosity (and strain rate) contour plots is very similar to those of the shape of velocity field on the plane at x = 0 mm.

Again, more material is passing the tool on the retreating side than on the advancing side; therefore, the velocities and consequently the velocity gradients (strain rate) extend over a larger volume on the retreating side.

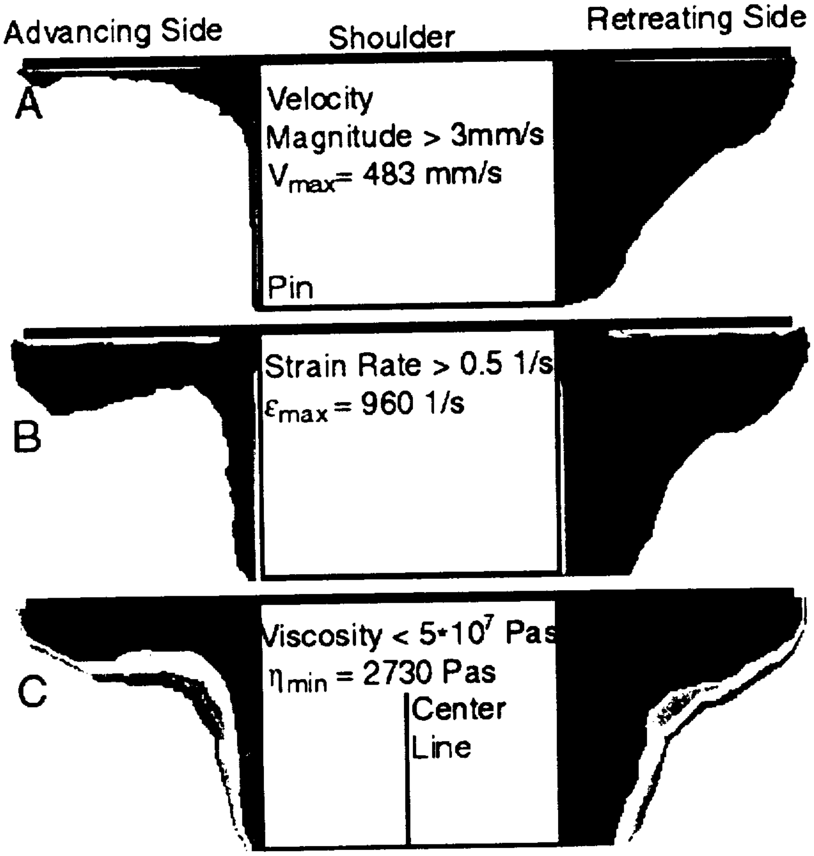

Figure 8-9 Velocity, strain rate, and viscosity contour plots on a plane at the center of the tool perpendicular to the flow direction at 390 RPM and 2.35 mm/s. In the images A, B, and C the minimum and maximum values of the velocity, strain rate and, viscosity correspond to red and blue, respectively.

The temperature distribution at the plane perpendicular to the flow direction at x = 0 mm is shown in Figure 8-10. Note that the maximum temperature (595 °C) is 13 °C above the solidus temperature of AA6061 due to the definition of the viscosity function, which drops 3 orders of magnitude within 50 °C above the solidus temperature. However, the maximum temperature in FSW is always below the solidus temperature; melting never occurs. It is apparent that the temperature range for the viscosity drop is too large and that the onset of the drop occurs too high. Therefore, modifying the viscosity function may improve the temperature distribution quantitatively.

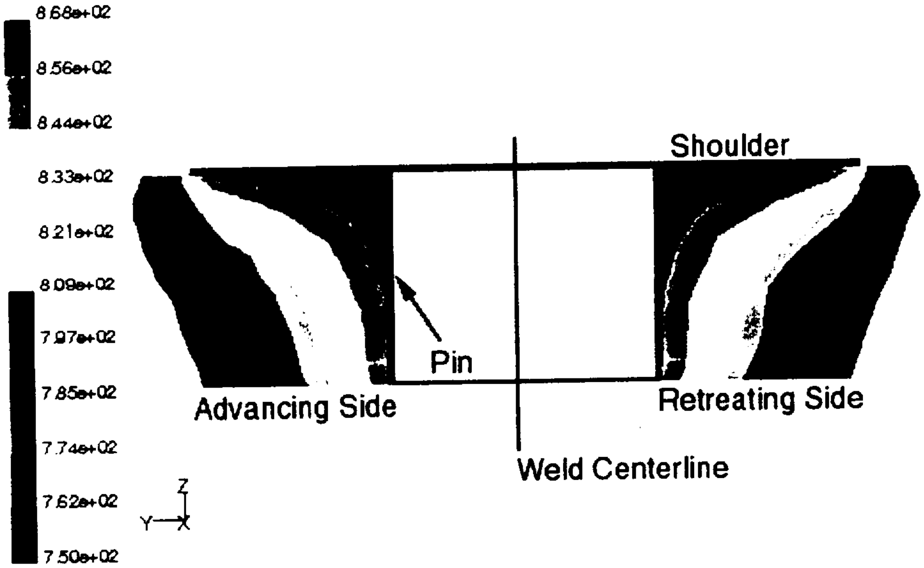

Figure 8-10 Temperatures on the plane at x=0 mm. The distribution is nearly symmetrical to the weld centerline. However, the adancing side is slighty hotter. Note that the legend shows the absolute temperature in Kelvin.

8.4.2 The 3-D model at 232 RPM

The 3-D model presented in this section was carried out at a rotational velocity of 232 RPM and the welding speed 2.35 mm/s. The thermal boundary conditions were the same as in the model at 390 RPM. The convective heat transfer coefficient at the top and bottom of the flow domain were 30 and 500 W/m^2-K, respectively. At the moving walls on advancing and retreating side, the same temperature profile was used as in the previous model (higher RPM) even though the "real" temperature distribution may be lower. However, no experimental temperature data was available at these welding conditions. The tool was modeled as a rotating wall with no heat flux through its surface.

It was shown in the previous section that the original viscosity drop-off[7] might result in unrealistically high fluid temperatures. Therefore, the user-defined function of the viscosity was modified such that the viscosity drops three orders of magnitude within 10 °C at T=577 °C, which is 5 °C below the solidus temperature (T_s=582 °C). It was assured with this modification that the maximum fluid temperature was always less than 582 °C. It is worth mentioning that also a model with the original viscosity function was carried out using the same boundary conditions as the case presented in this section. Due to the modification of the viscosity the changes of power, torque, and

---

[7] The original viscosity drops 3 orders of within 50 °C above the solidus temperature (T_s=582 °C) of AA6061-T6.

tool forces were less than 2 %. The modified viscosity function also did not influence the flow field noticeable. Since the fluid temperature did not exceed the solidus temperature, the results of the model carried out with the modified viscosity are presented in the following.

Welding data at 232 RPM and WS=2.35 mm/s was available for model verification and comparison from the two previously described weld types. Torque, energy PUWL, and forces of the conventional and the zero-degree partial penetration weld are listed in Table 8-2. Note that the welding data of the zero-degree weld is scaled down to account for the different tool sizes. The scaling factors have already been described the beginning of Section 8.4. The 3-D model results are compared to the two welds using the ratio of the predicted to the measured values.

As already seen at the higher rotational velocity, the torque and the energy data compares very well with the two welds. Note that the experimental energy per unit weld length is calculated based on the measured torque data, whereas it is determined from the power balance around the flow domain in the 3-D model. The predicted torque and energy PUWL are within 22% and 48 % of the measured values of the standard and the zero-degree weld, respectively. Note that the model over predicts the torque and the specific weld energy.

Case	Torque [Nm]	Energy PUWL [J/mm]	X-Force [N]	Z-Force [N]
Standard FSW	115.95	1235.01	-3913.9	26688
Scaled Zero-Degree FSW	98.82	1019.3	-2888.2	19927
3-D Model	141.21	1504.5	-1663	955
Comparison w/ Standard FSW	121.5%	121.8 %	45.6 %	3.7 %
Comparison w/ scaled Zero- Degree FSW	142.9 %	147.6 %	57.6 %	4.8 %

Table 8-2 Data comparison at 232 RPM. For the comparison with the data of the zero-degree weld, torque and energy PUWL of the zero-degree weld were scaled by a factor 0.512. X-force and z-force were scaled by the factors 0.64, to account for the different tool sizes.

The force in flow direction (x-force) is under predicted at 232 RPM. The measured longitudinal force was about twice as high as computed. It is important to mention that the predicted forces at 232 RPM are even lower than at 390 RPM. However, the friction stir welds showed the opposite trend.

Figure 8-11 shows the pathlines at 232 RPM near the tool at three different heights (z=1, 4, and 7 mm) from two different views. The left hand images (A, C, and E) are the projections of the pathlines on the horizontal x-y plane. The observer is looking in flow direction from the top of the retreating side in the right hand side images of Figure 8-11 (B, D, and F). The arrow in each image indicates the flow direction. The tool rotation is clockwise. Close to the bottom of the domain at z =

1mm (Figure 8-11A and B), the pathlines look familiar. Material is extruded around the retreating side and no material within the pin diameter passes the tool on the advancing side. The pathlines of particles released at the mid-section of the flow domain are clearly different from what was seen in the simulation at 390 RPM and in the flow visualization experiments. The pathlines at the mid-section on the retreating side are at about same vertical level before and after passing the pin. The material is "regularly" extruded around the tool with the exception that this material is deposited further to the advancing side than it was originally. However, the biggest difference is material flowing near the edge of the pin on the advancing side. The pathlines show that this material is "caught" in the tool rotation. The pathlines wind upwards in spirals around the pin. The spirals start close to the pin and widen on their way to the top. Material is released close to the top in the uniform flow field at about the same position perpendicular to the centerline after moving around the tool seven times.

Particles released close to the top surface (E and F) are passing the pin approximately in 5mm distance to the pin surface on the retreating side. Note that the volume near the pin at the top is occupied by material from lower regions, which is transported towards the shoulder. As Figure 8-12 shows, material passing the tool on the retreating side near the shoulder is pushed downwards to a lower final relative position.

The pathlines shown in Figure 8-11 and Figure 8-12 are unusual because a different material flow was detected in the flow visualization experiments. It is important to remember that the tool design and the tool setup of the 3-D model are different from the friction stir welding reality. The influences of the threaded pin and the tilted tool used in the welds for the marker insert technique were never investigated, but it is believed both have an important contribution to the observed flow pattern. Therefore, the generalization of the results of the marker insert technique is not valid.

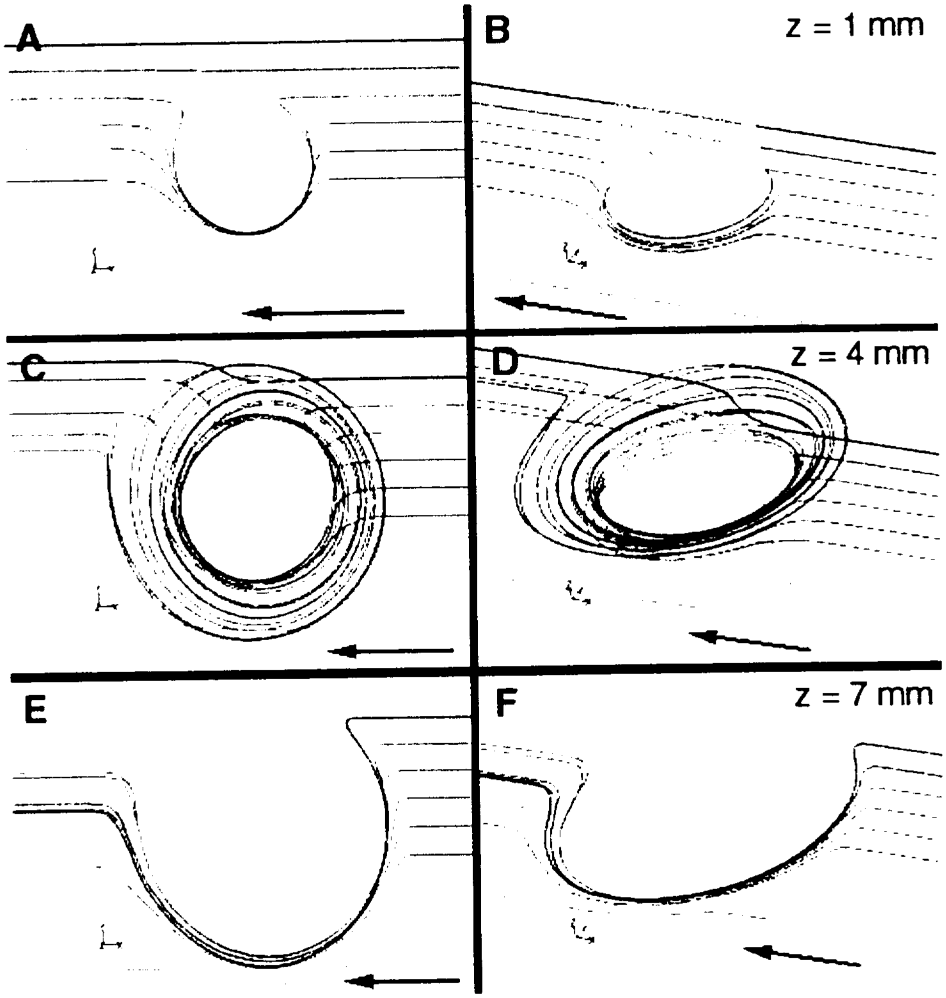

Figure 8-11 Pathlines at 232 RPM. Images on the left hand side are the projection of the pathlines on the horizontal plane and images on the right hand side show a perspective view of the pathlines. The tool rotation is clockwise and the arrows

indicate the flow direction. Particles are released close to the bottom surface (A and B), at the mid-plane (C and D) and near the top (E and F).**

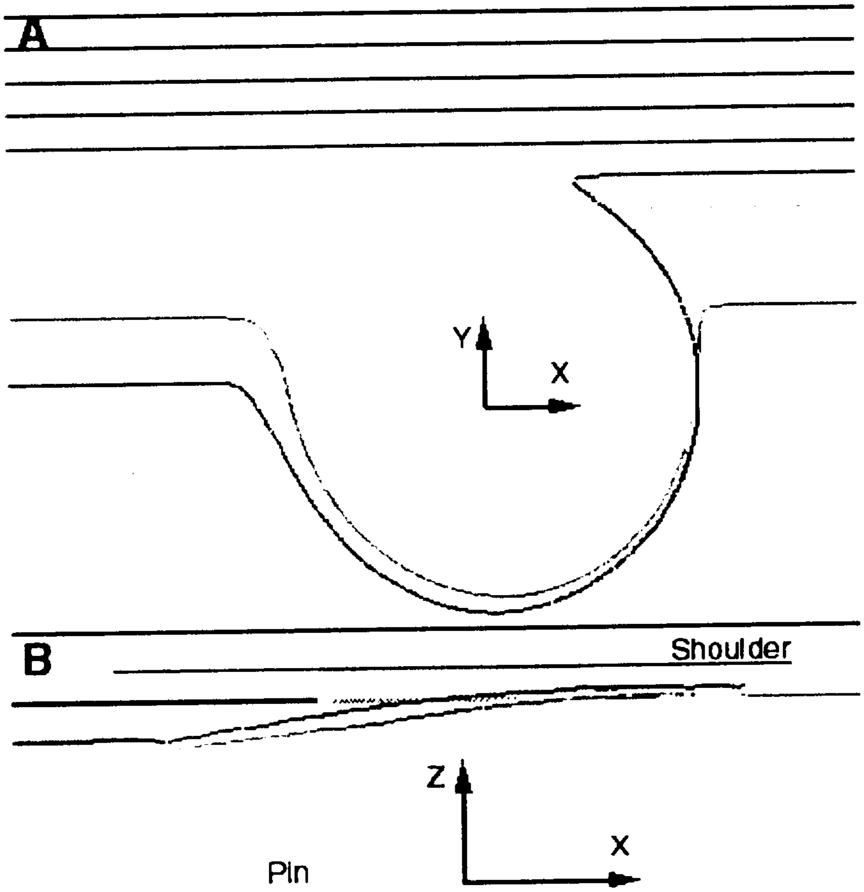

Figure 8-12 Pathlines of particles released near the top (z=7 mm) on the advancing side. (A) is the top view and (B) is a view from the retreating side.

We remember that in the friction stir welds material was moving upwards at the edges of the deformed zone on advancing and retreating side, respectively, which is not seen with the present model. It was already pointed out that the predicted material flow differs from the experimentally observed flow pattern, which shows only the final position of the deformed marker inserts. Assuming that under the given circumstances the model predicts the material flow correctly[8] we can reduce the differences to the different tool designs. One might argue that the material flow in the partial penetration weld using the zero-degree tool should be similar to the 3-D model prediction because of the similarity of the tool. However, it is believed that the scrolls in the shoulder are a significant, flow- influencing feature of the zero-degree tool. The scrolls are formed such that material is transported from the outer shoulder radius towards the center of the tool. In the 3-D model, however, material is transported towards the outer radius of the shoulder near the top of the domain as seen in Figure 8-11 C-F and in Figure 8-12.

To summarize, the material flow at 232 RPM is different than at 390 RPM. At 390 RPM, the vertical material flow is minimal. Material is extruded around the pin throughout the total height of the flow domain. At 232 RPM the material flow is similar in the lower half of the flow domain. Particles released at middle heights on advancing side of the tool are rotating with the tool. The pathlines wind in spirals towards the shoulder. Thereby, the radius of the spirals grows before the material flowing along those pathlines is released in the uniform flow field.

---

[8] The prediction of the correct torque and power in 3-D data in addition to the 2-D model simulation are reasons to justify the assumption.

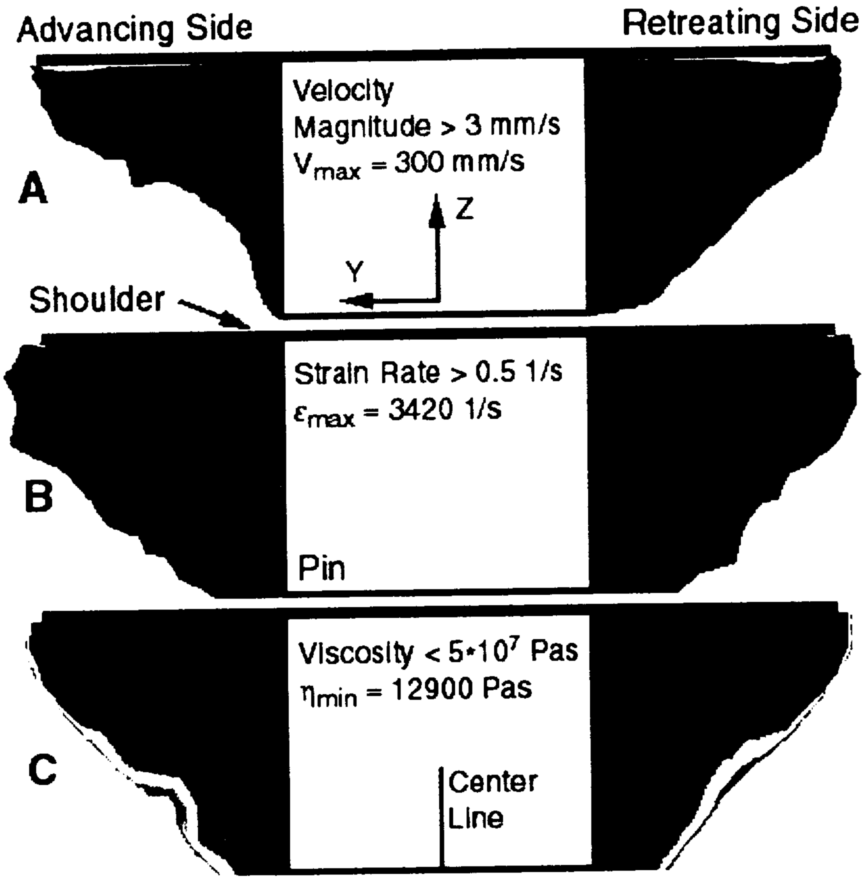

Figure 8-13 Velocity, strain rate, and viscosity contour plots on a plane at the center of the tool perpendicular to the flow direction at 232 RPM and 2.35 mm/s. The blue red contour colors correspond to minimum and maximum values of the velocity, strain rate, and viscosity, respectively.

In the following, the material deformation in the transverse direction is investigated. Figure 8-13 shows the velocity magnitude (A), the strain rate (B), and the viscosity (C) on the plane perpendicular to the welding direction at the center of the tool. Note that the contour colors red and blue correspond to the maximum and minimum values, respectively. For demonstration purposes the same cut-off values for the velocity, strain rate and viscosity were used as in Figure 8-9 at 390 RPM. The difference between the two rotational velocities is that the width of the deformed zone[9] on the advancing side is larger at 232 RPM than at 390 RPM. It increases almost linearly in transverse direction from the bottom of the pin to the shoulder. The deformed zone is nearly symmetrical to the centerline.

The deformation of the "fluid" in the transverse direction at the two rotational velocities is very similar to the width of the deformed zone in AA6061 observed with the marker insert technique as shown in Figure 5-23. Note that the transition to the common shape[10] of the width of the deformed zone was seen at different welding conditions (832 RPM and WS=1.28 mm/s) in the friction stir welds. However, the 3D-model also predicts less material deformation on the advancing side at the higher rotational velocity. It is important to remember that the large width of the deformed zone on the advancing side was seen only in the "cold" and "nominal" welding conditions in AA6061. In the alloys of the 2XXX and 7XXX series the volume of deformed material on the advancing side was much smaller than on the retreating side at all welding conditions (Figure 5-25). The differently deformed volume of material on the advancing side in AA6061 at different welding conditions may have been caused by the difference of the material properties of AA6061 since all the welds were performed using identical setups. The thermal conductivity and the solidus

---

[9] Note that the width of the deformed zone is displayed only qualitatively.

[10] All the welds in the 2XXX and 7XXX series aluminum alloys had a *common* shape of the deformed zone in transverse direction. On the advancing side less material was deformed than on the retreating side.

temperature of AA6061 are significantly higher and the flow stress of AA6061 is lower than that of the aluminum alloys of the 2XXX and 7XXX series.

Two questions asked in Section 5.5.4 remain to be answered. Why is the shape of the deformed markers in AA6061 different than in welds of the 2XXX and 7XXX series? Moreover: Why is the shape in "hot" welding conditions different from that at "colder" welding conditions?

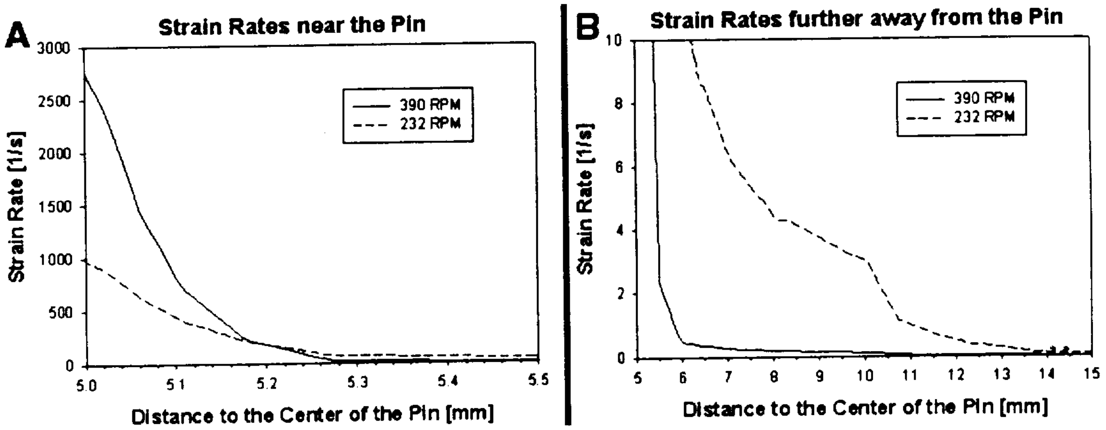

Figure 8-14 Strain rates on the advancing side in transverse direction at mid-height.

Let us find a possible answer to the second question first. Close to the pin, the strain rate and the strain rate gradient on the advancing side in transverse direction are *higher* at 390 RPM than at 232 RPM as seen in Figure 8-14-A. However, at a certain distance to the pin, the strain rates at 390 RPM are *lower* than at 232 RPM as seen in Figure 8-14-B. The same strain rate distribution on the advancing side is also shown in Figure 8-9 and Figure 8-13. Remember that the fluid is less viscous at high strain rates. As a consequence of the strain rate distribution, the plastic deformation at 390 RPM is constrained to a narrow region on the advancing side near the tool. However, the plastic deformation near the tool is larger at high RPM than at low RPM because the strain rates are higher near the tool. At low rotational velocities, more material is deformed on the advancing side because the viscosity is lower than at 390 RPM in a certain distance to the tool. In Figure 8-14-A the strain rates of the cases at 232 RPM and 390 RPM are equal at distance of 0.2 mm from the surface of the tool. The material flow along the pathlines "climbing" in spirals around the tool at 232 RPM is accompanied by the lower strain rate gradients near the tool and higher strain rates after a certain distance in transverse direction.

The current 3-D modeling results cannot give answers the first question because only AA6061 was simulated. Further investigations are necessary to reveal if, for example, AA2024 shows a different material flow behavior. Additionally, changing single material properties sequentially, as done in the 2-D model with the artificial materials (Section 7.4.6), may clarify what material properties or combination thereof may cause the different flow pattern seen in AA6061.

In the following the thermal boundary conditions at the tool were changed to gather information about the influence on the fluid temperature and the model performance.

8.4.3 Convective Heat Transfer at the Tool

Three models with varying convective heat transfer coefficient were carried out in the mesh configuration '3D-test-8-2', which is the large flow domain with the coarse mesh. The reason for using the coarse meshes was simply to save computation tine because the two coarse meshes contained only about half of the elements of the fine mesh (3D-test-9). The material properties of AA6061 were applied in the present investigation using the modified[11] viscosity function of AA6061. All models presented in this section were calculated at the same rotational velocity of 232 RPM and the same welding speed of 2.35 mm/s.

The common boundary conditions of the three models were as follows: A temperature profile was prescribed at the moving walls on advancing and retreating side. A similar same profile as discussed in the previous models was used. Due to the larger dimensions of the flow domain in y-direction, the temperature increased from 27 °C at the inlet to a maximum temperature of 82 °C 5 mm behind the center of the tool (at x=-5 mm and y = ±100 mm).

Convective heat transfer was assumed at the bottom and the top surface with heat transfer coefficients of 500 and 30 W/m^2-K, respectively. Three different heat transfer coefficients were used at the tool (pin and shoulder). The heat transfer

---

[11] The viscosity drop occurs in a smaller temperature range and at a lower temperature.

coefficients were guessed because no correlation of the Nusselt number[12] as a function of the Reynolds and Prandtl[13] number was found, which describes the current problem. The first model was carried out with the adiabatic tool. For the second model the heat transfer coefficient was guessed at 3000 W/m^2-K. By judging the temperature profile of that case, it was decided to increase the coefficient to 6000 W/m^2-K in the third case.

It is important to mention that the *solution* of the governing equations was not stable for the model including heat transfer at the tool. The reason was the poorly solved pressure distribution[14] in the flow field. It was already mentioned in the 2-D model that the pressure distribution was the most difficult part of the solution using the CFD software FLUENT. It is not believed that the coarser mesh contributed to the instabilities because the model without heat transfer at the tool converged perfectly.

As a consequence of the poorly solved pressure field, the forces acting on the tool were not solved correctly. However, the comparison with the model using the fine mesh makes us believe that the heat generated due to viscous dissipation and the temperature distribution were solved correctly.

---

[12] The mean Nusselt number N_m is defined as $Nu_m = \frac{hL}{k} = \frac{q''L}{k(T_w - T_\infty)}$, where h is the heat transfer coefficient, q" is the wall heat flux, L a representative length, k the thermal conductivity of the fluid, and T_w and T_∞ are the wall and the free stream temperature, respectively.

[13] The Prandtl number is defined as $Pr = \frac{\eta c_p}{k}$.

[14] For example, no distinct pressure minima or maxima exist at the tool. The pressure distribution is diffuse on the tool surface.

Case	h(tool) [W/m^2-K]	Power [W]	Torque [Nm]	Heat Transfer Rate at Tool [W]	X-Force [N]	Z-Force [N]
1	0	3458	136	0	1812	944
2	3000	4448	178	1057	~~976~~	~~689~~
3	6000	4987	201	1910	~~1153~~	~~958~~

Table 8-3 3-D model data at varying heat transfer coefficients at the tool.

The welding data of the three models is listed in Table 8-3. Note that the forces of Case 2 and 3 are not used for comparison because it is known that the solution of the pressure distribution was not stable.

As seen in Table 8-3, increasing the heat transfer coefficient at the tool increased the heat transfer through the tool boundary. Moreover, power and torque increased with increasing heat transfer at the tool. It is worth mentioning that the lowest torque (in the case without heat transfer to the tool) is already higher than measured (compare with Table 8-2). The temperature profiles at a line in longitudinal direction 8 mm off the centerline at middle height on the retreating side (y=-8 mm and z=4 mm) are shown in Figure 8-15. Note that the location of the selected line is close to the pin diameter on the retreating side. In addition to the model temperatures, the measured temperatures [98] along this line are plotted in the same graph although the friction stir weld was performed at a higher rotational velocity (390 RPM instead of 232 RPM). Remember that the measured temperatures at the weld may not reflect the actual weld temperature due to the inadequate choice of the thermocouple mounting.

Figure 8-15 shows that increasing the heat transfer coefficient at the tool decreases the fluid temperature. The model with the highest heat transfer coefficient yielded the lowest and possibly the most realistic temperature profile.

To conclude, modeling heat transfer at the tool decreases the fluid temperatures. It was seen in Section 8.4.1 that the measured temperatures were lower than predicted with a model using an adiabatic tool. The presented models suggest that a 3-D model including heat transfer at the tool may result in more realistic temperature profiles. Note that the accuracy of the measurement seems questionable as discussed in Section 8.4.1 and that the model in this section are presented with the reservation that the incorrectly solved pressure profile did not influence the heat generation, which is due to viscous dissipation. Further studies are necessary to investigate the solution instabilities and to determine the influence of the convection at the tool on the tool forces.

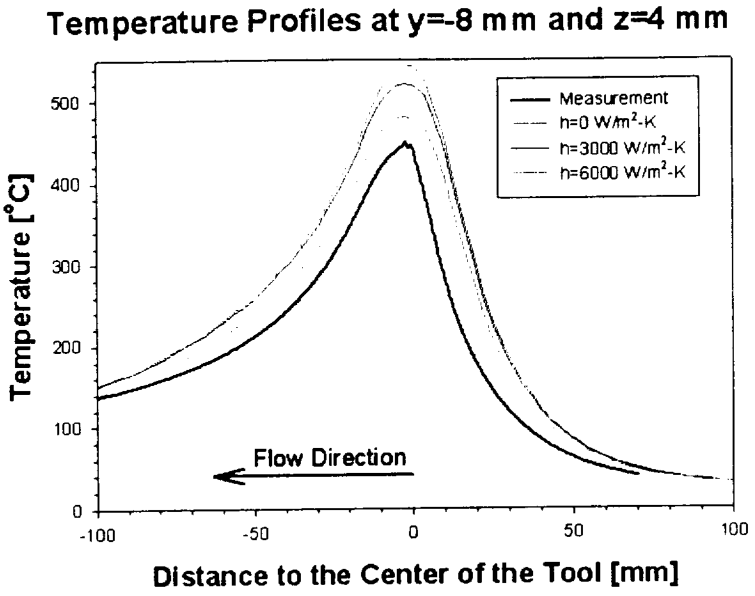

Figure 8-15 Temperature profiles of the cases, 1, 2, and 3 (Table 8-3) on the retreating side at middle height in longitudinal direction. In addition, the measured temperatures at 390 RPM at the corresponding location are plotted for comparison.

8.5 Summary and Conclusions of the 3-D Model

A three-dimensional FSW process model based on fluid mechanics has been presented in this chapter. The model is thermo-mechanically fully coupled. In the 3-D model, the tool consists of a cylindrical pin with a smooth surface and a flat shoulder. The shoulder is at the same height as the top surface of the domain. The flow domain is surrounded by moving walls, a flow inlet, and an outlet.

Convective heat transfer is assumed at the bottom and top surface domain. At the top surface, the convective heat transfer coefficient is that for aluminum and air. At the bottom surface, the contact area with the steel backing plate, a uniform heat transfer coefficient is used similar to the work of Chao et al. [100]. The welding speed and the rotational speed are used as kinematic inputs at the flow inlet and outlet as well as at the moving walls.

Models were carried out at two different rotational tool velocities (232 RPM and 390 RPM). The torque at the tool as well as the power generated in the model due to viscous dissipation compare very well with experimental data, which was measured with the FSW-PDS at the same welding conditions. The models over predict the measured values. However, the models and experiments show the same trend at increasing the rotational tool velocity, which is an decreasing torque and increasing power of the weld, respectively.

The simplifications of the tool, result in forces on the tool inconsistent with the measured data. The standard tool used in the welds consisted of a threaded pin with a round pin tip and a non-flat shoulder. This tool was tilted 2.5° against the vertical axis during welding. Additional welds were performed with a so-called zero-degree tool. The zero-degree tool consisted of a cylindrical pin and a shoulder with scrolls. Both tools are believed to have significant influence on the tool forces and on the material flow. The longitudinal and vertical force of the model do not compare very well with the measurements. Increasing the rotational speed increased the tool forces in the model. However, the opposite trend is observed in most friction stir welds[15]. It is worth mentioning that the 2-D model predicted the correct trend of the x-force. We believe that the different tool design of the current 3-D model is mainly responsible for the differences of the forces. As discussed above the FSW tools had features influencing the material flow such as threads, tool-to-workpiece-normal angle, or scrolls in the shoulder.

The predicted material flow agrees in parts with the observed flow pattern visualized with the marker insert technique. For example, the models show that no material within the pin diameter is passing the tool on the advancing side. It was shown with the 2-D model for so-called "cold" welding condition (producing little vertical mixing in friction stir welds) that only extrusion around the retreating side explains the observed flow pattern. Furthermore, the 3-D model predicts different varying volumes of deformed material on the advancing side at the 232 and 390 RPM. The deformed zone on the advancing side is smaller at the higher rotational velocity. Although detected at even higher RPM, the marker insert technique revealed the same phenomenon in AA6061-T6. It is important to mention that the deformed zone on the advancing side was small in the aluminum alloys of the 2XXX and 7XXX series at all welding conditions. So far, no reasonable explanation has been found for the different flow characteristics of AA6061. However, it is obvious that the different material

---

[15] In some welds performed in AAXXXX at USC the x-force decreased to almost zero at decreasing the rotational velocity.

properties of AA6061[16] caused the differences because all welds were performed with the identical tool using the same weld setup.

The material in the 3-D model shows almost no vertical mixing at high RPM. Material is extruded around the retreating side throughout the total height of the flow domain except for a narrow region close to the tool shoulder. The material flow due to the shoulder rotation has only little effect on the flow field in lower regions. The material deformation is constrained to a narrow volume around the tool at 390 RPM. At the lower rotational velocity, the pathlines show a different material flow in the upper half of the flow domain. Starting at about the mid-plane, material from the edge of the advancing side is rotating in spirals with the tool towards the top of the domain. This motion pushes other material in transverse direction causing a larger volume to deform on the advancing side.

It is known from the marker insert technique that material was pushed towards the root of the weld on the advancing side within the extrusion zone. Outside the extrusion zone and on the retreating side, material was pushed towards the root of the weld. Note the difference between the experiments and the current 3-D model. The features on the FSW tool such as the threads and the tool-to-workpiece-normal angle enhance the downward motion. The threads are formed such that material is transported downwards. Furthermore, the trailing side of the shoulder pushes material

---

[16] The flow stress of AA6061 is lower than that of the alloys of the 2XXX and 3XXX series. Furthermore, the thermal conductivity and the solidus temperature are significantly higher than in the other alloys.

towards the root due to the tilted tool. Both effects are counteracting against the observed material flow in the 3-D model. Hence, it seems obvious that the 3-D model with the current tool design is not capable of predicting the material flow that was observed in the welds visualized with the marker insert technique.

Additional models were carried out in a larger flow domain with a coarser mesh using varying heat transfer coefficients at the tool. It is important to mention that the pressure field of the models with heat transfer to the tool was not solved correctly. Nevertheless, it is believed that the generated heat and the temperature field were solved correctly. The temperature field near the tool was possibly more realistic because increasing the heat transfer to the tool results in lower temperatures. With increasing heat transfer coefficient more heat was generated in the fluid.

9 Summary and Recommendations

9.1 Summary

An extensive analysis of the material flow in friction stir welds has been performed in this dissertation. This work includes the experimental and numerical analysis of the material flow.

A marker insert technique has been developed to visualize the material transport during welding. The post welding method provides insight in the deformed weld zone by visually reconstructing a 3-D image of the deformed marker inserts. Seven different high strength aluminum alloys have been friction stir welded with varying welding parameters such as welding speed and rotational tool velocity. Additionally, different tools have been used to weld the alloy AA2195.

All welds regardless of the base material, welding parameter or, tool, had a basic flow pattern in common. The material transport in FSW, which is the result of the two tool motions – translation and rotation – can be roughly described as the superposition of the material extrusion around the tool, a clockwise rotation around the longitudinal axis within the extrusion zone, and the material transport towards the crown of the weld outside the extrusion zone. Different mechanisms cause the vertical mixing of the material. First, the rotating shoulder transports material originally from the retreating to the advancing side. Therefore, the material originally occupying the volume on the advancing side is pushed downwards in the weld causing material at lower levels to move in transverse direction towards the top of the weld. The tilted tool may enhance the shoulder effect because the trailing side of the shoulder, which is below is below the weld surface, is pushing material downwards. The material transport due to the threads on the pin is another mechanism contributing to the vertical material transport. The tool rotation direction is such that the threads push material downwards.

The material flow patterns in the aluminum alloys of the 2XXX and 7XXX series are fairly similar in all three welding conditions, which have been categorized as "cold", "nominal" and, "hot" based on the specific weld energy. The differences between the different alloys may be explained with the different material properties such as flow stress and thermal conductivity.

The material flow pattern in the AA6061 welds is clearly different from that of the alloys of the 2XXX and 7XXX series. In particular, the shape of the deformed zone in the "cold" and "nominal" welding configuration is different because a larger volume of material on the advancing side is deformed. The "hot" welding condition in AA6061 revealed a similar flow pattern as the other alloys.

The tool-to-workpiece-normal angle and the thread size were the same in all welds analyzed with the marker insert technique. Therefore, the exact influence of these parameters is not known. It must be stated that material flow in FSW depends on the exact tool geometry and the welding parameters used; therefore the generality of any of the above conclusions about the material flow has not been established.

The material flow in FSW was also investigated numerically. A process model based on fluid mechanics has been developed. The aluminum alloys are treated as fluids considering only ideal plastic deformation and neglecting the elastic properties as well as strain hardening. The viscosity is based on a constitutive law of the flow stress using the Zener-Hollomon parameter. The model couples the thermal plastic flow such that the solution of the temperature is obtained simultaneously with that of the velocity field. The heat necessary for the thermal softening of the material is generated due to the viscous dissipation. A non-slip velocity condition is assumed at the tool surface. Furthermore, the process model considers only the steady state part of friction stir welding.

As a first step, a two-dimensional model has been developed by considering only a mid-section of a "cold" friction stir weld, which produces only little vertical mixing. This model was used to establish appropriate boundary conditions and to perform parametric studies of the welding parameters and the material properties. The predicted material flow pattern of AA6061 matched the experimentally observed pattern of the deformed markers at the "cold" welding condition. The same trends of measured tool forces, torque, power, and specific weld energy were predicted with the 2-D model.

The 2-D model was carried out over a wide range of welding parameters. The 2-D model shows the existence of a plug rotating with the pin, which has also been reported by other researchers ([55] and [63]). The plug size changes with changing welding parameters. It has been found that flow of material within the pin diameter only around the retreating side of the tool occurs only in a certain rage of the welding conditions. At a given welding speed at low and at high rotational pin velocities, the material within the pin diameter also flows around the advancing side of the pin. It is believed that the flow around the advancing side explains some typical friction stir welding defects. Holes in the weld may develop in the lower part of the advancing side if the material transport around the retreating side is insufficient. The flow of material around the advancing side as predicted by the 2-D model is a plausible explanation for the occurrence of these defects.

A three-dimensional process model has been developed to simulate FSW more realistically. The presented 3-D model includes a tool, which consists of a smooth, cylindrical pin with a flat shoulder on top of the flow domain. The main focus in the development of the 3-D model has been on the determination of the thermal boundary conditions. Convective heat transfer is assumed at the top and bottom surface of the flow domain using uniform heat transfer coefficients, respectively. The temperatures on the sidewalls of the flow domain on advancing and retreating side are prescribed using experimentally determined temperature profiles.

3-D models were carried out at two rotational tool velocities. The model over predicted the fluid temperature when compared to measured temperature profiles. However, it is believed that the choice of the thermocouple mounting used in the experiments [98] was inappropriate (i.e. the epoxy) resulting in lower temperatures than the actual welding temperature. The 3-D model compares well with measured welding data such as torque and power. The predicted values are within 20 to 50% of the actual weld data. Moreover, increasing the RPM increased torque and power in both, FSW and 3-D model. However, the tool forces, in particular the vertical axis force, are clearly different. The calculated tool forces increase whereas the measure forces decrease with increasing RPM. The reasons for the supposedly incorrect prediction of the tool forces are inherent in the simplified FSW tool used in the 3-D model. The tool neglects the tool-to-workpiece-normal angle, a threaded pin, the pin clearance, and details at the shoulder to name only some simplification. All of the above tool details are believed to contribute significantly to the tool forces. Hence, the current 3-D model is not capable of simulating the tool forces occurring with a different tool design than used in the model.

As a further consequence, the material flow coincides with the visualized flow pattern using the marker insert technique only in parts. For example, the model shows that material within the pin diameter is passing the tool solely on the retreating side. Furthermore, the model also predicts the "abnormality" of the shape of the deformed zone of AA6061 seen with the marker insert technique. However, the model does not show the vertical mixing of material during FSW as described with the marker insert technique. The tool of the 3-D model does not include the tool features that are believed to cause the typical material flow pattern in the FSW visualized in the present research project.

Models and experiments have been very useful to gather information about the FSW process. For example, the flow patterns visualized experimentally have been helpful to characterize the influence of the welding parameters and tool diameters in terms of the horizontal and vertical material flow. Furthermore, the flow visualization has shown similarities and differences between welds of different base materials. However, the marker insert technique does not reconstruct the actual flow path of the material to its final position. For example, knowing only the final shape of the distorted zone, flow around the advancing and retreating side is also conceivable. However, the 2-D and 3-D process models leave no doubt that only the flow around the retreating side explains the observed flow patterns. Furthermore, a possible defect mechanism is suggested based on the results of the 2-D model. Although it is believed that the 3-D model describes correctly the material flow using the given simplified tool, it cannot predict the complicated material flow produced in welds using a tool design with details enhancing the material flow.

9.2 Recommendations

The current 3-D model uses a zero-degree tool. However, so far, no investigations have been conducted towards zero-degree welds using the marker insert technique. It would be useful to study experimentally the differences between threaded and non-threaded zero-degree welds at different welding conditions.

For future comparisons and validations the experimental welding data could be acquired more reliable and consistently. For example averaging the data of several welds performed at the same welding conditions may compensate for uncertainties of the force and torque measurements.

It was already pointed out that reliable temperature measurements are necessary for the "fine tuning" of the boundary conditions. It is suggested to use a thermally highly conductive cement to "glue" the thermocouples to the base material. Furthermore, temperature measurements at different welding conditions or different base materials would be helpful for future model verifications.

As shown in the previous chapter, the boundary conditions, i.e. the thermal boundary conditions, in the 3-D model are not known a priori. However, the quality of the model depends on the proper choice of the boundary conditions because of the coupled, partial differential governing equations and the use of the temperature dependent material properties.

Further optimizations of the boundary condition at the contact to the backing plate may be achieved by adjusting the uniform heat transfer coefficient to better match experimental temperature data. Additionally, the use of a non-uniform heat transfer coefficients at the bottom surface, which could be a function of the distance to the center of the tool, may compensate the non-uniform contact conditions at the bottom surface due to the high pressure below the tool. However, the key to optimized thermal boundary conditions is reliable and trustworthy experimental temperature data.

The simulation of different materials may help to understand the different flow characteristics seen with the marker insert technique. The 3-D model can be used to simulate artificial and/or other real materials to gain information about the influence of single material properties or combinations thereof.

For future modeling efforts, it is suggested to model zero-degree tools because the future tool development in FSW will most likely focus on zero-degree tools. With tool details added to the current simplified tool the material flow may be predicted more realistically. Adding for example concentric fins at the pin or the shoulder may approximate threads at the pin or scrolls at the shoulder, respectively, without changing the solution technique. By modifying the tool shoulder one may prevent the material movement towards the outer shoulder radius, as seen in the simulation of AA6601 at low RPM. This might affect the flow pattern in lower levels as well.

Another case to be studied could be a two-shouldered, self-retracting FSW tool. The benefit of such a model would be the simplification of the thermal boundary conditions since no backing plate is used in such welds. However, no experimental welding data of a two-shouldered tool is available, yet.

Appendix A: Vertical Flow in AA2219 and AA7075

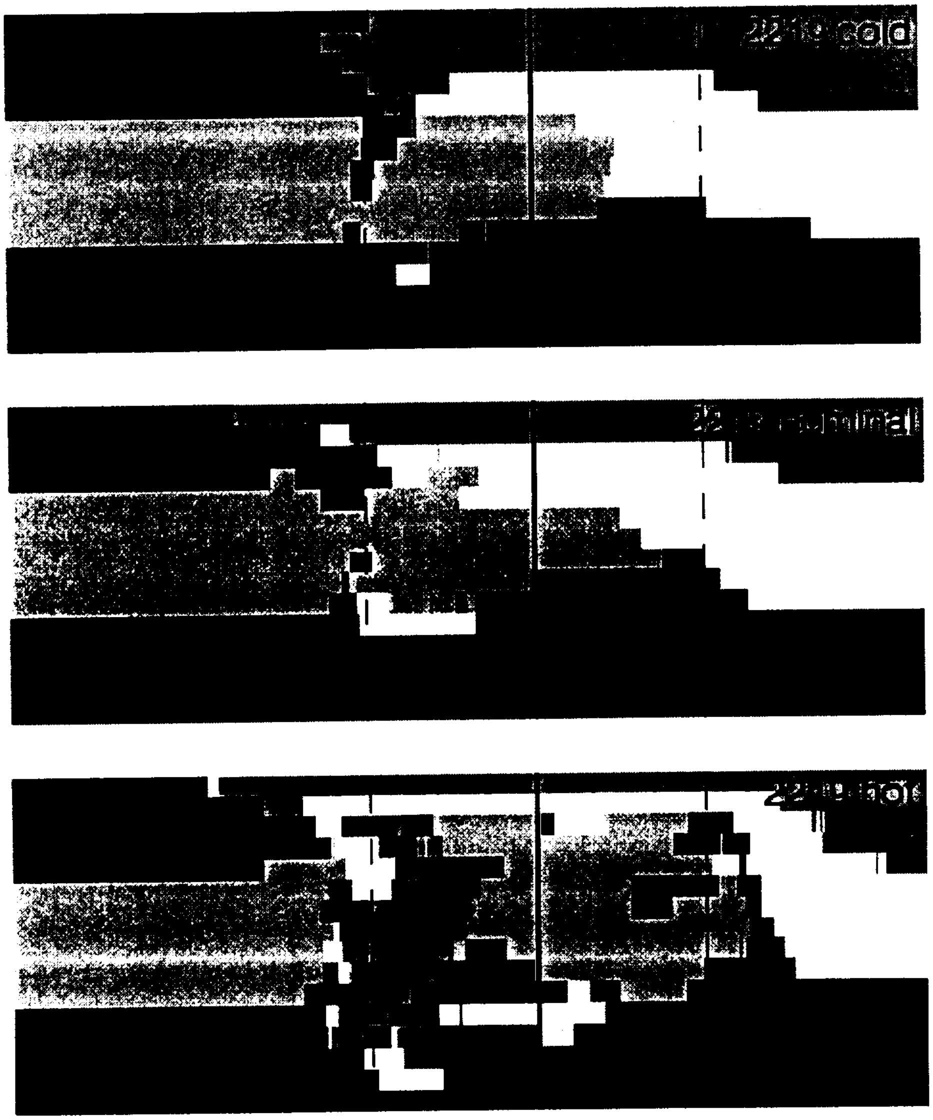

Figure A 1 Vertical flow in AA2219 for the welding conditions "cold", nominal", and "hot".

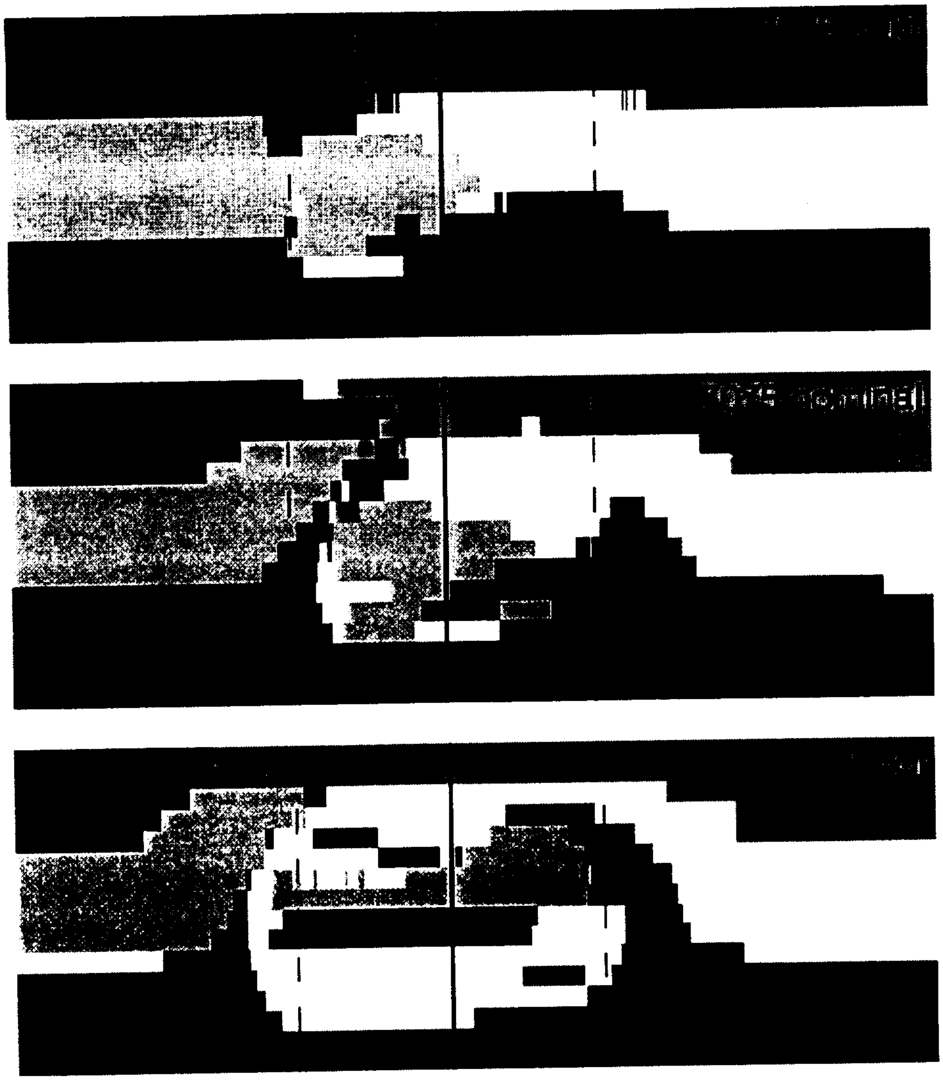

Figure A 2 Vertical flow in AA7075.

Appendix B: The User Defined Function

AA6061

In the following, the user-defined function (UDF) for the viscosity of AA6061 is shown. The viscosity based on the constitutive law using the Zener-Hollomon parameter is defined below the solidus temperature of 855 K and in the strain rate range 10^{-4} 1/s and 10^{5} 1/s. Constant strain rates are used outside the strain rate range for convergence reasons. The viscosity drops exponentially 3 orders of magnitude between 855 K and 905 K. This simulates steep viscosity drop at the onset of melting.

The UDF is written in C for the CFD software FLUENT version 5. The UDF is yet to be compiled, which is done in FLUENT 5 itself.

```
#include "udf.h"

DEFINE_PROPERTY(cell_viscosity, cell, thread)
{
 real mu_lam;
 real trial;
 real rate = CELL_STRAIN_RATE_MAG(cell,thread);
 real temp = C_T(cell,thread);

 mu_lam = 1.e12;
  if(temp < 855.)
  {
   if(rate > 1.0e-4 && rate < 1.e5)
     trial = 12830000. / rate * log(pow((rate * exp(17440.46 / temp)
     / 1.535146e8), 0.2817) + pow((1. + pow((rate * exp(17440.46 /
     temp) / 1.535146e8), 0.5634)) , 0.5));
   else if(rate >= 1.e5)
     trial = 128.3 * log(pow((exp(17440.46 / temp) /
     1.535146e3), 0.2817) + pow((1. + pow((exp(17440.46 / temp) /
     1.535146e3), 0.5634)) , 0.5));
   else
```

```
    trial = 1.283e11 * log(pow((exp(17440.46 / temp) /
    1.535146e12), 0.2817) + pow((1. + pow((exp(17440.46 / temp) /
    1.535146e12), 0.5634)) , 0.5));
  }
  else if(temp >= 855. && temp < 905.)
  {
   if(rate > 1.0e-4 && rate < 1.e5)
     trial = 12830000. / rate * log(pow((rate * 4.7063), 0.2817) +
     pow((1. + pow((rate * 4.7063), 0.5634)) , 0.5))* pow(10., -0.06
     * (temp - 855.));
   else if(rate >= 1.e5)
     trial = 243.654 * pow(10., -0.06 * (temp - 855.));
   else
     trial = 1.47897e10 * pow(10., -0.06 * (temp - 855.));
  }
  else if(temp >= 905.)
  {
   if(rate > 1.e-4 && rate < 1.e5)
     trial = 12830. / rate * log(pow((rate * 4.7063), 0.2817) +
     pow((1. + pow((rate * 4.7063), 0.5634)) , 0.5));
   else if(rate >= 1.e5)
     trial = 0.24365;
   else
     trial = 1.47897e7;
  }
  if(trial < 1.e12 && trial > 100.)
   mu_lam = trial;
  else if(trial <= 1.)
    mu_lam = 1.;
  else
   mu_lam = 1.e12;
return mu_lam;
}
```

AA2024

In the following, the user-defined function (UDF) for the viscosity of AA2024 is shown. The viscosity based on the Zener-Hollomon equation is defined below 770 K and in the strain rate range 10^{-4} 1/s and 10^{5} 1/s. Constant strain rates are used outside the strain rate range for convergence reasons. The viscosity drops exponentially 4 orders of magnitude between 770 K and 780 K. This simulates steep viscosity drop at the onset of melting.

```
#include "udf.h"

DEFINE_PROPERTY(cell_viscosity, cell, thread)
{
 real mu_lam;
 real trial;
 real rate = CELL_STRAIN_RATE_MAG(cell,thread);
 real temp = C_T(cell,thread);

 mu_lam = 1.e12;
  if(temp < 770.)
  {
   if(rate > 1.0e-4 && rate < 1.e5)
     trial = 36084000. / rate * log(pow((rate * exp(17907.14 / temp)
     / 5.63274e8), 0.234) + pow((1. + pow((rate * exp(17907.14 /
     temp) / 5.63274e8),0.468)) , 0.5));
   else if(rate >= 1.e5)
     trial = 360.84 * log(pow((exp(17907.14 / temp) / 5.63274e3),
     0.234) + pow((1. + pow((exp(17907.14 / temp) / 5.63274e3),
     0.468)) , 0.5));
   else
     trial = 360840000000. * log(pow((exp(17907.14 / temp) /
     5.63274e12), 0.234) + pow((1. + pow((exp(17907.14 / temp) /
     5.63274e12), 0.468)) , 0.5)); }
  else if(temp >= 770. && temp < 780.)
  {
   if(rate > 1.0e-4 && rate < 1.e5)
     trial = 36084000. / rate * log(pow((rate * 22.3483), 0.234) +
     pow((1. + pow((rate * 22.3483), 0.468)) , 0.5))* pow(10., -0.4
     * (temp - 770.));
   else if(rate >= 1.e5)
     trial = 1484.65 * pow(10., -0.4 * (temp - 770.));
   else
     trial = 8.56965e10 * pow(10., -0.4 * (temp - 770.));
  }
  else if(temp >= 780.)
  {
   if(rate > 1.0e-4 && rate < 1.e5)
     trial = 3608.4 / rate * log(pow((rate * 22.3483), 0.234) +
     pow((1. + pow((rate * 22.3483), 0.468)) , 0.5));
   else if(rate >= 1.e5)
     trial = 0.148465;
   else
     trial = 8.5695e6;
  }
  if(trial < 1.e12 && trial > 1.)
   mu_lam = trial;
  else if(trial <= 1.)
    mu_lam = 1.;
  else
   mu_lam = 1.e12;
 return mu_lam;
 }
```

Appendix C: Welding Data

The welding data of the friction stir welds described in chapter 4 is listed in the following tables.

Zero-degree welds in AA6061-T6

	RPM	WS [mm/s]	Z-Force [kN]	X-Force [N]	Torque [Nm]	Power [W]	Energy PUWL [J/mm]
1	232	2.36	31.136	4512.9	193.02	4705.4	1990.9
2	390	2.36	28.812	2862.4	125.95	5139.4	2174.5
3	464	2.36	26.688	4381.5	104.25	5068.7	2144.6
4	540	2.36	24.464	2639.6	92.59	5226.0	2211.1
Data below is scaled down to account for the different tool sizes.							
1*	232	2.36	19.92	2888	98.8	2409	1019
2*	390	2.36	18.44	1832	64.5	2631	1113
3*	464	2.36	17.08	2804	53.4	2595	1098
4*	540	2.36	15.66	1689	47.4	2676	1132

Table C-1 Welding data of the zero-degree weld in 25.4 mm thick AA6061-T6 described in Section 4.1.2. In the lower half of the table, the data is scaled down for comparison with welds performed with the standard tool (10 mm pin and 25.4 mm shoulder diameter, respectively). The scaling factor, which accounts for the different tool dimensions, is 0.512 for torque, power, and energy PUWL. The scaling factor for the tool forces is 0.64.

AA6061-T6 welds using the standard tool						
RPM	WS [mm/s]	Z-Force [kN]	X-Force [N]	Torque [Nm]	Power [W]	Energy PUWL [J/mm]
240	1.28	22.24	1748	108.6	2731	2135
240	2.36	26.69	3914	115.9	2915	1235
240	3.3	28.02	4195	118.5	2986	906
390	1.23	21.35	1403	64.1	2617	2125
390	2.36	22.24	1518	74.8	3056	1293
390	3.32	28.91	2163	87.4	3568	1076

Table C-2 Friction stir welds performed in AA6061-T6 using the standard tool (see Table 4-3 and Section 7.4.3).

References

1. Thomas, W.M. et al., "Friction Stir Butt Welding", International Patent Application No PCT/GB92/02203 and GB Patent Application No.9125978.8, Dec.1991, U. S. Patent No. 5,460,317.
2. Thomas, W. M., "Friction stir welding and related friction process characteristics", *7th International Conference on Joints in Aluminum*, Cambridge, UK, 16th April 1998.
3. Rhodes, C.G., Mahoney, M.W., Bingel, W.H., Spurling, R.A., and Bampton, C.C., "Effects of Friction Stir Welding on Microstructure of 7050 Aluminum", *Scripta Materialia*, vol. 36, pp. 69-75, 1997.
4. Mishra, R.S., Mahoney, M.W., McFadden, S.X., Mara, N.A., and Mukherjee, A.K., "High Strain Rate Superplasticity in a Friction Stir Processed Aluminum Alloy", *Scripta Materialia*, vol. 42, pp. 163-168, 2000.
5. Jata, K.V. and Semiatin, S.L., "Continuous Dynamic Recrystallization During Friction Stir Welding of High Strength Aluminum Alloys", *Scripta Materialia*, vol. 43, pp. 743-749, 2000.
6. Jata, K.V., Sankaran, K.K, and Ruschau, J.J., "Friction Stir Welding Effects on Microstructure and Fatigue of Aluminum Alloy 7050-T7451" *Metallurgical and Materials Transactions A*, vol. 31A, pp. 2181-2192, 2000.

7. Zienkiewicz, O.C. and Godbole, P.N., "Flow of plastic and visco-plastic solids with special reference to extrusion and forming processes", *International Journal for Numerical Methods in Engineering*, vol. 8, pp. 3-16, 1974.
8. Zienkiewicz, O.C., Jain, P.C., Onate, E., "Flow of solids during forming and extrusion: some aspects of numerical solutions", *International Journal for Numerical Methods in Engineering*, vol.14, pp.15-38, 1978.
9. Zienkiewicz, O.C. and Cormeau, I.C., "Visco-plasticity – Plasticity and Creep in elastic solids – A Unified Numerical Solution Approach", *International Journal for Numerical Methods in Engineering*, vol.8, pp. 821-845, 1974.
10. Zienkiewicz, O.C., Onate, E., Heinrichs, J.C., "A general formulation for coupled thermal flow of metals using finite elements", *International Journal for Numerical Methods in Engineering*, vol. 17, pp. 1497-1514, 1981.
11. Strenkowski, J.S. and Moon, K.J., "Finite Element Prediction of Chip Geometry and Tool/Workpiece Temperature Distributions in Orthogonal Metal Cutting", *Journal of Engineering for Industry – Transactions of the ASME*, vol. 112, pp. 313-318, 1990.
12. Rebolo, N. and Kobayashi, S., "A coupled analysis of viscoplastic deformation and heat transfer – I Theoretical considerations", *International Journal of Mechanical Science*, vol. 22, pp. 699-705, 1980.
13. Rebolo, N. and Kobayashi, S., "A coupled analysis of viscoplastic deformation and heat transfer – II Theoretical considerations", *International Journal of Mechanical Science*, vol. 22, pp. 699-705, 1980.
14. Bathe, K.J., "Finite Element Procedures", Prentice Hall, New Jersey, 1996

15. Kobayashi, S., Oh, S.I., Altan, T., "Metal Forming and the Finite-Element Method", *Oxford University Press*, New York, 1989.

16. Talbert, S.H. And Aviztur, B., "Plastic Flow in Metal Forming", John Wiley & Sons Ltd., Chichester, UK, 1996.

17. Tang, J., Wu, W.T., Walters, J., "Recent development and application of finite element method in metal forming", *Journal of Materials Processing Technology*, vol. 46, pp. 117-126, 1994.

18. Reinikainen, T., Andersson, K., Kiviuori, S., Korhonen, A.S., "Finite-element analysis of copper extrusion processes", *Journal of Materials Processing Technology*, vol. 34, pp. 101-108, 1992.

19. Surdon, G. and Chenot, J.L., "Finite element calculation of three-dimensional hot forging", *International Journal for Numerical Methods in Engineering*, vol. 24, pp. 2107-2177, 1987.

20. Shiau, Y.C. and Kobayashi, S., "Three-dimensional finite element analysis of open-die forging", *International Journal for Numerical Methods in Engineering*, vol. 25, pp. 67-85, 1988.

21. Meidert, M., Knoerr, M., Westphal, K., Altan, T., "Numerical and physical modelling of cold forging of bevel gears ", *Journal of Materials Processing Technology*, vol. 33, pp. 75-93, 1992.

22. Shen, G., Semiatin, S.L., Kropp, E., Altan, T., "A technique to compensate for temperature history effects in the simulation of non-isothermal forging processes", *Journal of Materials Processing Technology*, vol. 33, pp. 125-139, 1992.

23. Cheng, H., Grandhi, R.V., Malas, J.C., "Design of optimal process parameters for non-isothermal forging", *International Journal for Numerical Methods in Engineering*, vol. 37, pp. 155-177, 1994.

24. Lu, J., Saluja, N., Riviere, A.L., Zhou, Y., "Computer modeling of continuous forming extrusion process of AA6061 alloy", *Journal of Materials Processing Technology*, vol. 79, pp. 200-212, 1998.

25. Udagawa, T., Kropp, E., Altan, T., "Investigation of metal flow and temperatures by FEM in the extrusion of Ti-6Al-4V tubes", *Journal of Materials Processing Technology*, vol. 33, pp. 155-174, 1992.

26. Long, H. and Balendra, R., "FE simulation of the influence of thermal and elastic effects on the accuracy of cold-extruded components", *Journal of Materials Processing Technology*, 87, 247-260, 1998.

27. Chandra, T., Zhou, J., Kowalski, L., Duszczyk, J., "3D FEM simulation of the thermal events during AA6061 aluminum extrusion", *Scripta Materialia*, vol. 41, pp. 195-202, 1999.

28. Petersen, S.B. and Martins, P.A.F., "Finite element remeshing: A metal forming approach for quadrilateral mesh generation and refinement", *International Journal for Numerical Methods in Engineering*, vol. 40, pp. 1449-1464, 1997.

29. PavanaChand, C. and KrishnaKumar, R., " Remeshing issues in the finite element analysis of metal forming problems", *Journal of Materials Processing Technology*, vol. 75, pp. 63-74, 1998.

30. Gouveia, B.P.P.A., Rodrigues, J.M.C., Martins, P.A.F., "Finite element modeling of cold forward extrusion using updated Lagrangian-Eulerian formulations", *Journal of Materials Processing Technology*, vols. 80-81, pp. 647-652, 1998.

31. Movahhedy, M., Gadala, M.S., Altinas, Y., "Simulation of the orthogonal metal cutting process using an arbitrary Lagrangian-Eulerian finite-element method", *Journal of Materials Processing Technology*, vol. 103, pp. 267-275, 2000.

32. Joyot, P., Rakotomalala, R., Pantale, O., Touratier, M., Hakem, N., "A numerical simulation of steady state metal cutting", *Proceedings of the Institution of Mechanical Engineers Part C*, vol. 212, pp. 331-341, 1998.

33. Nakamura, T., Bay, N., Zhang, Z.L., "FEM Simulation of Friction Testing Method Based on Combined Forward Rod-Backward Can Extrusion", *Journal of Tribology*, vol. 119, pp. 501-506, Jul. 1997.

34. Peric, D. and Owen, D.R.J., "Finite-element applications to the nonlinear mechanics of solids", *Reports on Progress in Physics,* vol. 61, pp. 1495-1574, 1998.

35. Oancea, V.G. and Laursen, T.A., "A finite element formulation of thermomechanical rate-dependent frictional sliding", *International Journal for Numerical Methods in Engineering*, vol. 40, pp. 4275-4311, 1997.

36. Antunez, H.J. and Kleiber, M., "Sensitivity analysis of metal forming processes involving frictional contact in steady state", *Journal of Materials Processing Technology*, vol. 60, pp. 485-491, 1996.

37. Dickson, G.R. and Bahrani, A.S., "Friction Welding", *Proceedings of the 16th International Machine tool Design and Research Conference*, Manchester, UK, pp. 299-307, Sept. 1975.
38. Midling, O.T. and Grong, O., "A Process Model for Friction Welding of Al-Mg-Si Alloys and Al-SiC Metal Matrix Composites – I. HAZ Temperature and Strain Rate Distribution", *Acta Metallurgica Materialia*, vol. 42, pp. 1595-1609, 1994.
39. Vairis, A. and Frost, M., "On the extrusion stage of linear friction welding of Ti 6Al 4V", *Materials Science and Engineering A*, vol. 271, pp. 477-484, 1999.
40. Fu, L. and Duan, L., "The Coupled Deformation and Heat Flow Analysis by Finite Element Method During Friction Welding", *The Welding Journal*, pp. 202-207, May, 1998.
41. Francis, A., Craine, R.E., "On a model for frictioning stage in friction welding of thin tubes", *International Journal of Heat and Mass Transfer*, vol. 28, pp. 1747-1755, 1985.
42. Healy, J.J., McMullan, D.J., Bahrani, A.S. "Analysis of frictional phenomena in friction welding of mild steel", *Wear*, vol. 37, pp. 265-278, 1976.
43. Bendzsak, G.J., North T.H., Li, Z., "Numerical Model for Steady-State Flow in Friction Welding", *Acta Materialia*, vol. 45, pp. 1735-1745, 1997.
44. Zhai, Y., Malodano, C., North, T.H., Bendzsak, G.J., " Particle agglomeration and fracture in MA 956 and MMC friction joints", *International Journal of Materials and Product Technology*, vol. 13, pp. 89-104, 1998.

45. North, T.H., Bendzsak, G.J., Li, Z., Zhai, Y., " Particle Fracture, Retention, and Fluid Flow in Metal Matrix Composite Friction Joints", *Metallurgical and Materials Transactions A*, vol. 28A, pp. 2371-2384, Nov. 1997.

46. Midling, O.T., "Material Flow Behavior and Microstructural Integrity of Friction Stir Butt Weldments", *Proceedings of the 4th International Conference on Aluminum Alloys*, Atlanta, Georgia, USA, eds. T. H. Sanders, Jr., and E. A. Starke, Jr., pp. 451-458, Sept. 1994.

47. Li, Y., Murr, L.E. and McClure, J.C., "Solid-State Flow Visualization in the Friction Stir Welding of 2024 Al to 6061 Al", *Scripta Materialia*, vol. 40, pp. 1041-1046, 1999.

48. Colligan, K., "Material Flow Behavior during Friction Stir Welding of Aluminum", *Welding Journal*, vol. 75, pp. 229-237, 1999.

49. Seidel, T.U. and Reynolds, A.P., "Visualization of the Material Flow in AA2195 Friction Stir Welds Using a Marker Insert Technique", *Metallurgical and Materials Transactions A*, vol. 32A, pp. 2879-2884.

50. Reynolds, A.P., Seidel, T.U., Simonsen, M., "Visualization of Material Flow in an Autogenous Friction Stir Weld", Proceedings of the *1st International Symposium on FSW*, Thousand Oaks, CA, June 1999.

51. Reynolds, A.P., Lockwood, W.D., and Seidel, T.U., "Processing Property Correlation in Friction Stir Welds", *Materials Science Forum,* vols. 331-337, pp. 1719-1724, 2000.

52. Reynolds, A.P., "Visualization of material flow in autogenous friction stir welds", *Science and Technology of Welding and Joining*, vol. 5, pp. 120-124, 2000.

53. Seidel, T.U. and Reynolds, A.P., 'Correlation of Weld Temperatures with Material Flow in Solid-State Friction Stir Welds, *Proceedings of the SECTAM-XX*, MF90, Pine Mountain, GA, April 2000.

54. Larsson, H., Karlsson, L., Stoltz, S., Bergqvist, E.L., "Joining of dissimilar Al-alloys by Friction Stir Welding", *2nd Friction Stir Welding Symposium*, Gothenburg, Sweden, June 2000.

55. London, B., Mahoney, M., Bingel, W., Calabrese, M., and Waldron, D., "Experimental Methodology to Determine Metal Flow During FSW", AEROMAT Conference, Long Beach, CA, June 2001.

56. Russell, M.J. and Shercliff, H.R., "Analytical Modeling of Friction Stir Welding", *Proceedings of INALCO '98, 7th International Conference on Joints in Aluminium*, TWI, Abington, Cambridge, UK, April 1998.

57. Frigaard, Ø., Grong, Ø., Midling, O.T., "Modeling of Heat Flow Phenomena in Friction Stir Welding of Aluminum Alloys", *Proceedings of INALCO '98, 7th International Conference on Joints in Aluminium*, TWI, Abington, Cambridge, UK, April 1998.

58. Frigaard, Ø., Grong, Ø., Midling, O.T., "A Process Model for Friction Stir Welding of Age Hardening Aluminum Alloys", *Metallurgical and Materials Transactions A*, vol. 32A, pp. 1189-1200, 2001.

59. Gould, J.E. and Feng, Z., "Heat Flow Model for Friction Stir Welding of Aluminum Alloys", *Journal of Materials Processing & Manufacturing Science*, vol. 7, pp. 185-194, Oct. 1998.

60. Chao, Y.J. and Qi, X., "Thermal and Thermo-Mechanical Modeling of Friction Stir Welding of Aluminum Alloy 6061-T6", *Journal of Materials Processing & Manufacturing Science*, vol. 7, pp. 215-233, Oct.1998.

61. Tang, W. Guo, X., McClure, C., Murr, L.E., " Heat Input Model and Temperature Distribution in Friction Stir Welding", *Journal of Materials Processing & Manufacturing Science*, vol. 7, pp. 163-172, Oct. 1998

62. Steward, M.B., Adams, G.P., Nunes, A.C., Romine, P., "A Combined Experimental and Analytical Modeling Approach to Understanding Friction Stir Welding", *Proceedings of the 43rd International SAMPE Symposium*, Anaheim, CA, June 1998.

63. Nunes, A.C. Jr., " Wiping Metal Transfer In Friction Stir Welding", *Proceedings of the TMS 2001 Annual Meeting* New Orleans, LA, Feb. 2001.

64. Smith, C.B., Bendzsak, G.J., North T.H., Hinrichs, J.F., Noruk, J.S., Heideman, R.J., "Heat and Material Flow Modeling of the Friction Stir Welding Process", *Proceedings of the 9th International Conference in Computer Technology in Welding,* Detroit, MI, Sept. 1999.

65. North, T.H., Bendzsak, G.J., and Smith, C., "Material Properties Relevant to 3-D FSW Modeling", *2nd Friction Stir Welding Symposium*, Gothenburg, Sweden, June 2000.

66. North, T.H., Bendzsak, G.J., and Smith, C., "An Experimentally Validated 3D Model for Friction Stir Welding", *2nd Friction Stir Welding Symposium*, Gothenburg, Sweden, June 2000.

67. Colegrove, P. "3 Dimensional Flow and Thermal Modeling of the Friction Stir Welding Process", *Proceedings of the 2nd International Symposium on FSW*, Gothenburg, Sweden, June 2000.

68. Xu, S., Deng, X., Reynolds, A.P., Seidel, T.U., "Finite element Simulation of Material Flow in Friction Stir Welding", Science of Technology of Welding and Joining, vol. 6, pp. 191-193, 2001.

69. Reynolds A. P. and Tang, W., "Alloy, Tool Geometry, And Process Parameter Effects on Friction Stir Weld Energies and Resultant FSW Joint Properties", *Proceedings of the TMS 2001 Fall Meeting*, Indianapolis, IN, Nov. 2001.

70. Karman, Th. v., "Hauptaufsätze über laminare und turbulente Reibung", *Zeitschrift für Angewandte Mathematik und Mechanik*, vol. 1 (4), 1921.

71. Eirich, F.R., "Rheology Theory and Applications Volume 1", Academic *Press*, New York, 1956.

72. Gilman J.J., "Micromechanics of Flow in Solids", *McGraw-Hill*, New York, 1969.

73. White, F.M., "Viscous Fluid Flow 2nd edition", *McGraw Hill*, Boston, MA, 1991.

74. Badr, H. and Dennis, S.C.R., "Time-dependent viscous flow past an impulsively started rotating and translating circular cylinder", *Journal of Fluid Mechanics*, vol. 158, pp. 447-488, 1985.

75. Dhahir, S.A. and Walters, K., "On Non-Newtonian Flow Past a Cylinder in a Confined Flow", *Journal of Rheology*, vol. 33, pp. 781-804, 1989.

76. Juarez, H., Ridgway, S., Metcalfe, R., Bagheri, B., "Direct simulation of freely rotating cylinders in viscous flows by high-order finite element methods", *Computers & Fluids*, vol. 29, pp. 547-582, 2000.

77. FLUENT 5 User's Guide, *Fluent Incorporated*, Lebanon, NH, 1998.

78. Sigworth, G.K., "Rheological properties of metal alloys in the semi-solid state", *Canadian Metallurgical Quarterly*, vol. 35, pp. 101-122, 1996.

79. Jaluria, Y., "Numerical Modeling of Materials Processing Systems", *Computational Mechanics*, vol. 21, pp. 199-210, Apr. 1998.

80. Malas, J.C. and Seetharaman, V., "Using Material Behavior Models to Develop Process Control Strategies", *JOM – Journal of the Minerals Metals & Materials Science*, vol. 44, pp. 8-13, 1992.

81. Mukai, T., Ishikawa, K., Higashi, K., "Influence of the strain rate on the mechanical properties in fine-grained aluminum alloys", *Materials Science and Engineering A*, vol. 204, pp. 12-18, 1995.

82. Oosterkamp, L.D., Ivankovic, A., Venizelos, G., "High Strain Rate properties of selected aluminum alloys", *Materials Science and Engineering A*, vol. 278, pp. 225-235, 2000.

83. Altan, T. and Boulger F.W., "Flow Stress of Metals and Its Application in Metal Forming Analysis", *Journal of Engineering for Industry – Transactions of the ASME*, vol. 95, pp. 1009-1019, 1973.

84. Zener, C. and Hollomon, J.H., "Effect of Strain Rate Upon Plastic Flow of Steel", *Journal of Applied Physics,* vol. 15, pp. 22-32, 1944.

85. Sellars, C.M. and Tegart, W.J.McG., "Hot Workability", *International Metallurgical Reviews*, vol. 17, pp. 1-24, 1972.

86. Shepard, T. and Wright, D.S., "Determination of flow stress: Part 1 constitutive equation for aluminum alloys at elevated temperatures", *Metals Technology*, pp. 215-223, June 1979.

87. Sheppard, T., "Extrusion of AA2024 alloy", *Materials Science and Technology,* vol. 9, pp. 430-440, 1997.

88. Zhou, M. and Clode, M.P., "Modeling of high temperature viscoplastic flow of aluminum alloys by hot torsion testing", *Materials Science and Technology,* vol. 13, pp. 818-824, 1997.

89. Clode, M.P. and Sheppard, T., "Extrusion limit diagram containing structural and topological information for AA6063 aluminum alloy", *Materials Science and Technology*, vol. 9, pp. 313-318, 1993.

90. Sheppard, T. and Jackson, A., "Constitutive equations for use in prediction of flow stress during extrusion of aluminum alloys", *Materials Science and Technology*, vol. 13, pp. 203-209, 1997.

91. Shimansky, D. and McQueen, H.J., "Hot working of heat resistant rapidly solidified aluminum alloy 8009", *Materials Science Forum,* vols. 217-222, pp. 1199-1202, 1996.

92. McQueen, H.J. and Lee, M.J., "Hot Workability of High Strength 6060 Alloy", *Materials Science Forum,* vols. 331-337, pp. 437-442, 2000.

93. Wang, Y., Lin, D., and Law, C.C., "A correlation between tensile flow stress and Zener-Hollomon factor in TiAl alloys at high temperatures", *Journal of Materials Science Letters*, vol. 19, pp. 1185-1188, 2000.

94. Aukrust, T. and LaZghab, S., "Thin shear boundary layers in flow of hot aluminum", *International Journal of Plasticity*, vol. 16, pp. 59-71, 2000.

95. Wright, R.N. and Paulson, M.S., "Constitutive equation development for high strain rate deformation processing of aluminum alloys", *Journal of Materials Processing Technology*, vol. 80-81, pp. 556-559, 1998.

96. Zhou, M. and Clode, M.P., "Constitutive equations for modelling flow softening due to dynamic recovery and heat generation during plastic deformation", *Mechanics of Materials*, vol. 27, pp. 63-76, 1998.

97. Puchi Cabrera, E.S., Villalobos Gutiérrez, C. and Castro Fariñas, G., "Dynamic materials modelling concepts applied to analysis of hot rolling commercial aluminium alloys", *Materials Science and Technology*, vol. 16, pp. 1049-1055, 2000.

98. Khandkar, Z. and Xu, S., Private Communication, University of South Carolina, 2001.

99. Lindner, K., Private Communication, University of South Carolina, 2001.

100. Chao, Y.J., Qi, X. and W. Tang, "Heat Transfer in Friction Stir Welding – Experimental and Numerical Studies", *in review at Journal of Manufacturing Science and Engineering Transactions of the ASME.*

101. Reynolds A. P., unpublished research, 2001, University of South Carolina, Dept. ME.